Ben-Gurion University of the Negev
Faculty of Engineering Sciences
School of Electrical and Computer Engineering
Electro-Optics and Photonics Engineering Department

Novel Integrated Photonics Architectures for Efficient Light Manipulation on a Chip

---

By:

Adir Hazan

A Thesis Submitted in Partial Fulfillment of the Requirements for the Master of Science Degree

Under the supervision of

Prof. Alina Karabchevsky

September, 2022

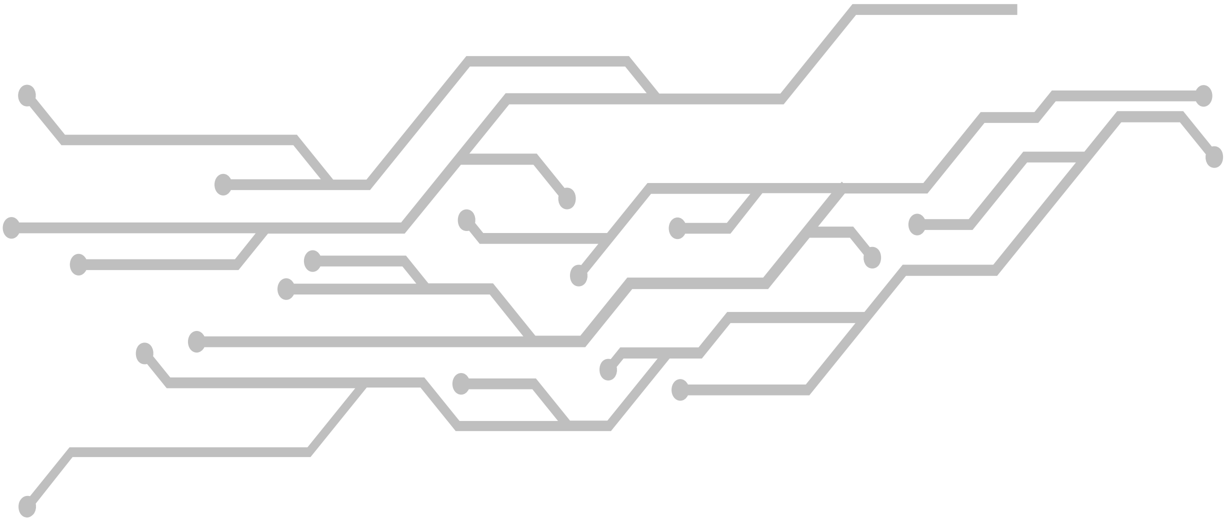

Ben-Gurion University of the Negev
Faculty of Engineering Sciences
School of Electrical and Computer Engineering
Electro-Optics and Photonics Engineering Department

Novel Integrated Photonics Architectures for Efficient Light Manipulation on a Chip

---

By:

Adir Hazan

A thesis submitted in partial fulfillment of the requirements for the Master of Science degree

Under the supervision of

Prof. Alina Karabchevsky

Adir Hazan 17/2/2023

Author *Date*

Alina Karabchevsky 19/02/2023

Supervisor *Date*

Chairman of Graduate Studies Committee *Date*

September, 2022

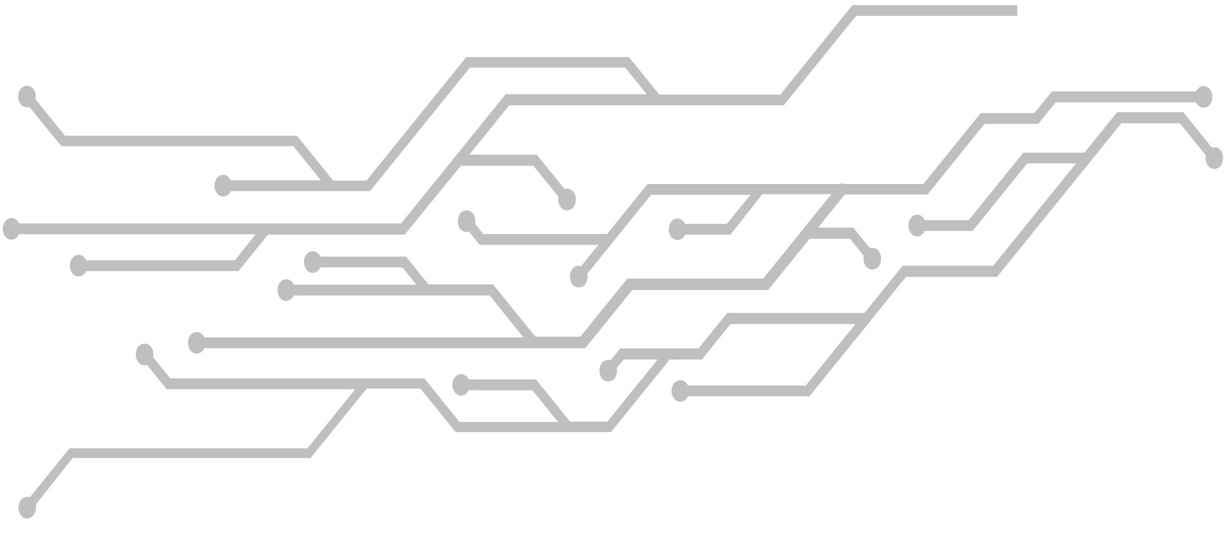

Abstract

Integrated photonics is one of the significant milestones of electro-optics and photonics science. This platform contains on-chip optoelectronic devices dealing with controlling and manipulating light in integrated circuits for applications aimed to achieve advantages that outperform those traditionally tackled by electronics. These ultra-fast and low-power architectures have drawn broad interest and have led to possible utilization in a wide range of commercial areas and research fields, including optical communications, optical computation, quantum optics, information processing, cryptography, and many others.

In this work, I investigated different new directions and studied how guided-wave optics configurations can be used for implementing unique optical functionalities. By employing light-matter interactions in two-dimensional $Ti_3C_2T_x$ (MXenes family) in the near-infrared range, I experimentally demonstrated two novel approaches for implementing an all-optical neuron nonlinear activation function in two configurations: 1) a silicon waveguide with MXene flakes overlayer, and 2) a MXene thin film deposited onto a transparent substrate. These proposed configurations can serve as nonlinear units in all-optical implementations of photonic deep structured learning architectures, in which the nonlinear transfer function can be flexibly designed depending on the operating wavelength, without modifying the physical structure. Their capability and feasibility were examined and compared to well-known software-based nonlinear activation functions by conducting classification tasks utilizing two independent deep-learning architectures to characterize their performances in terms of accuracy. The same technique can be generalized to implement arbitrary machine-learning tasks.

I designed a practical photonic candidate construction based on integrated building blocks for an on-chip quantum money scheme as quantum tokens, where the qubits were realized by utilizing a set of discrete waveguide normal polarized modes. The optimal structures of the photonic transmitter and receiver were obtained by extensive theoretical analysis of their optical operation mechanism. In addition, an experimental setup for the optical token prototype was proposed, using currently available optical communication guided-wave optics devices.

I experimentally demonstrated the feasibility of polarization state manipulation of guided linear polarized light by utilizing a unique 3D waveguide structure having a weak refractive index contrast between the core and the cladding. For such a 90° twisted waveguided immersed inside glass with a rectangular cross-section shape rotated along its length, the polarization state of the photons gradually changes when the light propagates along the twisted region.

For each study, I presented the fundamental concepts and the approaches required for comprehending light-matter interactions incorporated with guided-wave optics. The methods used to achieve each research objective are summarized, and advanced numerical and experimental observations are demonstrated and analyzed in this thesis.

Keywords: Integrated Photonics, Guided-Wave Optics, Optical Deep-Learning, MXene, Light-Matter Interactions, Twisted Waveguide, Optical Quantum Money.

Table of Contents

List of Figures

List of Tables

Abbreviations

Notation	*Description*
AF	Activation Function
CW	Continuous Wave
EM	Electromagnetic
EO	Electro-optic
FFNN	Feedforward Neural Network
MMW	Multimode Waveguide
MO	Microscope Objective
MZI	Mach-Zehnder Interferometer
NIR	Near Infrared
NN	Neural Network
OIU	Optical Interference Unit
QM	Quantum Money
ONLU	Optical Nonlinearity Unit
OSA	Optical Spectrum Analyzer
Qubit	Quantum Bit
RI	Refractive Index
SM	Single Mode
SPAD	Single Photon Avalanche Detector
TE	Transverse Electric
TM	Transverse Magnetic
2D	Two Dimensional
3D	Three Dimensional

Symbols and Constants

Symbol	*Description*	*Value*	*Units*
c	Speed of light in vacuum	2.99792×10^8	$\mathrm{m \cdot s^{-1}}$
λ	Vacuum wavelength	-	m
$\tilde{\varepsilon}_r$	The complex relative permittivity	-	-
ε_1	Real part of the complex relative permittivity	-	-
ε_2	Imaginary part of the complex relative permittivity	-	-
ε_0	Vacuum permittivity	8.85419×10^{-12}	$\mathrm{F \cdot m^{-1}}$
$\tilde{n}$	Complex refractive index	-	-
n	Real part of the refractive index	-	-
κ	Extinction coefficient	-	-
E	Electric field	-	$\mathrm{V \cdot m^{-1}}$
I	Optical intensity	-	$\mathrm{W \cdot m^{-2}}$
T	Transmittance	-	$\%$
$\lvert\psi\rangle$	Quantum state	-	-
μ_α	Mean photon number	-	-
h	Planck's constant	6.62607×10^{-34}	$\mathrm{J \cdot Hz^{-1}}$
BK-7	Borosilicate Glass (Element Symbol)	-	-
Si	Silicon (Element Symbol)	-	-
Ti	Titanium (Element Symbol)	-	-
$\mathrm{LiNbO_3}$	Lithium Niobate (Chemical Formula)	-	-
$\mathrm{SiO_2}$	Silicon Dioxide (Chemical Formula)	-	-
$\mathrm{Ti_3C_2T}_x$	Titanium Carbide, MXene family (Chemical Formula)	-	-

CHAPTER 1

Introduction

The 21^{st} century can be considered the century of the elementary excitation of the quantized electromagnetic (EM) field - the photon. In analogy to electronics, photonics utilizes the ”flow” of photons in a light beam through a material or engineered structure, instead of the movement of electrons, for optical processing and computing. Thus, generating, controlling, manipulating, measuring, and detecting light enables researchers to push state-of-the-art photonics-powered applications in many fields of science, society, and the economy.

Traditionally, optical waveguides are made from transparent dielectric materials [1] to form a spatially inhomogeneous structure for guiding EM waves in the optical spectrum. Naturally, confining, guiding, and passively directing optical EM waves embody light-matter interaction linear properties [2]. Besides being a key element to light guiding, this allows the construction of various guided-wave devices that form fundamental building blocks for integrated optical circuits. In addition, light can be absorbed, scattered, or radiated as it propagates through the waveguide, which triggers ultra-fast and low-power devices to upgrade the performance of classical optical waveguides and overcome conventional systems.

Since in the quantum nature of the photons as boson particles, except under extraordinary conditions, they do not interact with each other, controlling light by light usually requires matter - specifically, nonlinear optical processes. Guided-wave optics manipulation based on light-matter interaction ranges from numerous well-known optical nonlinear phenomena - such as changing the material refractive index (RI) described by the Kerr effect [3] or its absorption described by saturable absorption [4], or over-enhancing light-matter interaction via optical meta-waveguides using metasurfaces and metamaterials [5] - to hybrid plasmonic structures [6, 7] for field localization and enhancement in plasmonic waveguides.

Guided-wave optics architectures are a comprehensive class of devices capable of controlling and manipulating light, and can play a role at the crossroads of several disciplines, including photonics, electronics, physics, mathematics, and materials [8–10]. These involve structural design and modeling, EM wave propagation computational algorithms, fabrication techniques, and photonic building block functionalities [11, 12]. The photonic structures are engineered to effect optical material properties interacting with light to manipulate particular optical signals by changing their primary properties, such as intensity, phase, wavelength, propagation direction, and polarization. Consequently, tailormade optical transfer functions can be assembled.

Here, I take advantage of light-matter interactions incorporated with practical guided-wave optics configurations. I investigate how they can be used for unique optical application scenarios via on-chip light manipulating and controlling through its propagation. These include manipulating the propagating light through a dielectric waveguide; designing on-chip quantum money protocol via guided-wave optics; and demonstrating all-optical neuron nonlinear activation function (AF) for photonic deep structured learning. I present the key elements of optical EM wave propagation in dielectric media needed for dealing with light-confinement in advanced guided-wave optics architecture, and review the theory of three-dimensional (3D) guided-wave optics uniformly twisted along its longitudinal axis. In addition, the fundamental concepts of a nonlinear optical process are presented to examine how their optical response can be manipulated in such saturable absorber material. I present the photonic deep structured learning principles required for understanding the photonics neural networks (NNs) operation mechanism, provide an overview of the available state-of-the-art optical interference implementations for linear operation, and investigate the required optical properties to implement the nonlinearity of the photonic neuron. Finally, I present the outcomes of my work executed in the fields of on-chip polarization manipulation in the NIR through a twisted waveguide having varying cross-section shape along the propagation direction of the light [13]; guided-wave optics that enable optical quantum money; and an all-optical realization for a photonic deep structured learning nonlinearity unit [14].

1.1 Motivation

Multiple essential and exciting issues in the field of guided-wave optics have already been addressed [15]. However, many other efforts still need to be accomplished to implement it as a significant part of daily life applications, which may take the place of electronics as the dominant technology. Therefore, the study and development of novel on-chip architectures to efficiently manipulate light play an essential role in deploying advanced photonics technologies.

Reviewing the rapidly growing on-chip nanophotonics field, including current novel technologies and devices with their challenges and future plans [15], led me to proceed to explore novel guided-wave optics configurations for unique on-chip applications such as manipulating the polarization state of light on a chip and a practical photonic implementation of a quantum technology key scheme. In addition, while investigating an all-optical nanosensor switch engineered to operate at telecommunication wavelengths caused by the excitation of molecular overtones in a unique hybrid plasmonic-dielectric configuration [16], I was motivated to expand the research by investigating an advanced photonics computational approach in which the light is controlled with waveguides for all-optical computing.

This research activity aims to investigate new directions of novel on-chip configurations for unique functionalities such as twisted dielectric waveguide architecture, on-chip quantum money, and all-optical neuron nonlinear AF. To this end, my research objectives include experimentally demonstrating the polarization state manipulation of propagating light by employing a twisted rectangular shape waveguide in glass at commonly used wavelengths in both the NIR and visible regions; designing a practical photonic implementation of quantum money relying on classical verification via guided-wave optics; and experimentally investigating new approaches for implementing all-optical nonlinearity in photonics deep structured learning by utilizing light-matter interaction and nonlinear effects in MXene.

1.2 State of the Art

Light-matter interaction is one of the earliest and simultaneously one of the most lively research areas. Its scope ranges from classical to quantum-mechanical features, including optical communication, spectroscopy, biosensing, quantum computing, cryptography, and many others. In this section, I overview the state-of-the-art in each subject studied.

1.2.1 All-Optical Neural Networks – Advantages and Drawbacks

A significant landmark in the era of big data is the shifting of the emphasis from the manner in which datasets are collected to processing such data in real time. Hence, two of the modern challenges that machine learning engineers and data scientists face are computational speed and energy consumption, which have motivated many researchers to explore and develop light-based NNs. Artificial deep structured learning is one of the most advanced methods of improving computation, inspired by the human brain signal processing. Developing deep structured learning systems that only rely on light, and that allow training and applying different models could achieve benefits beyond those possible with traditional electronics-based computing.

Generally, there are two aspects to integrating artificial NN with photonics. On the one hand, implementing deep structured learning in electro-optics and photonics applications, and utilizing the advantages of photonics over traditional microelectronic NN implementation for machine-learning applications on the other. Many optical applications employ NNs for various achievements. These include predicting subwavelength nanophotonic device optical response or obtaining their inverse design [17–21], neuromorphic computing [22], enhanced optical sensing [23–25], enabled super-resolution imaging [26, 27], and many others. The advances in complex machine learning tasks demand plenty of computational power, existing computational resources are beginning to be insufficient.

In resource-constrained environments, NN performance is limited due to their computational requirements. Therefore, efforts have been increased to develop photonics deep structured learning architectures and all-optical computing-based NN hardware to improve computational speed and power efficiency [28]. Integrated photonics presents a phase-stable, miniaturized, and robust platform to implement complex photonic circuits without being susceptible to EM interference. Consequently, it is a possible attractive method to realize light-based NNs [29]. Whereas photonic NN approaches can significantly improve computational speed and simultaneous energy consumption compared with conventional deep structured learning hardware, several challenges exist in their ideal realization.

In principle, the fundamental unit of NNs is the neuron, which involves weighting and summation, followed by the application of nonlinear AF - a vital part of NN's powerful expression ability. While realizing all-optical deep structured learning architectures, implementing versions of the photonic nonlinear transfer function achieved by light-matter interactions is a tremendous challenge that remains to be addressed. Moreover, the most energy-intensive process in all-optical NNs implementation is generating the input optical signals that require high-powered lasers. Therefore, a chip-scale laser for fully integrated photonics needs to be considered [30]. The energy consumption of the active electro-optical modulators also impacts the optical deep structured learning architecture. In addition, optimizing the weights continuously via backpropagation, and utilizing the error based on the calculated output signals, requires updates of the photonic NN parameters while modifying the optical guided-wave device characteristics [31, 32]. Traditional digital computers still carry out the photonic deep structured learning training phase. That limits the emulation of the system performances, computing speed, and expansion of the photonics NN approach to a broad range of computation tasks.

Two chip-scale mechanisms for implementing a fully optically neuron nonlinear AF were suggested in this work to address the issue of realizing an all-optical nonlinear transfer function for photonic NN architectures. These rely on the nonlinear optical response of novel two-dimensional (2D) material MXene-based devices in the near-infrared (NIR) operating in a broad spectral range. MXenes, a new series of 2D material, contains a broad category of transition metal carbides and nitrides (e.g., $Ti_3C_2T_x$). These present unique light-matter interactions: either nonlinear effects of saturable absorption [33, 34] and two-photon absorption [35] or, under other conditions, plasmonic features [36, 37]. MXene-based all-optical AF architectures may play a critical role in deploying deep structured learning technologies and provide new perspectives for implementing other functionalities.

1.2.2 Quantum Money – A Dream or a Technology to be Realized?

As long as money exists, people will try to copy it. Although such activity is illegal, there is no available payment method in which the 'laws of nature' prevent a forger from copying physical banknotes. In general, whatever a bank can do to make the money, a counterfeiter can act to copy it. This is because the security of current payment methods in the classical world (e.g., coins and bills or credit cards) rely only on computational assumptions or the fact that it is not easy to copy the physical medium due to its complex design. As a result, these are potential and attractive targets for forging and duplicating due to fast technological advancement.

Quantum money (QM) as a quantum token was first introduced by Wiesner [38], circa 1969. The notion of QM is quite similar to the money used today, with two main advantages: 1) thanks to the unique quantum principles, it is physically impossible to forge the money, and 2) it is digitally transferable. Any QM scheme aims to make an unforgeable currency - achieved by unclonable quantum states. That enables a trusted authority (e.g., the bank) to provide verifiable cash embedding a sequence of quantum bits (qubits) prepared from a set of different bases, which an untrusted user cannot copy or increase the amount. On the one hand, having the certainty of measuring a qubit state in one of the two encoding bases removes any certainty of measuring a particular state in the other basis and vice versa. That is known as Heisenberg's uncertainty principle. On the other hand, the no-cloning theorem states that it is impossible to make an exact copy of an arbitrary quantum object in an unknown state [39]. Consequently, these mechanisms establish quantum tokens as one-time passwords [40] for various attractive applications such as guaranteeing the security of QM, a tokenized signature scheme to produce signed documents, quantum teleportation, and others.

Despite QM proposal maturity, this milestone protocol has not yet seen the same experimental progress compared to more popular research fields, including quantum communication and quantum computation, due to its lack of realizability which remains a technological challenge. A practical unforgeable QM scheme suffers from two main drawbacks: 1) long-distance quantum communication between the payment terminals and the bank is required for each validation, which is limited by the noise and losses of transmitting the quantum states. 2) money has several functions, one of which is the storage of value, hence QM requires long-term quantum state storage devices [41, 42].

In recent years, the experimental interest in QM schemes has increased, with demonstrations of attacking quantum state-based optical QM schemes and attempting their forgery [43, 44]. Besides particle-like states, the qubits were applied to the most closely resembling classical states, with proof-of-principle versions of implementing coherent state-based quantum token schemes [45–47], and appropriate security proofs considering the optimal cloning of such states [48–50]. While in these various refinement schemes of Wiesner's original work, the challenging quantum communication was replaced by a classical channel for the verification phase, the primary missing ingredient for real use cases in QM is to store the qubits states for long periods. By contrast, some quantum applications, such as tokenized signature schemes, do not necessarily need to be stored for long periods, thus extending the usage of QM states [51] to another notion called message authentication code [52, 53]. Currently, cryptographic tokens are broadly employed as an additional layer of security. Whereas classical tokens for verifiable signed documents are sensitive to duplication, untrusted parties cannot forge quantum tokens with the additional property that can allow the holder to obtain a one-use quantum signing token.

Practical and large-scale deployment of quantum optical tokens might require a chip-to-chip system based on guided-wave optics devices compatible with mass manufacture and easy integration with current and developing optical and microelectronics technologies. In this work, photonic candidate construction was presented for preparing and verifying quantum optical tokens that may allow the usage of QM and quantum signing tokens. The design relies on implementing a qubit utilizing the polarization properties of a set of optical discrete normal modes. The main advantages are miniaturization, environmental robustness, cost-effective device manufacture, and the possibility of applying the qubits to either quantum states or classical states of an optical field - which means, among other factors, that these do not require new security proofs. Advancements in quantum memory may pave the way to using QM as the primary payment method for future universal transactions.

1.2.3 On-Chip Polarization Manipulation

Polarization manipulations have always been a concern for demanded functionalities in various photonic systems due to the building blocks of guided-wave optics exhibiting significant polarization-dependent. Its scope ranges from optical technologies such as telecommunication [54] over spectroscopy [55] and sensing [56, 57] to quantum information encoding [58, 59]. To process polarization-encoded information in photonic integrated circuits, controlling the polarization state of propagating light is necessary and requires combinations of polarization manipulation, polarization isolator, polarization rotator, and more. Though there are many examples of implementing polarization state manipulation of the light realized in free-space [60–62], utilizing conventional bulk optical waveplates - on-chip polarization conversion using guided-wave optics, in general, is nontrivial and remains an open challenge.

Current methods for manipulating the polarization states of light in photonic integrated circuits can be divided into three classes: 1) Asymmetric cross-section waveguide, where the orthogonal polarization modes interfere with one another [63]. This standard method requires extraordinary fabrication accuracy and is usually wavelength sensitive. 2) Surface plasmon resonance [64]; although these devices can be very small, their performance is severely encumbered by the absorption of the metal. 3) Mode evolution-based type, where the polarization of the photon changes as the waveguide geometry is slowly engineered, has broad bandwidth benefits, and there is no strict requirement on fabrication accuracy [65–67].

Novel 3D waveguide structure geometries, such as twisted waveguides, can have interesting functionalities for implementing on-chip polarization manipulation. However, the characterization of twisted waveguides immersed in optical glass based on weak-guidance approximation has never been explored and remains to be addressed. This work experimentally investigated the feasibility of on-chip polarization manipulation via a dielectric rectangular waveguide uniformly twisting along its longitudinal axis - operating at a desired wavelength in commonly used bands in NIR and visible regions. The proposed twisted rectangular waveguide can be further generalized to realize an almost arbitrary wavelength-dependent waveplate on a chip by modifying its design parameters [13]. In addition, the twisted waveguide configuration can be found extremely useful as a waveguide polarization rotation for ultra-highspeed optical communication systems [65]; polarization diversity systems which consist of polarization beam splitters and polarization rotators that allow designing and fabrication of functional devices (e.g., filter) for one polarization state instead of both TE and TM modes; an integrated polarization-entangled photon-pair source [68] consists of a 90° polarization rotation sandwiched by two buried channel waveguides - generates the polarization-encoded quantum state on a chip; and more than 90° polarization rotation is clearly needed for unique photonics applications, i.e., arbitrary linear polarization states are needed for plenty of polarization-encoded information processing implementations [59]. Moreover, a novel platform of twisted optical elements can be formatted based on this fundamental building block, including a twisted coupler, a Mach-Zehnder interferometer (MZI) whose arms are twisted, a twisted beam splitter, a twist ring resonator which becomes to be an optical Möbius ring, and many other.

1.3 Thesis Outline

This thesis is organized as follows: in the current chapter, I overview each state-of-the-art on each studied project and give their fundamental principles.

Chapter 2 is dedicated to the theoretical foundations and methods used to explore various guided-wave optics architectures, which are essential for the following sections. I will begin by reviewing the EM wave propagation nature in optical waveguides with concepts of guided mode optics and twisted dielectric waveguides with a rectangular cross-section shape. Before I discuss the photonic deep structured learning principles, optical saturable absorption behavior will be introduced. I will elaborate on the photonic NN mechanism of operation, including an optical interference unit for linear operation and optical nonlinearity unit applications. Finally, the principles of photonics-based quantum computing are presented based on qubits encoding in different degrees of freedom of the fundamental particle of light - photon.

In Chapter 3, the previously described methods are applied to design novel devices employing a combined approach of theoretical analysis, numerical study, and experimental measurements. The main results for each project are presented in this chapter. Unique light-MXene interactions are explored in two independent configurations, and how their transform functions could be utilized for nonlinear AF in photonic-based deep structured learning is demonstrated. In addition, the design and implementation of a photonic chip-to-chip system are presented for preparing and verifying quantum optical tokens, allowing QM (as a quantum token) to rely on classical verification, which is also compatible with the scheme for message authentication code. The remainder of this chapter presents the practical considerations for a novel twisted waveguide embedded inside glass with a 90° twisting angle, along with experimental evidence for manipulating the polarization state of guided linear polarized light.

Chapter 4 summarizes and concludes the thesis. It ends with an outlook on possible future research and perspectives in the field of the studied topics in Chapter 5. Finally, the research activities are presented, where novel guided-wave optics architectures are utilized for efficient light manipulation on a chip for unique functionalities.

CHAPTER 2

Fundamentals

This chapter introduces light propagation foundations and concepts in optical media and complementary light-matter interactions. The discussion is limited to topics relevant to later sections. Various photonic systems and their optical mechanisms are reviewed, emphasizing on guided-wave optics devices since they are of central interest in this thesis. The basic notions and essential principles of various photonic approaches used in several devices and applications throughout this work are presented to enable the understanding of key elements at the root of developing more complex optical procedures.

2.1 Electromagnetic Wave Propagation in Optical Waveguides

Optical waveguide architectures are categorized according to their geometrical design, mode field distribution, RI distribution and material platforms. Unique configurations can be engineered to exhibit tailormade properties in different applications, such as optical communication, high-powered waveguide lasers, sensing, and more. The key element of an optical waveguide is its designed structure that aims to guide the flow of EM waves in a definite direction, confining it to a region either inside or close to its surface boundaries.

A dielectric optical waveguide is constructed from the guiding element with a higher RI medium; the so-called core is embedded between the substrate and cladding with a low RI medium. Broadly, the waveguide configurations fall into three major classes depending on their optical confinement direction. The first two classes consist of waveguides in which the light is confined in one or two transverse directions (a.k.a. 1D and 2D waveguides) - while their RI distribution is not a function of the light propagation direction. These waveguides can be characterized with a transverse spatially dependent profile of their dielectric function $\varepsilon(x)$ such as slab, or $\varepsilon(x, y)$ including rib, buried, and others made of optically isotropic media. The third class contains waveguides with a RI that vary along the light propagation direction (a.k.a. 3D waveguides), assembled by optically anisotropic media or having changed cross-section shape and size along their propagation direction.

2.1.1 Concepts of Guided Mode Optics

The optical waveguide is the fundamental passive element that interconnects the various devices of the photonic integrated circuit, in analogy to a metal strip in an electrical integrated circuit. While the electrical current flows through a metal strip according to Ohm's law, the optical waves travel in the optical waveguide in distinct optical modes (i.e., the spatial distribution of optical energy in one or more dimensions). Moreover, this optical transparent dielectric structure is a key component of many passive and active complex devices for manipulating and controlling light in various integrated photonics applications [15, 69].

One can describe the optical modes by geometrical optics (a.k.a. ray optics) approach, relying on the geometrical ray-tracing principles of classical optics. Thus, a light beam that is coupled into a waveguide is confined in the core, composed of plane waves moving in "zig-zag" paths undergoing total internal reflection (TIR) at the interfaces bounding the waveguides [70]. While the plane waves forming each mode travel with the same phase velocity, the angle of reflection at the interfaces bounding the waveguides is different for each mode (i.e., the component of the phase velocity in the propagation direction is different). Namely, each mode is associated with light rays at a distinct propagation angle. On the other hand, the optical modes can also be described by wave optics (a.k.a. physical optics) approach, providing a more comprehensive description [8]. Light propagates as an EM wave along a waveguide as a solution of Maxwell's equations using the constitutive relationships under the appropriate boundary conditions at the interfaces bounding the waveguide. A mode is the discrete solution of the wave equations (derived from Maxwell's equations) for an EM field propagating along the waveguide with a distinct propagation constant β, phase velocity, group velocity, polarization, and spatial field intensity distribution. Generally, a mode can be characterized by the effective index n_{eff} and spatial distribution of the EM field in one dimension or more. Each mode propagates through the waveguide with a phase velocity of $v_p = c/n_{\text{eff}}$, where c is the speed of light in vacuum, and n_{eff} is the mode effective index.

Dielectric rectangular and slab waveguides are the most common geometries of waveguides in optical device applications. A traditional three-layer slab waveguide consists of a guiding layer (a.k.a. waveguide core) in which the light is confined, sandwiched between a substrate and a cladding, as depicted in Fig. 1- that consider the light propagation in the z-direction, and the inner layer possesses the highest RI, i.e., $n_{\text{core}} > n_{\text{sub}} \geq n_{\text{clad}}$. The solution to the wave equation in each dielectric region (i.e., the i^{th} layer) under the appropriate boundary conditions for the waveguide shown in Fig.1 can be deduced by considering two cases: 1) $\beta < k_0 n_i$, the solution has an oscillatory nature, and 2) $\beta > k_0 n_i$, the solution decaying exponentially as a function of the distance in the x-direction from the corresponding core-medium interface [70]. The relation between the propagation constants $h = \sqrt{k_0^2 n_i^2 - \beta^2}$ (transverse, x component of k), β (longitudinal, z component of k), and $k = k_0 n_i$ are given by $k^2 = \beta^2 + h^2$. The propagation constant β belonging to the discrete mode m must satisfy the following condition in order to be guided inside the waveguide:

$$n_{\text{clad}} \leq n_{\text{sub}} < n_{\text{eff}} = \frac{\beta}{k_0} < n_{\text{core}} \, . \tag{2.1}$$

where the ratio between the propagation constant β and the vacuum propagation constant $k_0 = \frac{2\pi}{\lambda}$ defines the mode effective index n_{eff}. Although optical waveguides can support various modes when the corresponding β is in the range as in Eq. (2.1), only discrete values of β are allowed through, satisfying the required boundary conditions at the interfaces bounding the waveguide. These discrete values of β correspond to the various guided modes that can be grouped into two families: transverse electric (TE) and transverse magnetic (TM) optical modes. In general, the number of modes that the waveguide can support depends on the physical dimensions of the waveguiding region, the wavelength, and the spatial RI distribution [15].

The changes in the type of the optical mode describing the spatial distribution of the electric field as a function of the propagation constant β at a fixed wavelength λ are shown in Fig. 1 - considering a core possesses the highest RI, and a cladding possesses the lowest RI, i.e., $n_{\text{core}} > n_{\text{sub}} > n_{\text{clad}}$. The nature of the optical modes as a function of β [71] can be divided into the following four types: 1) For values in the range of $\beta > k_0 n_{\text{core}}$ (marked as I in Fig. 1), only a solution for the electric field with an exponential nature in the x-direction, in all three dielectric regions, could satisfy the required continuous boundary conditions. This mode is not physically realizable due to unlimited field increases in substrate and cladding, indicating infinite energy; 2) For values in the range of $k_0 n_{\text{core}} > \beta > k_0 n_{\text{sub}}$ (marked as II in Fig. 1), the solution for the electric field is sinusoidal in the core region but decaying exponentially in both substrate and cladding. The energy carried by these modes is confined inside the core or close to its surface boundaries. These modes are named guided modes - as the fundamental mode TE_0 and 2^{nd} order mode TE_1 (marked in red in Fig. 1); 3) For values in the range of $k_0 n_{\text{sub}} > \beta > k_0 n_{\text{clad}}$ (marked as III in Fig. 1), the solution for the electric field is exponentially decaying in the cladding but has an oscillatory nature in the core and substrate regions. These kinds of modes are classified as substrate radiation modes. The energy lost from the waveguiding region to the substrate as they propagate - an unwanted characteristic for signal transmission but may be primarily valuable for coupling applications; 4) For values in the range of $k_0 n_{\text{clad}} > \beta > 0$ (marked as IV in Fig. 1), the solution for the electric field has an oscillatory nature in the x-direction, in all three dielectric regions, resulting in radiation modes - the energy leaks from the waveguiding region to both the substrate and cladding regions. Since the lower limit $\beta = k_0 n_{\text{sub}}$ represents the critical condition under which the field is dissipated as a radiation mode (i.e., becomes a non-guided mode), it defines the cutoff condition - a cutoff frequency ω_c below which waveguiding cannot occur (or above a cutoff wavelength λ_c).

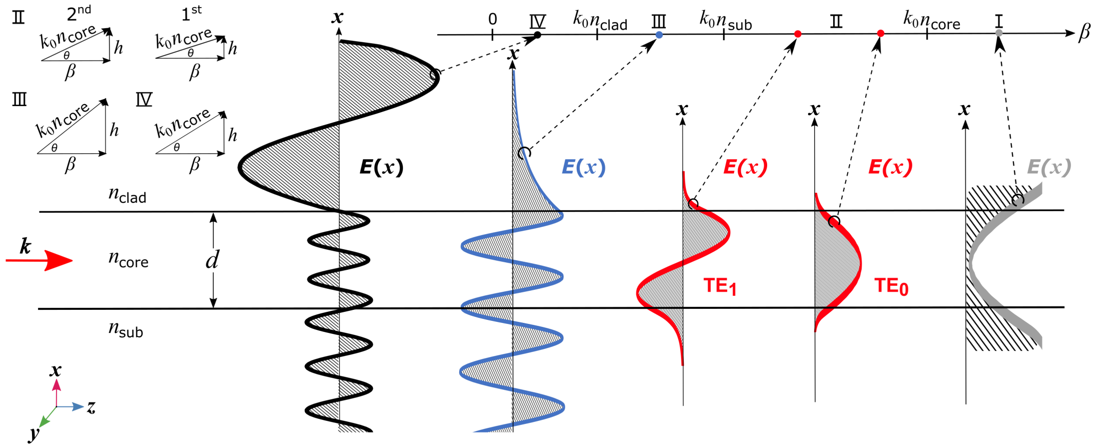

Figure 1 | Diagram of different types of optical modes in a slab waveguide. The modes' nature as a function of the propagation constant β at some fixed wavelength. The corresponding electric field distributions $E(x)$, and wavevector diagrams for four types: 1) a mode I (gray) in the range of $n_{\text{eff}} > n_{\text{core}}$ is not physically realizable; 2) the modes II (red) in the range of $n_{\text{core}} > n_{\text{eff}} > n_{\text{sub}}$ are confined modes supported by the waveguide, such as the TE_0 and TE_1 guided modes; 3) a mode III (blue) in the range of $n_{\text{sub}} > n_{\text{eff}} > n_{\text{clad}}$ is a substrate radiation mode; 4) a mode IV (black) in the range of $n_{\text{clad}} > n_{\text{eff}} > 0$ is a radiation mode of the waveguide. The wavevector $\boldsymbol{k}$ (red arrow) indicates the propagation direction of the light.

Although a slab waveguide is employed in various on-chip photonic applications and is possibly considered the basic element of more complex waveguiding structures due to its fundamental geometry, numerous integrated photonics applications require two-dimensional optical confinement. Rectangular waveguides consist of a core with rectangular or square cross-section shapes immersed in several dielectric media. Usually, these waveguides contain at least three regions: the core (a.k.a. guiding layer) in which the light is confined, surrounded by a cladding, and both are in contact with a substrate. The RI of the waveguide core n_{core} is higher than the RI of the adjacent substrate n_{sub} and cladding n_{clad} (i.e., $n_{\text{core}} > n_{\text{sub}} \geq n_{\text{clad}}$) to satisfy the guiding condition in Eq. (2.1). The typical geometry of a wire waveguide (a.k.a. ridge waveguide) is schematically shown in Fig. 2, contains a core with a small index step $\Delta n = 0.02$ between the core and the substrate; and the guiding layer immersed in the air (or cladding). Both mediums are in contact with the lithium niobate (LiNbO_3) substrate. These waveguides support a discrete number of guided modes which can be grouped into two families: quasi-TE (a.k.a. TE-like or E^x_{mn}) and quasi-TM (a.k.a. TM-like or E^y_{mn}). A 1D waveguide configuration, such as a slab waveguide, can support either a pure TE or a pure TM mode. However, pure TE or TM modes do not exist in the case of 2D waveguide structures [70]. In particular, these waveguides support modes of two independent polarizations, with either the dominant magnetic (TM-like) or electric (TE-like) field component along the transverse direction. The dominant TE or TM polarization fraction is frequently used to label the optical modes for their characterization; otherwise, their dominant electric field component can be employed - E^y_{mn} or E^x_{mn}, respectively. The sub-indices m and n (integers) indicate the number of crossings of each field component with the x-axis and y-axis inside the core, respectively.

The electric field distributions of the first two order modes supported by the waveguide, TE_{00} and TE_{10}, are shown in Fig. 2, along with the electric field profile of each component as a function of the x- and y- directions. The main field components of the quasi-TE modes are E_x and H_y. In contrast, the main field components of the quasi-TM modes are E_y and H_x. The quasi-TM modes are qualitatively similar to the quasi-TE modes but differ quantitatively. The optical power corresponding to each mode is confined to the waveguide core. The propagating fields are confined primarily inside the guiding layer, where the field components have an oscillatory nature along both x- and y- directions inside the waveguide core. However, the field distributions also exhibit evanescent tails outside the waveguide core, decaying exponentially with distance from the core boundaries, as shown in Fig. 2. When the indices of refraction of both media adjacent to the core are similar (e.g., cladding-core-cladding for the x-direction in Fig. 2), the field profiles decay at similar rates - and symmetric field distributions are observed considering the $y = 0$ plane. Whereas for different indices of refraction (e.g., cladding-core-substrate for the y-direction in Fig. 2), the modes exhibit non-symmetric field distribution considering the $x = 0$ plane since the field profiles decay at different rates.

It is important to note that higher effective index modes are more tightly confined to the waveguide core and characterized by more rapidly decaying evanescent tails. In particular, as a distinct optical mode propagates along the waveguide, a portion of the mode penetrates the medium surrounding the waveguide core. This phenomenon is named evanescent wave (a.k.a. evanescent field) [15]. The decay of the field profile in the medium surrounding the waveguide core can be approximated by:

$$E \propto e^{-\frac{2\pi d}{\lambda}\sqrt{n_{\text{eff}}^2-n_i^2}}\,, \tag{2.2}$$

where E is the electric field amplitude at a distance d from the interface between the core and adjacent medium, λ is the wavelength of the light, n_{eff} is the mode effective index, and n_i is the RI of the adjacent medium. Namely, the amplitude of each field component is exponentially decaying in the i^{th} medium surrounding the core with exponential decay constants α_i. The penetration depth $\delta_p = 1/\alpha_i$ denotes the distance from the adjacent medium-core interface, at which the intensity of the optical field inside the material decays to e^{-1} (or about 37%) of its value at this surface. Hence, the evanescent fields in the waveguide can be evaluated by the penetration depth δ_p of the field, which is given by:

$$\delta_p^{-1} = \frac{2\pi}{\lambda}\sqrt{n_{\text{eff}}^2 - n_i^2}\,. \tag{2.3}$$

The evanescent fields of each optical TE and TM mode are quantitatively different because of the variance in their mode effective indices. For a small RI step Δn between the core and the substrate or cladding (i.e., $\Delta n/n_{\text{core}} << 1$), the TE and TM guided modes having the same order are almost degenerate - resulting in qualitatively similar evanescent fields. While degenerate modes have the same propagation constant value β, they are characterized by different polarization and other main field components. In general, highly confined modes for particular waveguide geometry can be achieved with increasing Δn and vice versa, along with less field leakage to the substrate and cladding.

In many cases, the wave equation analysis of a rectangular waveguide core immersed in different dielectrics can be achieved by the scalar wave equation:

$$\frac{\partial^2 E}{\partial x^2} + \frac{\partial^2 E}{\partial y^2} + \left[k_0^2 n^2(x,y) - \beta^2\right] E = 0 \tag{2.4}$$

where $n(x,y)$ is the spatial RI distribution of the waveguide structure. Upon appropriate boundary conditions, various analytical approximation methods have been developed to analyze the transmission characteristics of the waveguide and the field distributions corresponding to its optical modes [1, 8]. However, these approximate methods may not hold for devices having a variation of the structure along their propagation direction - such as changed cross-section shape and size; or involve more complex geometric designs, including unique cross-section shapes and non-symmetrical geometric shapes as usually employed in integrated photonics applications [72, 73] (e.g., the core is not precisely constructed of rectangular geometry). Therefore, numerical methods and techniques are required for solving the optical wave propagation for designing novel photonic devices - as provided by the rigorous treatment of the finite element method (FEM) [1, 70, 74], which gives a clear insight into the essential lightwave transmission mechanism in complex waveguide structures.

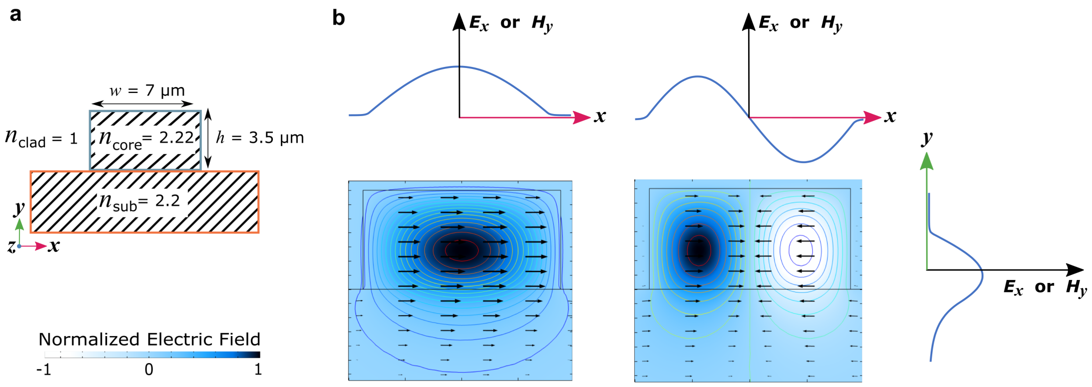

Figure 2 | Optical guided modes of typical wire waveguide structure. a, Transverse cross-sectional view (xy plane) of the waveguide. The waveguide core with cross-section sizes of 3.5×7 (μm)^2 is immersed in the air. Both mediums are in contact with the LiNbO$_3$ substrate. **b,** The electric field distributions and field profiles of the first two order modes supported by the waveguide: the fundamental (left) and the 2$^{\text{nd}}$ order (right) quasi-TE modes at a wavelength of 1550 nm. The arrow-, contour-, and surface- plots represent the transverse electric field $E^x_{mn}(x, y)$. Light is confined in the core and propagates in the z-direction.

2.1.2 Twisted Dielectric Waveguide with Rectangular Cross-Section

Twisting geometries can provide an additional degree of freedom for designing and forming light propagation characteristics of optical waveguides. In many cases, the transformation optics technique is employed to analyze optical structures of complex geometry, allowing rigorous modeling and designing of unique guided-wave devices, including both isotropic and anisotropic twisted waveguide architectures [75, 76]. Following the transformation optics technique, any modification in the original coordinate system can be described as an equivalent modification in the media optical parameters represented by the corresponding permittivity ε and the permeability μ. In other words, the interpretation of Maxwell's equations in different coordinate systems is equivalent to changing the medium parameters in the constitutive relationships.

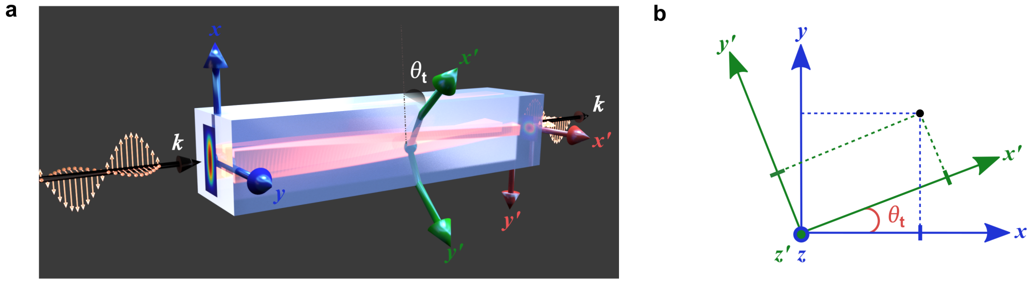

Figure 3 | The geometrical structure of a twisted waveguide in a twisted coordinate system. a, 3D schematic representation of the twisted rectangular waveguide made of transparent glass. The waveguide core is uniformly twisting along the z-axis with 90° twisting angle between the input and output facets; and is surrounded by a dielectric material with a lower RI. A polarized incident light illuminates the input facet of the waveguide. The wavevector $\boldsymbol{k}$ indicates the propagation direction of the light. **b,** The displacement of the physical points in each "z" cross-section takes place along x'- and y'- axes. The x'- and y'- axes (green) rotate around the z-axis by a twisting angle of θ_t relative to the x- and y- axes (blue) at the input facet of the waveguide.

A 3D twisted guided-wave configuration provides a spatially inhomogeneous structure for guiding the optical EM waves in a definite direction. The twisted waveguide can be characterized by a transverse spatial dependency of its dielectric function distribution which also varies along the propagation direction of the light. The concept of the twisted waveguide with a uniformly twisting waveguide core along the z-direction is illustrated in Fig. 3a. Similarly to a typically buried waveguide geometry, the guiding layer of the twisted waveguide is immersed in a dielectric material - the RI of the waveguide core n_core is higher than the adjacent cladding n_clad to satisfy the guiding condition in Eq. (2.1). In addition, the waveguide core has a modified cross-section shape in the propagation direction of the light; specifically, the waveguide core with a rectangular cross-section geometry rotates along its optical axis. The transverse cross-sectional of the twisted waveguide has a symmetrical geometry. The twisted waveguide is made of a transparent dielectric material in which the media properties are linear, time-independent, independent on the electric $\boldsymbol{E}$ and the magnetic $\boldsymbol{H}$ fields, and lack of free carriers and absorption (i.e., lossless media). In the case of isotropic media, the material properties can be represented by the scalars permittivity $\varepsilon = \varepsilon_r \varepsilon_0$ and permeability $\mu = \mu_r \mu_0$. Here, ε_r denotes the relative permittivity, ε_0 is the vacuum permittivity, μ_r denotes the relative permeability, and μ_0 is the vacuum permeability. Since most conventional materials are non-magnetic at optical frequencies, the relative permeability can be assumed to be unit $\mu_r = 1$, and therefore $\mu = \mu_0$. The twisted coordinate system employed to analyze the waveguide geometry is depicted in Fig. 3b, where the x'- and y'- axes are rotated around the z-axis by a twisting angle θ_t with respect to the x- and y- axes associated with the input facet of the waveguide. The length of the twisted region of the waveguide required to achieve a certain twisting angle θ_t is denoted by the twisted length l_t.

In general, in the 3D Euclidean space - the coordinate transformation between the original Cartesian basis $\{x, y, z\}$ and the new twisted basis $\{x', y', z'\}$ is related by the inverse of the Jacobian matrix $\mathbf{J}^{-1}$:

$$\mathbf{J}^{-1} = \begin{bmatrix} \frac{\partial x'}{\partial x} & \frac{\partial x'}{\partial y} & \frac{\partial x'}{\partial z} \\ \frac{\partial y'}{\partial x} & \frac{\partial y'}{\partial y} & \frac{\partial y'}{\partial z} \\ \frac{\partial z'}{\partial x} & \frac{\partial z'}{\partial y} & \frac{\partial z'}{\partial z} \end{bmatrix} , \tag{2.5}$$

Thus, the optical field and the optical properties of the materials in the twisted coordinate system $\{x', y', z'\}$ can be related to their respective counterparts in the original coordinate system $\{x, y, z\}$. In particular, the relationship between the medium permittivity tensor in the twisted coordinate system $\boldsymbol{\varepsilon}'$ and the medium permittivity in the original Cartesian coordinates $\boldsymbol{\varepsilon}$ is given by:

$$\boldsymbol{\varepsilon}' = \frac{\mathbf{J}^{-1}\boldsymbol{\varepsilon}\mathbf{J}^{-T}}{\det(\mathbf{J}^{-1})} , \tag{2.6}$$

where $\mathbf{J}^{-T}$ produces the transpose of $\mathbf{J}^{-1}$. A similar relation holds for the medium permeability tensor $\boldsymbol{\mu}'$ in the new coordinate system and the medium permeability in the original Cartesian coordinate system $\boldsymbol{\mu}$. Eq. (2.6) and the corresponding relation for $\boldsymbol{\mu}'$ are known as the material interpretation of the coordinate transformation - which allows EM phenomena in the transformed space to be analyzed in real space using the transformation media. In particular, the transformation optics technique utilizes the fact that in electromagnetism, a modification in the coordinate system from $\{x, y, z\}$ to $\{x', y', z'\}$ is equivalent to appropriate changing the material properties [77]. Hence, transformation optics can be employed to reduce the required dimensionality of some complex photonic problems - by choosing a coordinate system in which the waveguide geometry and its material properties become independent of one of the coordinates. The structure of a twisted dielectric waveguide with a rectangular cross-section shape can be simplified in the twisted coordinates $\{x', y', z'\}$[76] - which are related to Cartesian coordinates by:

$$\begin{cases} x' = x\cos(\alpha_\mathrm{t} z) - y\sin(\alpha_\mathrm{t} z) \\ y' = x\sin(\alpha_\mathrm{t} z) + y\cos(\alpha_\mathrm{t} z) \\ z' = z \end{cases} , \tag{2.7}$$

where $\alpha_\mathrm{t} = 2\pi/\Lambda_\mathrm{t}$ denotes the twisting rate with units of rad/m. The twisting rate defines the clockwise rotation of the x'- and y'- axes of the twisted coordinate system around the z-axis by the twisting angle of $\theta_{\mathrm{t}} = -\alpha_{\mathrm{t}} z$ with respect to the x- and y- axes of the original Cartesian coordinate system. Here, Λ_{t} is the twisted length corresponding to a full rotation angle where x' and y' axes rotate 360° around the z-axis at a distance of $z = \Lambda_{\mathrm{t}}$. Eq. (2.7) shows that all lines parallel to the z-axis in the twisted coordinate system behave as helices with a pitch distance equal to Λ_{t} in the original Cartesian coordinate system. According to Eq. (2.5, in conjunction with Eq. (2.7), the inverse of the Jacobian matrix $\mathbf{J}^{-1}$ is given by:

$$\mathbf{J}^{-1} = \begin{bmatrix} \cos(\alpha_{\mathrm{t}} z) & -\sin(\alpha_{\mathrm{t}} z) & -\alpha_{\mathrm{t}} \left[x \sin(\alpha_{\mathrm{t}} z) + y \cos(\alpha_{\mathrm{t}} z) \right] \\ \sin(\alpha_{\mathrm{t}} z) & \cos(\alpha_{\mathrm{t}} z) & \alpha_{\mathrm{t}} \left[x \cos(\alpha_{\mathrm{t}} z) - y \sin(\alpha_{\mathrm{t}} z) \right] \\ 0 & 0 & 1 \end{bmatrix} = $$

$$= \begin{bmatrix} 1 & 0 & -\alpha_{\mathrm{t}} y' \\ 0 & 1 & \alpha_{\mathrm{t}} x' \\ 0 & 0 & 1 \end{bmatrix} \begin{bmatrix} \cos(\alpha_{\mathrm{t}} z) & -\sin(\alpha_{\mathrm{t}} z) & 0 \\ \sin(\alpha_{\mathrm{t}} z) & \cos(\alpha_{\mathrm{t}} z) & 0 \\ 0 & 0 & 1 \end{bmatrix}, \tag{2.8}$$

where $\det\left(\mathbf{J}^{-1}\right) = 1$. When the material properties of a twisted waveguide are isotropic, they can be expressed with scalars permittivity ε and permeability μ. Thus, following Eq. (2.6) in conjunction with Eq. (2.8), the equivalent $\boldsymbol{\varepsilon}'$ in the twisted coordinate system $\{x', y', z\}$ has the unique representation of the form:

$$\boldsymbol{\varepsilon}'\left(x', y', z\right) = \varepsilon\left(x', y', z\right) \begin{bmatrix} 1 + \alpha_{\mathrm{t}}^2 y'^2 & -\alpha_{\mathrm{t}}^2 x' y' & -\alpha_{\mathrm{t}} y' \\ -\alpha_{\mathrm{t}}^2 x' y' & 1 + \alpha_{\mathrm{t}}^2 x'^2 & \alpha_{\mathrm{t}} x' \\ -\alpha_{\mathrm{t}} y' & \alpha_{\mathrm{t}} x' & 1 \end{bmatrix}. \tag{2.9}$$

where ε and $\boldsymbol{\varepsilon}'$ denote the corresponding permittivity values expressed in the Cartesian coordinate system and the twisted coordinate system, respectively. Here, the coordinates $\{x', y', z\}$ indicate the position in space. As seen from Eq. (2.9), the equivalent permittivity in the twisted coordinate system $\boldsymbol{\varepsilon}'\left(x', y', z\right)$ is z-independent in the case the $\varepsilon\left(x', y', z\right)$ can be described as $\varepsilon\left(x', y'\right)$.

2.2 Saturable Absorption

A saturable absorber is a material with a nonlinear absorption coefficient that decreases as the intensity of the applied optical field increases (or exhibits increased transmittance as the incident light intensity increases). When the intensity of the applied optical field on the saturable absorber is relatively weak, a photon of larger energy may be absorbed depending on allowed energy levels, and a carrier is excited from the ground to a higher energy atomic level causing the absorption of light. Due to the plenty of ground-state population of absorbent carriers, on the one hand, the material can still absorb more photons [78]. On the other hand, if the excited-state lifetime is long enough and the intensity of the applied optical field upon the saturable absorber is increasing, such that the excited-state carriers are not decaying fast enough to allow reabsorption (i.e., to participate in the absorption process again); and simultaneously more carriers may be excited - consequently, these mechanisms can cause the saturation of absorption. In other words, these mechanisms can increase transmission as the intensity of the incident light increases (i.e., nonlinear transmittance), which is attributed to saturable absorption behavior.

In general, considering an instantaneous dielectric response in an isotropic material, the optical response can be characterized by expressing the polarization $P(t)$ (or dipole moment per unit volume) as a power series in the strength of the applied optical field $E(t)$ which is given by:

$$P(t) = \varepsilon_0 \left(\chi^{(1)} E(t) + \chi^{(2)} E^2(t) + \chi^{(3)} E^3(t) + \cdots \right), \tag{2.10}$$

where $P(t)$ and $E(t)$ are scalar quantities, ε_0 is the vacuum permittivity, $\chi^{(1)}$ is the linear susceptibility, and $\chi^{(2)}$ and $\chi^{(3)}$ are second- and third-order nonlinear optical susceptibilities, respectively [4]. The third-order nonlinearity $\chi^{(3)}$ can be associated with the third harmonic generation process, changes in RI (a.k.a. nonlinear Kerr effect), and nonlinear absorption (i.e., saturable absorption and multi-photon absorption). The changes in RI and optical absorption depend on the intensity of the applied optical field. Hence, the complex RI $\tilde{n}$ has a representation of the form [4, 79]:

$$\tilde{n} = n_0 + n_2 I - j \frac{\lambda}{4\pi} \left(\alpha_0 + \alpha_2 I \right), \tag{2.11}$$

where I is the intensity of the applied optical field, n_0 is the linear RI, n_2 is the nonlinear RI (a.k.a. Kerr coefficient), α_0 is the linear absorption coefficient, and α_2 is the nonlinear absorption coefficient. While the n_2 can be related to the real part of $\chi^{(3)}$, the α_2 can be associated with the complex part of $\chi^{(3)}$ by the relations:

$$n_2 = \frac{1}{c n_0^2 \varepsilon_0} \frac{3}{4} \operatorname{Re}\left(\chi^{(3)} \right), \quad \alpha_2 = \frac{-\omega}{c^2 n_0^2 \varepsilon_0} \frac{3}{2} \operatorname{Im}\left(\chi^{(3)} \right). \tag{2.12}$$

where ω denotes the frequency, and c is the speed of light in vacuum.

Saturable absorption is a phenomenon related to the imaginary part of $\chi^{(3)}$ [4, 79] as expressed in Eq. (2.12), where the material nonlinear absorption coefficient decreases as the intensity of the applied optical field increases. Despite Eq. (2.10), this power series expansion in some cases does not converge; therefore, other methods to describe different nonlinear optical effects are required [4]. Such a case is saturable absorption, which can be defined in terms of an intensity-dependent absorption coefficient $\alpha(I)$ at a given wavelength by the relation:

$$\alpha(I) = \frac{\alpha_0}{1 + I/I_\mathrm{S}} , \tag{2.13}$$

where α_0 is the weak-field absorption coefficient (a.k.a. the linear absorption coefficient), I_S is the saturation intensity, and $I = 2n\varepsilon_0 c|E|^2$ is the intensity of the applied optical field E [4]. The intensity of the incident light at which the absorption coefficient is half of the optical loss difference (i.e., $\alpha = \alpha_0/2$) is defined as the saturation intensity. When the intensity of the applied optical field is relatively weak $I << I_\mathrm{S}$, absorption of more photons occurs by the saturable absorber resulting in intensity attenuation of the light passing through the material. In addition, Eq. (2.13) can be expanded in a power series to obtain:

$$\alpha = \alpha_0 \left[1 - (I/I_\mathrm{S}) + (I/I_\mathrm{S})^2 - (I/I_\mathrm{S})^3 + \cdots\right] , \tag{2.14}$$

In principle, most saturable absorbers are imperfect since the saturation of absorption does not ideally lead the attenuation of the light intensity to zero. Namely, these do not absorb completely the light passing through the sample, and a portion of the incident light is transmitted through the material.

$$\alpha(I) = \frac{\alpha_0}{1 + I/I_\mathrm{S}} + \alpha_\mathrm{ns} . \tag{2.15}$$

where α_ns is the non-saturation component of the optical absorption [4, 79]. The saturable absorber property is shown in Fig. 4, along with the various essential parameters. Consider the normalized intensity is defined as I/I_S, and $\alpha_0 d = 0.1$. The normalized absorption is defined as $\left(1 - e^{-\alpha d}\right) / \left(1 - e^{-\alpha_0 d}\right)$, since the non-absorbed light after transmitted through a material sample with a thickness of d is $Ie^{-\alpha d}$. Fig. 4 demonstrates the intensity dependence of the attenuation of the light passing through a saturable absorber - the absorption coefficient decreases as the intensity of the applied optical field increases.

Many 2D materials exhibit increased light transmission by increasing the intensity of the applied optical field via a saturable absorption behavior in the nonlinear regime [79, 80]. Recently, $\mathrm{Ti_3CNT}_x$ was found to exhibit a nonlinear absorption coefficient (i.e., increased transmittance at higher light fluences) [33, 81, 82]. Besides, it is reported in Ref. [33] that the saturation fluence and the modulation depth of $\mathrm{Ti_3CNT}_x$ (MXene) depend on the film thickness.

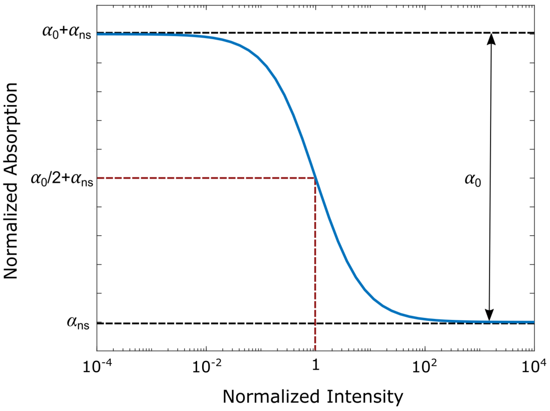

Figure 4 | Saturable absorption property. Nonlinear absorption coefficient of a saturable absorber as a function of normalized intensity of the incident light I/I_S. The coefficient α_0 denotes the total optical loss difference, and α_ns is a non-saturation component of optical loss.

2.3 Photonic Deep Structured Learning Principles

NN approaches play an essential role in artificial intelligence models, widely employed in a broad range of fields due to their effective capability in the massive data processing. Current NN hardware systems are still electronics-based and exhibit extensive implementations of different deep structured learning architectures for numerous machine learning computation tasks. However, computing and data processing capabilities are fundamentally limited by their integration size and power consumption, along with the approaching limit of Moore's law - where exponential behavior of the transistors' number in a dense integrated circuit is approaching its physical limitation [83]. Thus, developing the new generation computing method is highly required despite the present domination of electronic hardware implementations. The utilization of integrated photonics for NN applications offers a promising alternative approach to conventional microelectronic implementations, thanks to both computational speed and low energy consumption improvements in deep learning computing tasks. Unlike traditional electronic-based interconnects, photonic NNs are constructed by guided-wave optics to execute linear and nonlinear optical computing. Due to the photon nature as elementary excitation of the EM field, photonic NNs present an extraordinary potential for parallel processing, allowing multiple computations simultaneously without being susceptible to EM interferences. Moreover, the manipulations of light allow performing the calculations simultaneously when the information propagates via the photonic circuit, decreasing repeated handling of the information and memory usage while improving speed processing and low latency.

2.3.1 Photonic Neural Network Mechanism of Operation

Fundamentally, an artificial neuron includes a summation of multiple weighted input signals followed by nonlinear AF. Namely, each neuron in the photonic deep structured learning system acts as a mathematical operation incorporating linear and nonlinear processes, as shown in Fig. 5. Therefore, the optical realization of photonic deep structured learning system falls into two significant steps: 1) implementing the linear operation via optical interference unit (OIU), and 2) introducing the nonlinearity of the network via optical nonlinearity unit (ONLU). For multiple weighted $W_{ij}^{(l)}$ input signals $n_j^{(l-1)}$ arriving from the output of neurons in the previous layer with the addition of a bias $b_i^{(l)}$, the output of the OIU of the i^{th} neuron $n_i^{(l)}$ in the layer l^{th}, is given by a linear combination across all the inputs:

$$X_{\text{OIU}}{}_i^{(l)} = b_i^{(l)} + \sum_j W_{ij}^{(l)} n_j^{(l-1)} \quad , \tag{2.16}$$

Then, the photonic neuron generates a new optical output signal processing the multiple optical weighted inputs signals $X_{\text{OIU}}{}_i^{(l)}$ through the nonlinear AF. The neuron output is expressed by:

$$n_i^{(l)} = f_{\text{NL}}\left(X_{\text{OIU}}{}_i^{(l)}\right) \ . \tag{2.17}$$

In practice, the photonic neuron achieves linear and nonlinear computations via manipulating and controlling the light by changing its phase and intensity through its propagation through the designed photonic circuit. The photonic neuron must respond to multiple optical inputs, be able to apply a nonlinearity to the optical signals, and produce an optical output suitable to drive other photonic neurons in the subsequent layer.

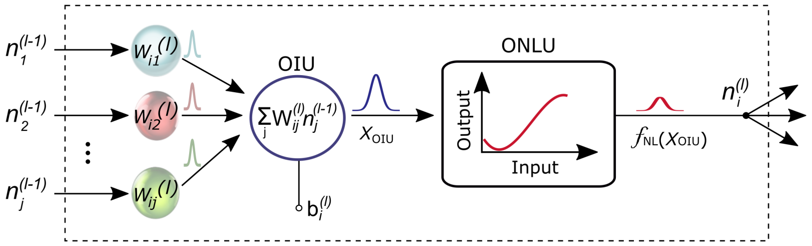

Figure 5 | Schematic diagram of neuron mechanism of operation. The input optical signals arrived from neurons in the previous layer are weighted and combined via OIU (X_{OIU}, blue circle). Then, a nonlinear AF is applied to the summation signal via ONLU (f_{NL}, black rectangle). Finally, the output is employed as an input for other neurons in the successive layer.

Once the operation principles of a single photonic neuron are established, a deep structured learning system can be assembled. The NN system is a collection of photonic neurons arranged in individual layers. A general deep structured learning architecture that consists of at least one hidden layer between the input and output layers is shown in Fig. 6 together with its decomposition into individual layers. The NN system could be defined as a function: $f : \mathbb{R}^n \rightarrow \mathbb{R}^m$, where n and m $(n, m \geq 1)$ are the number of neurons in the input and output layers, respectively. The NN system is characterized by its neural parameters (i.e., weights and AF) and the organization of neurons for producing an output according to received inputs. Deep structured learning architecture contains interconnected neurons that do not form a cycle is called feedforward NN (FFNN). Specifically, the neurons connect only to different neurons in successive layers, usually arranged in fully-connected layers. The information is transmitted unidirectionally through the NN circuit from the input to the output layer. Hence, a matrix multiplication must be executed to satisfy the multiplication and accumulation implementations before passing through the nonlinearity unit.

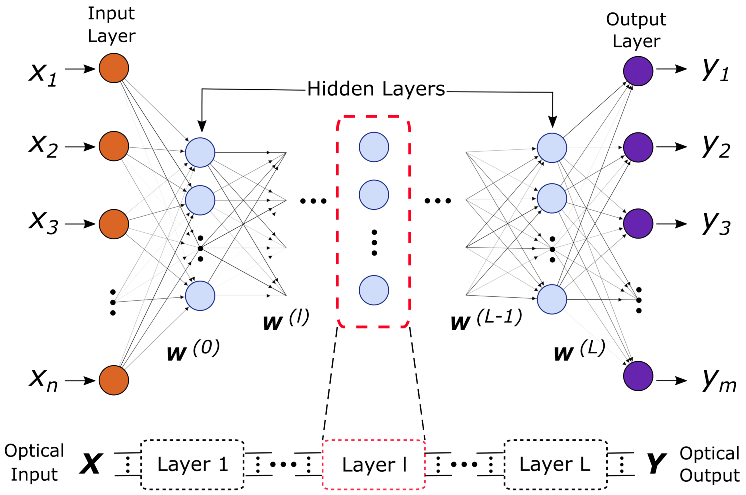

Figure 6 | Decomposition of the NN architecture into individual layers. The neurons are embodied in each layer of the system, where several hidden layers (light-blue circles) are placed between the input layer $\boldsymbol{X}$ (orange circles) and the output layer $\boldsymbol{Y}$ (purple circles). The corresponding layers in the block diagram represent the complete neural architecture.

In general, the NN system learns how to map between input and output in a complex way by modifying its weights based on previous examples. In particular, all the inputs embody the information pass forward through the network to compute the output, namely, feeding a training dataset into the network (so-called forward propagation). Then, the network weights are subsequently optimized using a model error calculated by the difference between the computed output and the actual dataset labels (so-called backpropagation). In the case of injecting extensive information simultaneously, the challenge is to distinguish between relevant and irrelevant pieces of information because not all are equally valuable. Thus, nonlinear AF plays a key role in deep structured learning by enabling the network to use important information and concurrently suppress irrelevant information.

2.3.2 Optical Interference Unit for Linear Operation

The essence of realizing the OIU is to complete the linear operation, namely the matrices multiplication. Thus, a realistic OIU building block must be implemented as a whole layer in photonic NN models. $X_{\mathrm{OIU}}^{(l)}$ is carried out through the forward propagation procedure to satisfy $X_{OIU}^{(l)} = W^{(l)}Y^{(l-1)}$, where $Y^{(l-1)}$ represents all the outputs of the previous layer's neurons. In practice, the photonic NN building block implementations can be deployed to a large scale to implement arbitrary deep structured learning dimensions and depth optically.

An OIU can be realized using various integrated photonics architectures to implement matrices multiplication for achieving weighting and summation of input optical signals. These utilize light propagation in optical waveguides and integrated guided-wave optics devices to manipulate and control the phase and intensity of the optical signal to complete the linear operation. Due to their passive functionality nature [84], the linear computation can be carried out without energy consumption. The physical implementations fall into two major categories: optical modes realization, such as linear operation nanophotonics circuits [85], and multiwavelength realization, such as parallel weighting of optical carrier signals generated from wavelength-division multiplexing using microring resonators weight banks [86]. In particular, the weighted input signals can be obtained with a mesh of integrated MZIs, each formed of waveguides and 50:50 directional couplers combined with phase shifters (i.e., applying an electric field on one MZI's arm to modify the RI of the waveguide's material) [87, 88]. Where any unitary transformations can be implemented with conventional optical beam splitters and phase shifters [89], a rectangular diagonal matrix can be implemented with optical attenuation achieved by optical intensity modulator. Coherent monochromatic light from multiple channels propagates paralleled through the MZIs in which the differential output phase changes and, therefore, the optical signal's intensity is adjusted, and the output signals eventually yield the linear computing outcome.

Alternatively, polychromatic light is injected into the waveguide combined with various microring resonators operating at different wavelengths, acting as filters that form a channel carrying a signal with a specific wavelength. The optical signals are weighted using phase-change material cells and are summed using a WDM multiplexer [90, 91], and consequently, the linear operation is completed. Furthermore, an OIU implementation that relies on free-space diffractive optical systems has already been shown [92, 93] along with implementations in the spectral domain [94, 95]. When diffraction light interference implements the weighting of the optical signals, their summation is achieved through combined transmission (or reflections) coefficients at each point on a given transmissive layer that acts as an individual neuron.

It is worth mentioning that there are other forms of deep structured learning architectures capable of accomplishing various computing applications, such as convolutional NN (a.k.a. CNN), recurrent NN (a.k.a. RNN), and others. The mode of operation of CNN is to complete convolution operations utilizing its unique hidden layers in addition to the fully-connected layers in the corresponding FFNN. Different optical accepts proposed to realize CNN [96], including utilizing diffractive optical elements [97], incorporating integrated photonics reconfigurable linear processors [98], and combining microring resonator weight bank with wavelength division multiplexing [99]. On the other hand, RNN contains numerous configurations in which interconnections between neurons form a temporal sequence of directed or undirected pathways that allow its dynamic behavior. It can be realized using a coherent integrated photonics processor [100] or a diffractive optoelectronic processor [101].

In addition, it needs to be emphasized that both optical free-space and integrated photonics computing architectures should concurrently establish for large-scale deployment of the all-optical deep structured learning in a broad range of fields. The main advantages of free-space NN implementations allow a more straightforward realization of many neurons and a larger computing scale to examine further complex models and additional optical computing techniques. However, they have higher requirements for the integrated environment, construct via bulky optical setups, and are possibly more susceptible to error if the beams are not perfectly aligned. In contrast, integrated photonics NN implementations are a miniaturization of the neuron dimensions, a phase-stable and robust platform to implement complex photonic circuits, higher computational speed, and stability for the integrated environment without being susceptible to EM interference.

2.3.3 Optical Nonlinearity Unit

Based on the linear operation, NN is limited in its performance and can only deal with simple problems. The nonlinear AF is the essence of the NN's powerful expression ability. Namely, it influences the network's speed (in terms of data and epochs it needs) and the accuracy of the task it performs. Thus, an OIU alone is insufficient for a photonic device to act as a building block in deep structured learning applications, and some optical nonlinearities must be introduced in the system. It needs to be emphasized that there is no one best AF for all the NN architectures' computing tasks. Individual AF may be better in some cases but may be worse in others. Therefore, different optical AFs (i.e., shape) implementations are required due to the different computing tasks. ONLU implementation tries to mimic the software-based AFs commonly used in deep structured learning models by achieving optical transfer functions representing the photonic device's nonlinear optical responses. Fig. 7 shows several of the commonly used software-based AFs such as rectified linear unit (ReLU), exponential linear unit (ELU), hyperbolic tangent (tanh), and swish function. In general, software-based nonlinear AFs define a nonlinear output to input relation, which is specified with unitless. In contrast, realistic optical transfer functions represent the photonic device's nonlinear responses by output-to-input power relationships. While the optical transfer functions are specified with arbitrary units (e.g., transmittance), the input and output power values are in the context of spectral quantities, which are specified with units of mW/nm (or dBm/nm).

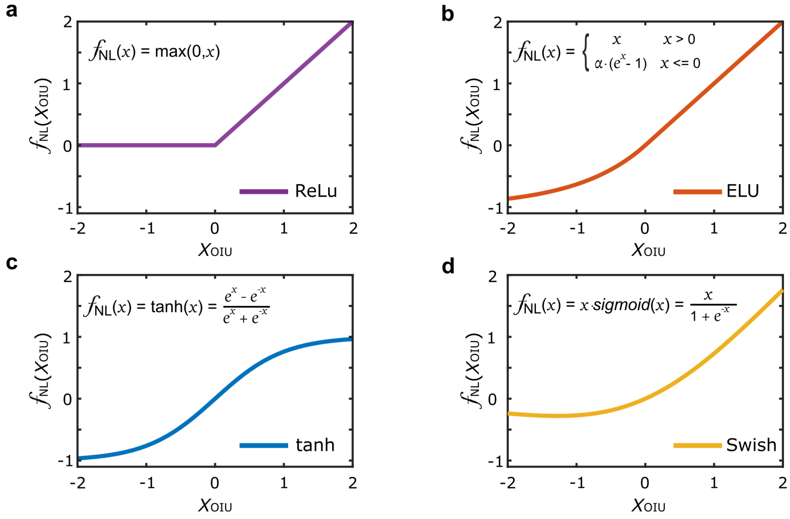

Figure 7 | Different common software-based nonlinear AFs. The nonlinear transfer functions: ReLu (**a**), ELU (**b**), tanh (**c**), and Swish (**d**) are represented by input-to-output relationship.

A general photonic deep structured learning system realization diagram is shown in Fig. 8. The input optical signal is generated via laser, and the optical splitters and optical modulation are used to encode the information, usually in the intensity of the optical signal. Next, the light propagating through the optical circuit implements the NN system. After each neuron linear operation (i.e., matrix multiplication), the ONLU must be integrated into each layer. Each layer of the NN is composed of optical interference and nonlinearity units, representing a building block in photonic NN. This process repeats for each layer constructed in the photonic deep structured learning model. Eventually, the optical signal is converted to an electrical signal via photoelectric detectors for future integration with the current microelectronics.

Since there are insufficient implementations for all-optical nonlinear AF, the nonlinear operation hardware is still electronic-based, incorporating photoelectric and electro-optical conversions to execute the required optical nonlinear computing. These lead to higher energy consumption and limit the computational speed of the photonic deep structured learning system. An ideal all-optical AF must be capable of implementing the nonlinear calculation by manipulating the intensity of the optical signal as the light propagates through the photonics device. With the ability to produce tailormade AF and simple integration, this configuration can significantly improve the response and decrease the system's latency.

Practical photonic devices capable of exhibiting nonlinear transfer functions to implement advanced optical nonlinear AF mechanisms can be divided into three major categories: 1) electronics -based devices, 2) utilizing electro-optic effects, and 3) all-optical driven techniques via light-matter interaction. The mechanism of operation of the electronics-based devices is based on converting the input optical signal to an electrical signal proportional to the detected incident optical power. This follows by executing the nonlinear activation via digital computing on the electronic signal, eventually converting it into an optical signal proportional to the incident electrical power. The nonlinear activation can be realized with the help of standard electronics hardware such as the CPU [87, 88], passing a voltage signal through a component that has an electrical nonlinear transfer function [102], etc. However, these configurations result in slower computational speed, higher power consumption, and additional noise on both devices and system levels. In contrast, optoelectronic-based devices directly apply the application of AF to the intensity of the optical signal. These rely on controlling the transmission spectrum of the optical signal through electro-optics effects to achieve nonlinear activation. Accordingly, the manipulation of the light can be obtained by incorporated devices such as an electro-optic intensity modulator [103, 104], an electro-optic absorption modulator [105], a photodetector employing the photoelectric effect [101], and a mesh of semiconductor optical amplifier [106, 107]. However, these configurations are bulky, challenging to integrate, and require electrical and temperature controls.

The devices based on all-optical driven methods via light-matter interactions are ideal for taking advantage of all-optical deep structured learning. The basic principle relies on light-matter interaction, where the incident light changes the material's or structure's optical properties and consequently influences the transmitted optical power via the photonic device. These include a theoretical work that presents an all-optical nonlinear AF based on nanophotonic structures exhibiting induced transparency and reverse saturated absorption [108], realization based on light-induced quantum interference effect among atomic transitions operating in free-space [109], semiconductor Fano lasers which have recently been predicted analytically to be realized as an all-optical nonlinear AF [110], and phase-change materials cell integrated on top of the waveguides construct a micro-ring resonator [90]. However, these configurations require special fabrication techniques for integrating on a chip, are sensitive to the operating wavelength of the incident light, and have increased conditions for the integrated environment. With the help of light-MXene interaction, the nonlinear AF can be realized in an all-optical manner employing the numerous nonlinear optical effects in MXene in different configurations for both free-space and integrated circuits implementations.

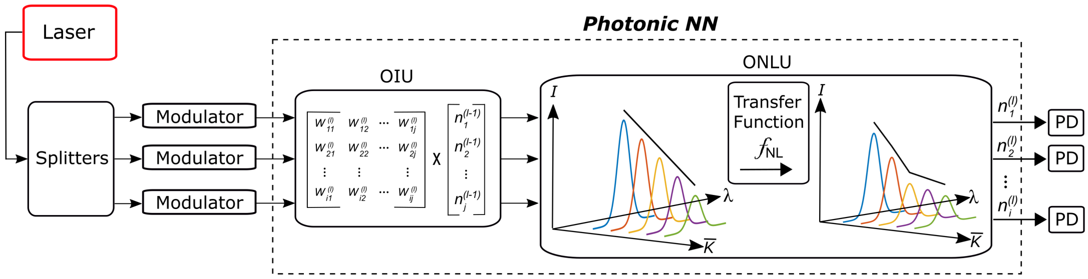

Figure 8 | Schematic diagram of a general photonic deep structured learning system. The photonic NN comprises OIU and ONLU assembling the NN layers (dashed line box), which implement the matrix multiplication followed by nonlinearity. The light source, optical splitters, and modulators form the encoded information carried by the optical signals. Each repeat of the NN building block (dashed line box) represents a fully connected layer. The optical-to-electrical conversion is carried out at the end utilizing photodetectors (PD) for further integration.

2.4 Basics of Photonic Quantum Computing

The quantum bit (qubit) is a fundamental element of quantum computing, the basic container of quantum information in quantum computers. It is the quantum generalization of the classical bit, the basic unit used to represent classical information in classical computers. In analogy to the classical bit - whose value is either 0 or 1, the qubit is a quantum mechanical system whose state is defined as a unit vector in the vector space $\mathbb{C}^2$. Moreover, an orthonormal basis must be selected to characterize a qubit state in the state space. The most frequently used basis is the standard basis (a.k.a. computational or x-basis): $\{|0\rangle, |1\rangle\}$. Using the bra-ket notation (a.k.a. Dirac's notation), $|0\rangle$ and $|1\rangle$ can be employed to represent the vectors $e_0 = \begin{bmatrix} 1 \\ 0 \end{bmatrix}$ and $e_1 = \begin{bmatrix} 0 \\ 1 \end{bmatrix}$, respectively. Hence, the qubit state can be formulated as a linear combination of the selected two basis states $|\psi\rangle = a_0 |0\rangle + a_1 |1\rangle$, where a_0 and a_1 are the complex amplitudes of the quantum state $|\psi\rangle$. Following the relationship of these amplitudes to probabilities (which should sum up to 1), the state vector needs to satisfy the normalization condition. Namely, the magnitude of the state vector should be 1, which can be written as $\langle\psi|\psi\rangle = 1$ and consequently equivalent to $|a_0|^2 + |a_1|^2 = 1$.

In general, the states $|0\rangle$ or $|1\rangle$ are analogous to the logical 0 and 1 that a bit may hold, respectively. While a classical bit represents a logical state with one of two possible values - 0 or 1, a qubit can be in a superposition of the two basis states. In other words, a classical bit can be described as a qubit being in only one state at any time, either $|0\rangle$ or $|1\rangle$. Although a qubit can be in a superposition of these two orthogonal states, observation or measurement change the qubit state. Specifically, it collapses into one of the two orthogonal states [111]. The amplitudes of the state $|\psi\rangle$ comprise information about the probability of the qubit being measured in a particular state. In particular, given an arbitrary state $|\psi\rangle$, this state has exactly $|a_0|^2$ probability of being measured in the state $|0\rangle$, and exactly $|a_1|^2$ probability of being measured in the state $|1\rangle$; by measuring the qubit state in the basis $\{|0\rangle, |1\rangle\}$. Once the qubit is measured, its original quantum state collapses to the measured state. For instance, if the outcome of measuring a qubit is the state $|1\rangle$, there is a 100% chance of finding the qubit in the state $|1\rangle$ in additional measurements. Namely, the acts of observing or measuring change the state of the qubit, which can be described by:

$$|\psi\rangle = \begin{bmatrix} a_0 \\ a_1 \end{bmatrix} \xrightarrow{\text{Measure } |1\rangle} |\psi\rangle = |1\rangle = \begin{bmatrix} 0 \\ 1 \end{bmatrix} . \tag{2.18}$$

The measurements are usually used when needed to extract an output and are typically placed at the end of the quantum circuit, either in practical implementations or simulations. A qubit state can be measured either in the basis in which it is prepared or a different basis can be used for carrying out the measurement. Another commonly used basis is the Hadamard basis (a.k.a. z-basis): $\{|+\rangle, |-\rangle\}$, where $|+\rangle = \frac{1}{\sqrt{2}}(|0\rangle + |1\rangle)$ and $|-\rangle = \frac{1}{\sqrt{2}}(|0\rangle - |1\rangle)$. Thus, the state may be expressed as a superposition of these two quantum states and is then written as $|\psi\rangle = \frac{a_0+a_1}{\sqrt{2}} |+\rangle + \frac{a_0-a_1}{\sqrt{2}} |-\rangle$.

Quantum gates are building blocks of quantum circuits that denote unitary operators acting on one or a small number of qubits, and their operations are reversible [112]. Below, three of the useful and fundamental quantum logic gates are introduced: the rotation, Hadamard, and Z gates. The rotation operator gate applies a rotation by θ on a single qubit state about the y-axis at the Bloch sphere and specified by:

$$R_\theta = \begin{pmatrix} \cos(\theta/2) & -\sin(\theta/2) \\ \sin(\theta/2) & \cos(\theta/2) \end{pmatrix}, \tag{2.19}$$

The Hadamard operator acts on a single qubit, usually utilized to create a uniform quantum superposition state, which maps the basis states $|0\rangle \mapsto \frac{|0\rangle+|1\rangle}{\sqrt{2}}$ and $|1\rangle \mapsto \frac{|0\rangle-|1\rangle}{\sqrt{2}}$. This operator is defined by $H|0\rangle = \frac{1}{\sqrt{2}}(|0\rangle + |1\rangle) = |+\rangle$ and $H|1\rangle = \frac{1}{\sqrt{2}}(|0\rangle - |1\rangle) = |-\rangle$, where:

$$H = \frac{1}{\sqrt{2}} \begin{pmatrix} 1 & 1 \\ 1 & -1 \end{pmatrix}. \tag{2.20}$$

Employing the rotation operation, the Hadamard gate can be represented as $R_{\pi/2} Z = H$, where Z is the Pauli Z-gate defined by $Z(a_0|0\rangle + a_1|1\rangle) = a_0|0\rangle - a_1|1\rangle$ (i.e., Z-gate leaves the basis state $|0\rangle$ unchanged and maps $|1\rangle$ to $-|1\rangle$).

The state of a single qubit and operations on it can be visualized geometrically, as depicted in Fig. 9, by the Bloch sphere (or Poincaré sphere in terms of a single photon polarization state as a qubit of information). A point on the sphere's surface characterizes a pure quantum state $|\psi\rangle = a_0|\leftrightarrow\rangle + e^{j\phi} a_1 |\updownarrow\rangle$, where an infinite number of such points are on the unit sphere. In particular, this visualization tool maps the 2D complex state vector (containing the amplitudes for the two qubit states) onto real 3D space ($a_0, a_1, \phi \in \mathbb{R}$). Any point on the unit sphere ($r = 1$, the qubit state magnitude is 1) can be interpreted in the context of the polar angle θ and azimuth angle ϕ. Since the state space is exponential in the number of qubits, visualization of more than one qubit is more complicated. Namely, a state of N qubits can be in a superposition of 2^N basis states and can be formulated as $|\psi\rangle = a_0|p_{00\ldots0}\rangle + a_1|p_{00\ldots1}\rangle + \ldots + a_{2^N-1}|p_{11\ldots1}\rangle$ such that $\sum_{i=0}^{2^N-1} |a_i|^2 = 1$. Accordingly, a joint state $|\psi\rangle$ of N qubits can be represented as a tensor product of these qubits $|\psi\rangle = |\psi_0\rangle \otimes |\psi_1\rangle \otimes \ldots |\psi_{N-1}\rangle = |\psi_0\psi_1\ldots\psi_{N-1}\rangle$.

Qubit states can be encoded utilizing different degrees of freedom of the single particle of light - photon, such as polarization [113, 114], optical path, transverse spatial field distribution [115], frequency and time bin [116]. An arbitrary state of a single qubit can be characterized using a complete orthonormal set of functions. In the case of polarization encoding, these are constituted of photons prepared in orthogonal polarization states such as horizontal and vertical polarization states. Generally, a photon polarization state can be depicted as a superposition of two basis states:

$$|\psi\rangle = \cos\left(\theta/2\right)|{\leftrightarrow}\rangle + e^{j\phi}\sin\left(\theta/2\right)|{\updownarrow}\rangle \ . \tag{2.21}$$

where $\leftrightarrow$ and $\updownarrow$ are the horizontal and vertical photon polarization states, respectively. The two variables express the amplitudes for the two states that the qubit can be: $\theta, \phi \in \mathbb{R}$. While ϕ denotes the relative phase between these states, θ embodies the real amplitudes of the normalized qubit states in terms of one variable. The corresponding orthogonal state of a certain state is given by: $\left|\psi^{\perp}\right\rangle = \sin\left(\theta/2\right)|{\leftrightarrow}\rangle - e^{j\phi}\cos\left(\theta/2\right)|{\updownarrow}\rangle$.

In principle, any pair of the orthogonal states $|\psi\rangle$ and $|\psi^{\perp}\rangle$ can be used for encoding the logical values 0 and 1. To find the certain qubit state embodied in the polarization state of a single photon associated with the bit value 0 or 1, the particular states that have been used to prepare it are required, namely, the two chosen variables ϕ and θ. Moreover, trying to gain the exact information from this single photon will disturb its polarization state (e.g., measure the qubit in a different basis), resulting damage the encoded quantum information.

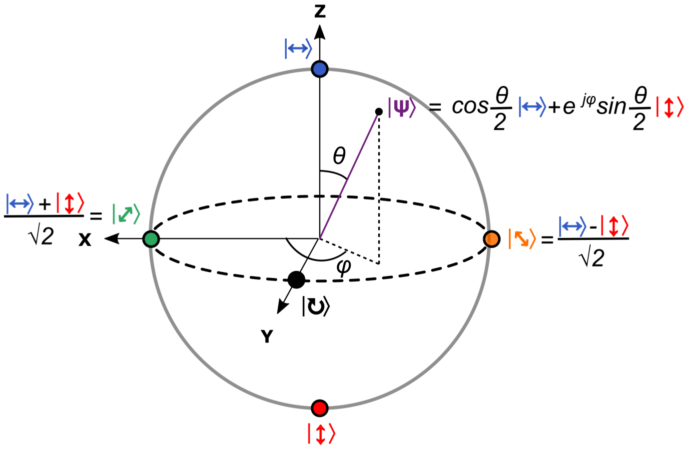

Figure 9 | Geometrical representation of a qubit state as the polarization state of a single photon. The photon's polarization state $|\psi\rangle = a_0|{\leftrightarrow}\rangle + a_1|{\updownarrow}\rangle$ is represented by a point on the sphere surface which can be described as a linear combination of $|{\leftrightarrow}\rangle$ and $|{\updownarrow}\rangle$ states with $a_0 = \cos(\theta/2)$ and $a_1 = e^{j\phi}\sin(\theta/2)$.

Any information can be encoded as a sequence that contains combination of 1's and 0's. This encoded information can be protected from forgery, as shown by Wiesner [38], by encoding classical information into quantum conjugate bases utilizing a unique quantum principle. Based on the no-clone theorem $|\psi\rangle \nRightarrow |\psi\rangle|\psi\rangle$, there is no procedure able to duplicate an arbitrary quantum state [39]. Namely, without knowing what particular states have been used (i.e., the encoding basis), there is no way to guess with certainty which bit value is associated with the particular qubit. For example, each of the qubits states $|0\rangle, |1\rangle, |+\rangle$, or $|-\rangle$ with equal probabilities can be used to encode this sequence of classical bits. While the logical 0 can be encoded with one of the quantum states in each basis $\{|0\rangle, |1\rangle\}$ and $\{|+\rangle, |-\rangle\}$, the logical 1 can be encoded with the other quantum state in each basis. In contrast to the classical world, the logical value associated with the bit can easily be measured; when randomly given one of the two pure states, there is no way of telling which is provided with probability more than 3/4 [117], and therefore, it cannot be certainly copied. Besides, the security of this quantum scheme is exponential in the number of qubits N, i.e., there is no way of deterministically distinguishing between all given qubits associated with the bit values 0 and 1 with a probability more than $(3/4)^N$.

In Wiesner's original QM (as a quantum token) scheme [38], the bank secretly and securely chooses a random classical string $s(i)$ in $\{0, 1, +, \}^N$ corresponding to the serial number i, and stores $s(i)$ in the bank's database. The bank then generates the quantum state $|\psi_i\rangle$ of N qubits prepared from conjugate quantum bases chosen from the string $s(i)$ (e.g., if the string is ”1-0+” the quantum state $|\psi_i\rangle$ will be: $|1\rangle \otimes |-\rangle \otimes |0\rangle \otimes |+\rangle$). It then gives the output pair $(|\psi_i\rangle, i)$ (i.e., the money state and the serial number) to a bank's client. Here $\{|0\rangle, |1\rangle\}$ and $\{|+\rangle, |-\rangle\}$ are the standard basis and Hadamard basis, respectively. The bank's client presents the token by giving $(|\psi\rangle, i)$ back to the bank, which looks for the secret sequence associated with the serial number i containing the classical description of $|\psi\rangle$. Finally, the bank validates or rejects the token after measuring each of the received qubits in the basis given by the string $s(i)$.

In various extensions to Wiesner's scheme, the bank's client can present the token (i.e., by giving $(|\psi\rangle, i)$) either to the bank or one of a set of vendors (i.e., honest verifiers) based on classical verification approach. Namely, the verifier who applies quantum measurements on $|\psi\rangle$ communicates with the bank via a classical channel for sharing the classical outcomes to validate or reject the QM [45]. Moreover, advanced versions of quantum token schemes rely on computational assumptions [51, 118, 119] in addition to the no-cloning theorem - which can offer the benefit of using QM without communicating with the bank for token validation.

CHAPTER 3

Results and Discussion

In the preceding sections, I presented the principles and fundamental concepts of on-chip configurations for unique functionalities. The various previously described methods were applied to design novel devices employing a combined approach of theoretical analysis, numerical study, and experimental measurements. The main results for each project are presented in this chapter.

3.1 All-Optical Nonlinear Activation Function for Photonic Neural Networks via MXene in Near-Infrared

Though nonlinear AFs were suggested for use in optical NNs, developing ONLU that only relies on light is a tremendous challenge. Furthermore, they were never implemented with MXenes family materials, consisting of a wide range of optical properties for designing photonic devices. The prospect of an all-optical nonlinear transfer function is extremely interesting for key technologies of photonic artificial intelligence chips. Thus, inventing a MXene-based application that can play a vital role in creating a nonlinear unit is exciting.

In this work, I experimentally demonstrated two approaches for implementing the photonic neuron nonlinear AF based on light-matter interaction via 2D material $Ti_3C_2T_x$ in the NIR range in two configurations: deposited film of a layered material (MXene) onto either a transparent substrate or a photonic waveguide. To this end, I tested 2D MXene using $Ti_3C_2T_x$ in distilled water to implement the two proposed configurations and characterize the material's optical properties. Two experimental setups operating in a broad spectral range were employed to study the nonlinear response of the fabricated samples. Next, I confirmed the capability and feasibility of the obtained results in a conventional machine-learning task for classifying the MNIST handwritten digit database. Finally, the performances of two independent NN architectures were validated by focusing on the nonlinear operation functionality formed by the studied photonic devices. Parts of these research outcomes have been published in Ref. [14], where further details of the fabrication processes of MXene-based devices can be found.

3.1.1 Photonic Deep Neural Network Chip Architecture

A fully connected deep-NN consists of at least one hidden layer between the input and output layers. From the photonic implementation perspective, the optical signals carrying intensity-encoded information propagate through an optical circuit, in each layer, by involving optical linear and nonlinear processes. The proposed concept of a fundamental building block for fully integrated deep structured learning, in which I incorporate the MXene-based nonlinear transfer function, is illustrated in Fig. 10. The zoom-in shows the all-optical neuron nonlinear AF established on light-MXene interaction, where a rib waveguide is covered with MXene flakes overlayer. In particular, this chip represents an entire layer in photonic NN architecture. It is composed of optical interference and nonlinearity units, which execute optical matrix multiplication and introduce nonlinear properties in the network. The optical input signals are launched into multiple channels and propagate simultaneously via the waveguides. The OIU is responsible for the linear computing implemented in the mesh of MZIs, each formed of directional couplers and waveguides combined with phase shifters to control the splitting ratio and the differential output phase. This way, the output matrix multiplication can be obtained by completing the linear combination of the inputs arriving from photonic neurons in the preceding building block unit (i.e., a layer). The signals then pass through the ONLU, in which the optical output intensity is given by the application of a nonlinear transfer function.

Finally, the optical output signals serve as the input signals to the next building block unit. In principle, one can optically implement arbitrary deep-NN dimensions and depth considering a cascade of the proposed photonic NN building block. The neurons connect only to different neurons in successive layers by optical waveguide interconnects. When the photonic NN is trained, this architecture can perform its task fully optically on a passive system. Hence the computation of the optical signals will be accomplished without additional energy input at the speed of light in the material. Since an OIU alone is insufficient for a photonic device to act as a building block in NN applications, some optical nonlinearities must be introduced. Therefore, an architectural update is required to integrate the all-optical nonlinear AF with the various current hardware structures that implement the linear operation stated earlier in section 2.3.2. As seen from Eq. (2.17), each neuron applies the nonlinear operation on the summation of all the weighted inputs from neurons in the previous layer. Thus, the MXene-based nonlinear AF is placed between two consecutive layers on each output connection.

In order to enhance the computational energy efficiency and concurrently reduce the processing time of the photonic neuron, several considerations must be taken in realizing the nonlinear unit. First, the all-optical AF configuration should be satisfied by choosing the appropriate materials to express a nonlinear optical response as changes in material's properties for both free-space and integrated photonics platforms. Once the all-optical configuration has been established, proper choice of the physical structure is essential to achieve a nonlinear transfer function that can be operated according to different wavelengths and does not require thermally or electronically controlled.

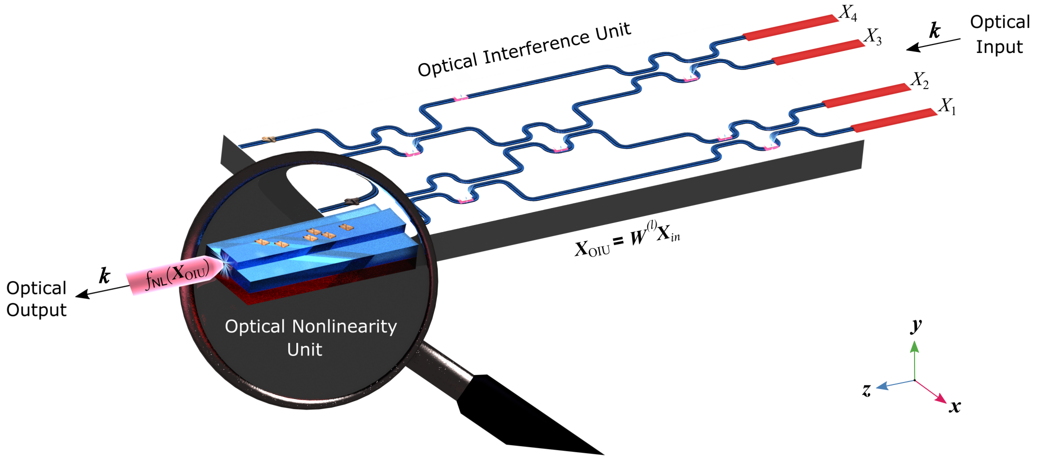

Figure 10 | Photonic NN building block architecture incorporates linear and nonlinear operations. The chip illustrates a general optical implementation of an entire layer via a photonic circuit (grey rectangle) formed by optical waveguide interconnects (marked blue) and elemental optical devices. The wavevector $\boldsymbol{k}$ (black arrows) indicates the propagation direction of the light, where multiple optical input signals $\boldsymbol{X}_{in}$ (marked red) carry encoded information. The linear operation $\boldsymbol{X}_{\text{OIU}} = \boldsymbol{W}^{(l)}\boldsymbol{X}_{in}$ is implemented in the mesh of MZIs integrated with phase shifters (pink glowing objects) and directional couplers (curved sections in the waveguides). The focus is on the ONLU, which realizes an all-optical nonlinear transfer function, $f_{\text{NL}}\left(\boldsymbol{X}_{\text{OIU}}^{(i)}\right)$. This photonic neuron nonlinear AF is based on light-MXene interaction, constructed by a rib waveguide with a MXene flakes overlayer.

3.1.2 Design and Characterization of MXene-Based Configurations

Two devices were planned to exhibit nonlinear optical responses for demonstrating the concept of an all-optical nonlinear AF based on MXene. The studied architectures for both optical free-space and integrated photonics computing approaches are illustrated in Fig. 11. The nonlinearity effects in the optical responses can be observed either by the material's nonlinear optical properties or by the light-matter interaction within an engineered structure. One possibility to implement a nonlinear AF optically is utilizing the nonlinear optical effect of saturable absorber material. Namely, the absorption of the material decreases with an increasing the intensity of the incident light. It can be achieved via illuminating a thin film of MXene on top of a BK-7 substrate by an unpolarized optical EM wave, as shown in Fig. 11a. A further alternative approach is to utilize a hybrid system consisting of a silicon (Si) waveguide with a MXene flakes overlayer, as shown in Fig. 11b, in which an unpolarized optical EM wave illuminates the input facet of a rib waveguide. The interaction with the MXene flakes overlayer occurs through evanescent waves, which leads to some optical losses within the material on the one hand, and causes the scattering of light in all directions on the other hand.

The Si rib waveguide supports multiple modes, where higher-order modes have a longer evanescent field extension into the medium, and concurrently exhibit larger field amplitude at the interface of the waveguide boundary and the medium. Hence, exciting higher-order modes could enhance the evanescent field, which leads to an increase in the coupling between the evanescent waves and the medium. Furthermore, besides the waveguide configuration studied in this work, various waveguide geometry and other structure possibilities exist where such light-MXene interactions can be employed. It can be seen simply from Eq. (2.2) that lower effective index modes are more weakly confined to the waveguide and have more slowly decaying evanescent tails. These improve the sensitivity of the light propagates via the waveguide to the changes in its boundary conditions. In other words, one can control the enhancement of the evanescent field by adjusting the effective index modes (i.e., depending on the waveguide size, shape, and RI of the guiding layer and cladding). For instance, ultra-thin-core single-mode waveguides can be utilized as an alternative approach to increase the coupling between the evanescent waves and MXene as found for absorption overtone spectroscopy [72] or another sensing on a chip application.

MXenes contain a broad family of 2D materials obtained from carbides and nitrides of transition metals such as titanium (Ti) [120]. This work utilizes titanium carbide ($Ti_3C_2T_x$) to implement the two independent configurations. The material is produced by a selective chemical etching process of Ti_3AlC_2 (MAX phase) in a mixture of hydrochloric acid (HCl) and lithium fluoride (LiF), in which the ”A” element (i.e., Al atoms) is selectively removed [121]. Consequently, the surface of the carbide layers becomes terminated by -O, -OH, and -F atoms, which the T_x in the chemical formula represents [122]. The $Ti_3C_2T_x$ crystal structure that forms the suggested MXene-based configurations is shown in Fig. 11c. The proposed devices were manufactured using two fabrication techniques. In the case of thin-film configuration, as shown in Fig. 11a, the MXene was synthesized by our collaborators [123] to deposit a thin film of a layered material ($Ti_3C_2T_x$). Four thin films with different thicknesses of $Ti_3C_2T_x$ in a distilled water solution with a 4.5 mg/ml concentration were spray-coated on BK-7 substrates. In the case of waveguide with MXene flakes overlayer configuration, as shown in Fig. 11b, dry $Ti_3C_2T_x$ rocks were fabricated [124] by our collaborators for future preparation of MXene flakes solution. In addition, the rib waveguide was fabricated based on a silicon-on-insulator (a.k.a. SOI) wafer, as detailed in Ref. [125]. The guiding layer contains a Si nanostrip with a thickness of 400 nm on top of a 2 µm thick Si layer. The substrate is made of silica (SiO_2) to satisfy the guiding condition in Eq. (2.1). Comprehensive details about the MXenes synthesis process and waveguides fabrication done by our collaborators are present in Ref. [14].

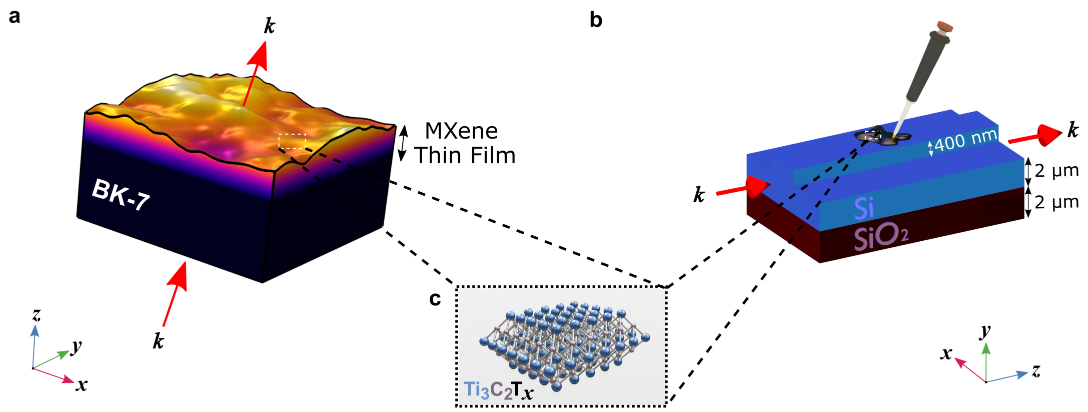

Figure 11 | Geometry and structure of the photonic studied devices based on MXene. a, Schematic illustration of MXene thin film deposited on BK-7 substrate considering a random rough surface. The unpolarized incident light is transmitted through the structure. **b,** Schematic of the MXene overlayer on a waveguide system: unpolarized incident light illuminates the rib waveguide facet covered with MXene flakes. The wavevector $\boldsymbol{k}$ (red arrows) indicates the propagation direction of the light. **c,** $Ti_3C_2T_x$ crystal structure of a 2D material (MXene) deposited onto either a transparent substrate or a photonic waveguide.

For deposited MXene onto the photonic rib waveguide, 5 minutes of sonication of 100 mg dry $Ti_3C_2T_x$ and 10 ml distilled water in an ultrasonic bath was first performed. Consequently, a 10 mg/ml concentration of MXene solution was obtained. Afterward, the solution was ready to be pipetted off to the top surface of the rib waveguide, as shown in Fig. 11b. This step was carried out prior to the experiment. Since their native negative surface charge of the MXene flakes, they form stable colloidal solutions in pure water without additives and surfactants [126]. Accordingly, it is possible to deposit these MXene flakes from distilled water solution (or alternatively, other polar solvents such as alcohols). It is worth mentioning that this property is an essential benefit of MXenes to simplify the implementation of the proposed configuration over other options such as graphene, carbon nanotube (a.k.a. CNT), metal nanoparticles, and related 2D materials.

During this proof of concept demonstration, the MXene deposition was statistically determined by a fixed 10 mg/ml concentration associated with the $Ti_3C_2T_x$ flakes in distilled water along with one droplet pipetted off perpendicularly to the top boundary of the waveguide. Namely, the solution's mass concentration, the utilized polar solvent, and the dripped position can provide a tunning of the MXene flakes deposition. In other words, by controlling the extinction properties of the MXene overlayer on the waveguide, the proposed device could be scaled for large-scale all-optical NN deployment to provide a desired nonlinearity of the optical response.

To further obtain more statistical characteristics of the MXene-based samples and allow physical modeling of the studied devices, the fabricated MXene thin films were characterized by profilometry, spectroscopic ellipsometry, and NIR transmittance to evaluate their thickness, uniformity, and linear optical properties. An EM wave propagating through a lossy medium also experiences attenuation. In such materials, the RI is a complex function $\tilde{n}$, with real part n and imaginary part κ (a.k.a. extinction coefficient). In order to evaluate the linear optical properties of independently fabricated MXene samples with thicknesses ranging from 50 nm to 91 nm, their optical parameters are required. To this end, the spectral dependence of the RI $n(\lambda)$ and extinction coefficient $\kappa(\lambda)$ were obtained via spectroscopic ellipsometry (M2000 XI, J. A. Woollam) measurements from 245 nm to 1690 nm wavelength range.

As can be seen from Fig. 12a-b, the optical parameters are qualitatively similar for all four samples, but still, there are some quantitative differences depending on the film thickness. The wavelength dependence of the medium's optical properties dictates the light's changes during interacting with the material. Thus, the complex dielectric function can fully describe the linear interactions between light and matter. Since most conventional materials are non-magnetic at optical frequencies (i.e., the relative permeability can be taken for granted to be unity, μ_r =1), the complex RI can be related to the complex relative permittivity by:

$$\tilde{\varepsilon}_r(\lambda) = \varepsilon_1(\lambda) + j\varepsilon_2(\lambda) = \tilde{n}^2(\lambda) = (n(\lambda) - j\kappa(\lambda))^2 \ . \tag{3.1}$$

where ε_1 and ε_2 are the real and imaginary components of the relative permittivity, respectively. The relative permittivity of a material is expressed as the ratio of the dielectric function and the vacuum permittivity, given by $\tilde{\varepsilon}_r(\lambda) = \varepsilon(\lambda)/\varepsilon_0$.

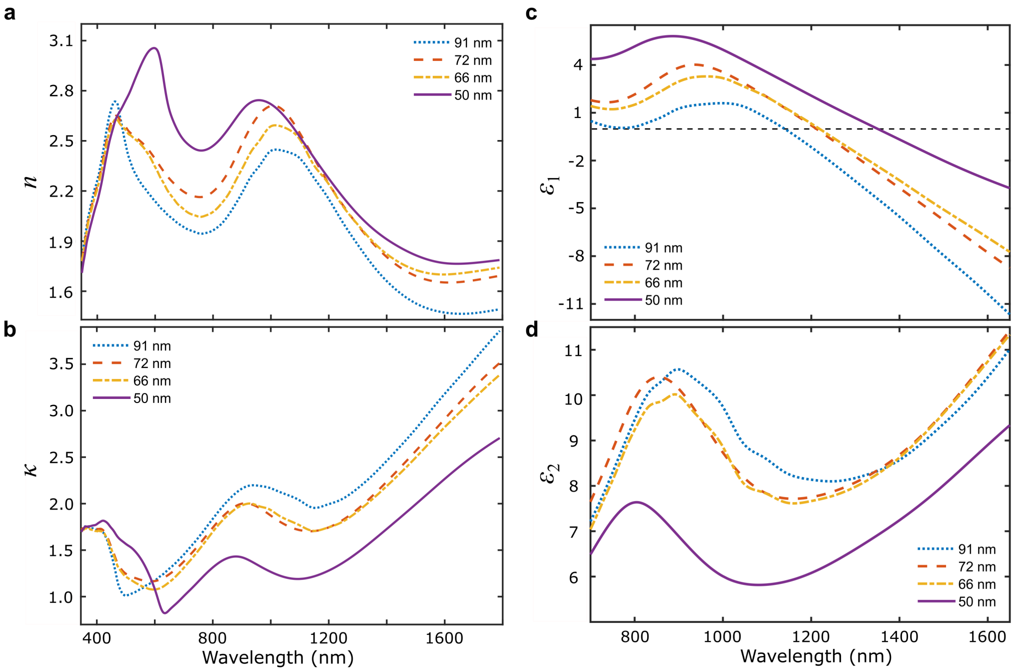

Figure 12 | Dispersion relation of MXene thin films. a-b, The RI n (**a**) and extinction coefficient κ (**b**) of various $Ti_3C_2T_x$ thin films as a function of the wavelength. **c-d,** The spectral dependence of the complex dielectric permittivity $\tilde{\varepsilon}_r(\lambda)$, with real ε_1 (**c**) and imaginary ε_2 (**d**) components of the fabricated thin film of varying thicknesses: 50 nm (solid purple curve), 66 nm (yellow dash-dotted curve), 72 nm (orange dashed curve), and 91 nm (blue dotted curve). The horizontal black dashed line in (**c**) indicates $\varepsilon_1 = 0$.

It is observed from Fig. 12c that a dielectric to metallic crossover occurs at wavelengths larger than 1139 nm. The horizontal black dashed line $\varepsilon_1 = 0$ in Fig. 12c highlights each sample's crossover wavelength (summarized in Table 3.1). It is embodied in the real component ε_1 that becomes negative as the wavelength increases, indicating the onset of free carrier oscillations [127]. Accordingly, $Ti_3C_2T_x$ is a plasmonic material at NIR spectra, where either surface plasmon resonance (SPR) or localized surface plasmon resonance (LSPR) could be excited at the MXene layered material interface. In addition, the crossover of ε_1 from positive to negative values exhibited film thickness dependence, namely, the wavelength in which ε_1 is negative value increases as the thickness of the film decreases (see Table 3.1). In addition, the imaginary component ε_2 for all four samples exhibited a peak at a wavelength longer than 820 nm, as shown in Fig. 12d. The observed ε_2 for the MXene thin films incrementally increased at wavelengths longer than the resonant wavelength. Despite their quantitative differences, the spectral behavior of imaginary components of the dielectric functions is qualitatively similar at all four thicknesses. The changes in the relative permittivity's real and imaginary components for varying MXene thin films could be indicated thickness dependence of the medium's linear optical properties.

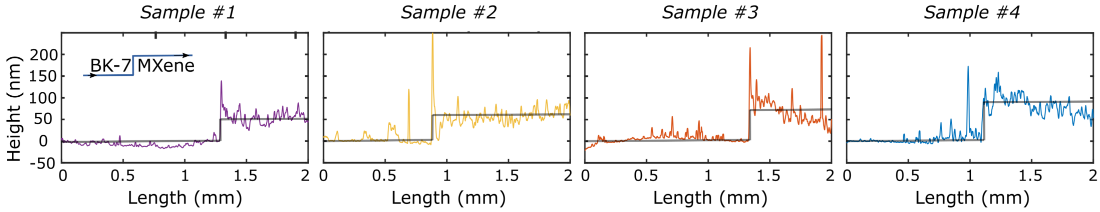

Figure 13 | Surface profile measurements of $Ti_3C_2T_x$ MXene thin films. The average thickness (marked by the solid black line) and surface roughness of each sample were determined using a profilometer. Each sample consists of a spray-coated $Ti_3C_2T_x$ film on a BK-7 substrate with different thicknesses. The inset of the left subplot indicates the profile scanning direction for all sample, in which zero height indicates the substrate plane.

Thicknesses of MXene films were measured using a profilometer (Stylus Veeco Dektak-8), and their surface uniformity was evaluated in terms of roughness, continuous region, and profile flatness. The nanometer-scale topography measurements of the $Ti_3C_2T_x$ thin films are shown in Fig. 13. The step function fitting was deduced from the corresponding line profiles indicating the films' average thicknesses of approximately 50 nm, 66 nm, 72 nm, and 91 nm, where 0 height refers to the surface of the BK-7 substrate (i.e., the probe reference point on the substrate plane). As seen from Table 3.1, which summarizes the characterization parameters of the samples, the surface roughness of the fabricated $Ti_3C_2T_x$ thin films seems to be increased with increasing the film thickness, however, there is a quantitative difference for sample 3. The two thinner samples (1 and 2) exhibit relatively flat surfaces, in contrast to the slop observed from the two thicker samples (3 and 4), which may indicate the existence of broad valleys across the thicker samples (i.e., the differential irregularities' height would be dominant). In addition, all four samples exhibit smoothly and uniformly covered a considerable length (>0.5 mm) substrate with no discontinuous regions. The samples were imaged via camera for fine-tuning and alignment of the profiler's probe to scan the samples' top surface. The profiler's probe moves across the sample to determine the surface irregularities' heights to achieve at least 0.5 mm scanning length in either coated or uncoated regions (total scanning length of 2 mm). When the probe arrived at the boundary position between coated and uncoated regions, the topography profile was characterized by a sharp step height-like function due to the rapid and immediate movement of the prob (the probe movement and the sample were viewed simultaneously via the profiler's camera.). From the perspective of experimental measurements, as shown in the following sections, the random roughness of the spray-coated MXene films does not affect the observed nonlinear optical transform function since the wavelength of the incident light is much larger (>110-fold higher) than the sample's roughness.

Table 3.1 | Characterization parameters of the $Ti_3C_2T_x$ (MXene) thin films.

$Ti_3C_2T_x$ *Sample*	*Thickness (nm)*	*Surface roughness (nm)*	ε_1 *crossover wavelength (nm)*
Sample #1	50	8	1347
Sample #2	66	12	1217
Sample #3	72	10	1210
Sample #4	91	15	1139

Usually, the study of the linear interactions between light and matter involves determining the solutions to Maxwell's equations using constitutive relations along with appropriate boundary conditions. The deposited MXene thin film on the transparent substrate can be analyzed using a typical thin-film structure, as shown in Fig. 14a. The light is incident normally on the MXene interface from the BK-7 substrate, and part of it is transmitted to the air, which are represented as semi-infinite mediums. In practice, when the light is very close to normal incidence, the transmission and reflection coefficients are assumed to be independent of the light's polarization based on the Fresnel equations. The dependency of optical linear transmittance on MXene film thickness can be accomplished with numerical calculations.

The optical response of the MXene thin films was calculated under the excitation of unpolarized light. Each fabricated sample consists of a spray-coated $Ti_3C_2T_x$ film on a BK-7 substrate with varying thicknesses. The computational domains for the model considering Mxene film with a rough surface are depicted in Fig. 14b. The optical wave is launched from the interior port toward the MXene interface. While part of the light is transmitted, other parts are reflected and absorbed by the lossy material. A short segment of the studied structure might be represented when periodic boundary conditions (PBC) are introduced. Since perfectly matched layers (PML) absorb any fields incident upon them, all transmitted light through the MXene sample can be absorbed, avoiding light reflected back and forth.Finally, an additional boundary (purple line in Fig 14b) can be introduced to monitor each sample's transmittance spectra.

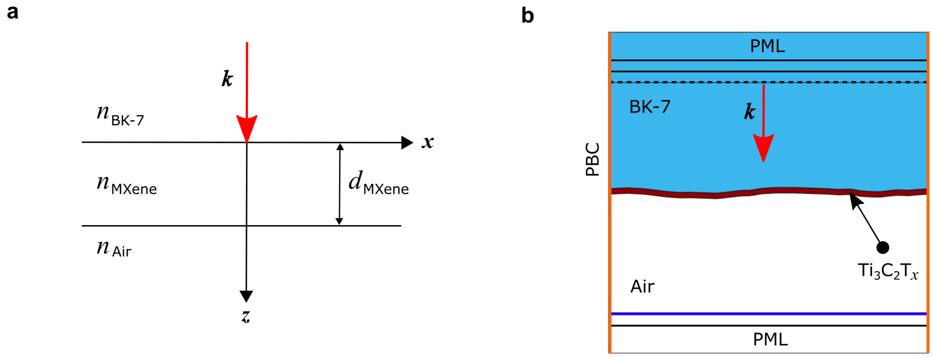

Figure 14 | Schematic diagram and model of MXene films. a, The theoretical model for depositing a film of a layered material (MXene) onto a transparent substrate. **b,** The computational domains of MXene rough film (dark red medium) on BK-7 (light blue medium) and air (white medium) which are used for calculations. Polychromatic light is launched from the interior port toward the MXene interface and absorbed in the perfectly matched layer (PML). Periodic boundary conditions (PBC, orange lines). The wavevector $\boldsymbol{k}$ (red arrows) indicates the propagation direction of the light.

The numerically calculated transmittance spectra for all four samples are shown in Fig. 15a, along with the experimentally obtained output transmittance spectra (see experiment setup detailed in section 3.1.3). The numerical results are in good agreement with the experimental values with a total relative error of 1.27 %. The optical models are qualitatively similar at all four thicknesses, though there are some quantitative differences for the two thicker samples (3 and 4) at shorter wavelengths (<1000 nm). These minor changes can be explained by: 1) The accuracy of the numerical modeling is embodied in the precision of the MXene film optical parameters measured with a spectroscopic ellipsometer, in which a phase delay associated with both the physical thickness and the RI could occur as the film thickness increases. 2) Since a thicker uniform layer is more challenging to obtain using a spray-coated technique, resulting in higher surface roughness, which can have a more dominant effect on the transmitted light at shorter wavelengths λ of the incident light.

It is observed from Fig. 15a that both experimentally measured and numerically calculated optical linear transmittance decreases as the MXene film thickness increases. In their optical spectral transmittance, the $Ti_3C_2T_x$ thin films exhibited a broad peak around $\sim$1100 nm. These can be associated with the well-pronounced dips in the calculated imaginary components ε_2 (Fig. 12d), obtained from measured complex RI $\tilde{n}$ using a spectroscopic ellipsometer. Moreover, at longer wavelengths λ, the material's losses increase as the wavelength values increase (i.e., ε_2 gradually increases) for all four samples, resulting in decreasing transmitted light through the films. This behavior could validate the metallic properties of MXene in this spectral range because the real component ε_1 of MXene thin films is negative at corresponding wavelengths. On the one hand, with decreasing film thickness values, the MXene thin film exhibits lower optical losses, leading to increased light transmission (Fig. 15). On the other hand, ε_1 in thicker films reaches negative values at shorter wavelengths λ (Fig. 12c). These indicate that the linear optical properties of MXene exhibit film thickness dependence.

The dependency of optical linear transmittance on MXene film thickness at a wavelength of 1180 nm is shown in Fig. 15b. While linear optical transmittance of -3.69 dB was observed for a 50 nm thick $Ti_3C_2T_x$ film, it decreased by -5.73 dB when the light was propagating in a 91 nm thick film. The experimental measurements show good correspondence with the numerically calculated results in which the optical linear transmittance of $Ti_3C_2T_x$ films varies with film thickness, exhibiting an exponential-like decrease with an increase in film thickness. Following this behavior, a good estimate to characterize the attenuation of light propagating in the material as related to the linear transmittance may be expressed based approximately on the Beer-Lambert dependence of transmittance on thickness. Namely, an intensity I of light will decrease to $Ie^{-\alpha_0 d}$ as the light travels through a material sample with a thickness of d, giving the relation between the linear transmittance T and absorbance A as $A = \alpha_0 d = -\ln(T)$. The logarithm of the transmittance at 1180 nm versus MXene film thickness is shown in Fig. 15c. A linear fit (solid blue curve) of the measured data expected from the Beer-Lambert law achieved a slope of $1.36 \times 10^{-2}\ \mathrm{nm}^{-1}$, with an intercept of -0.239 and a relative error of 3.81%. While the obtained slope can be associated with the absorption coefficient $\alpha_0 = 1.36 \times 10^5\ \mathrm{cm}^{-1}$, the intercept may be related to the total reflectance of the deposited MXene thin film. The approximated slope compares well with the absorption coefficient of $1.52 \times 10^5\ \mathrm{cm}^{-1}$ calculated from ellipsometry measurement by its connection to the imaginary component of the RI as $\alpha_0(\lambda) = 4\pi\kappa(\lambda)/\lambda$.

Both the numerical simulations and the experimental measurements exhibit the dependency of MXene transmittance on the thickness, as expected from spectroscopic ellipsometry measurements. This can be associated with the changes in both real and imaginary components of the relative permittivity for varying MXene thin films (as shown in Fig 12), which indicates the thickness dependence of the MXene's linear optical properties. Hence, the obtained optical transmittance of the $Ti_3C_2T_x$ MXene films supports their optical parameters and thickness. For comparison, the logarithm of the transmittance at 1180 nm versus MXene film thickness without considering the dispersion relation dependence of MXene film thickness is also depicted in Fig. 15c (black dashed curve). Namely, modeling only changes in the film thickness without taking into account the different obtained complex RI dispersion relations of the various films provided by a spectroscopic ellipsometer. Consequently, there is a quantitative difference in the transmittance for all samples between the numerical and experimental results. In contrast, the calculated results show good correspondence with the experimental computed values in the dispersion relation dependence of MXene films (solid blue curve). Since the transmittance increases as MXene film thickness decreases, a thinner film is more suitable to serve as an optical AF for photonics deep structured learning architectures.

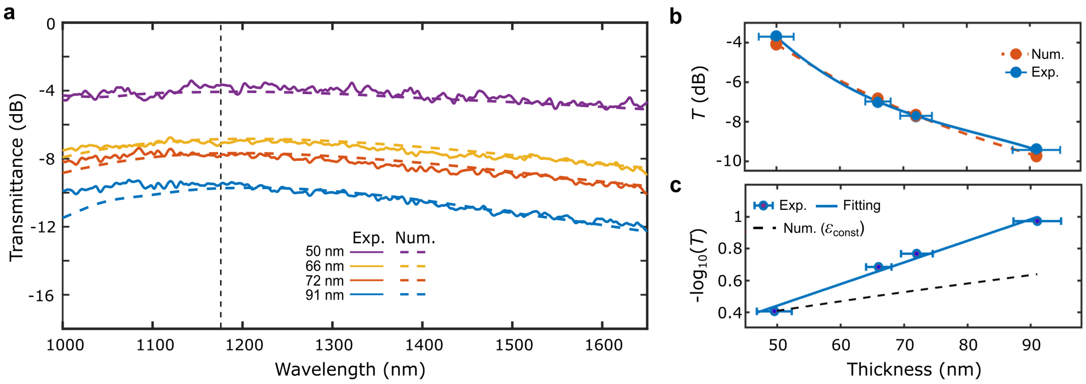

Figure 15 | NIR transmittance spectra of MXene thin films. a, Experimentally obtained and numerically calculated spectral transmittance for $Ti_3C_2T_x$ thin films with various thicknesses (top to bottom) 50 nm, 66 nm, 72 nm, and 91 nm. **b,** Dependence of transmittance on MXene film thickness of the numerical (orange) and experimental (blue) results at a wavelength of 1180 nm. **c,** The logarithm of transmittance vs. film thickness of MXene thin films (blue dots) and linear fit to the data using the derived thickness (solid blue curve). The dashed black curve indicates the numerical $-\log_{10}(T)$ values with thickness-independent permittivity.

Maxwell's equations were solved numerically to understand better the light-matter interaction in the cases of evanescent excitation. The 3D simulations were carried out utilizing the COMSOL Multiphysics platform in the wave optics module based on the finite element analysis method. As shown in Fig. 16a, numerical evidence of the MXeme-light interactions can be achieved via modeling unpolarized optical EM wave that incident upon the input facet of the Si rib waveguide covered with MXene material. The interaction between the optical evanescent waves and MXene flakes overlayer leads to optical losses within the material due to its absorption. It simultaneously leads to scattering light in all directions. While the optical modes travel without disturbance through the waveguide without the presence of the MXene flakes overlayer, the total broadband optical transmittance of the device is defined primarily by the power losses within the interaction length.

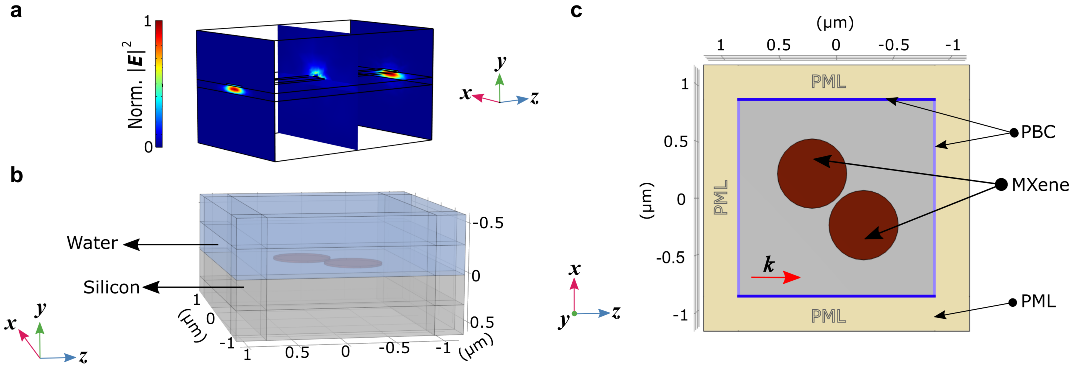

Figure 16 | The modeled geometry of MXene nanodisks on the silicon substrate. a, The electric field distribution of the optical mode propagating in the waveguide at the input and output planes, and the scattered field when interacting with MXene nanodisks (middle plane), considering the light propagating along the z-direction, with evanescent field components in the y-direction extending into the sample medium. **b,** The computational domains of a unit cell considered in the simulation include two MXene nanodisks (red media) embedded in water (light blue medium); placed on top of a silicon surface (grey medium). **c,** Schematic cross-sectional top view of the numerical model with perfectly matched layers (PML, yellow domains) for setting up the model's EM interface to obtain the total field with the MXene nanodisks present. The wavevector $\boldsymbol{k}$ (red arrow) indicates the propagation direction of the light.

To further numerically explore the hybrid system consisting of a MXene overlayer on the top waveguide's surface, a unit cell of the configuration was simulated, which formed two MXene flakes atop a Si surface illuminated by the evanescent waves of the studied rib waveguide. The 3D computational domains of the MXene-based system, as shown in Fig. 16b, is composed of two MXene nanodisks embedded in distilled water on top of a Si surface. The dimensions of the $Ti_3C_2T_x$ nanodisks were evaluated from scanning electron microscopy (SEM) images of the fabricated MXene flakes atop the rib waveguide, obtained by our collaborators [14]. The MXene nanodisks thickness was fixed to 10 nm with a radius of 0.25 µm, and separated by 15 nm. The material's complex dielectric function can entirely define the material optical properties in the simulations. While the empirical dispersion relations of Si [128] and SiO_2 [129] were taken from the available RI database, the complex dielectric function of MXene was estimated by the measured RI distribution via the spectroscopic ellipsometer (as shown in Fig. 12). Since the MXene nanodisks' thickness is smaller than the thinnest sample in the dispersion measurements, the device was calibrated by measuring known transmittance spectra for the lowest input power and comparing it to the calculated spectral extinction properties. To this end, modifications were implemented to distributions of n and κ of the complex RI for the MXene nanodisks. As can be seen from Fig. 12, the optical parameters are qualitatively similar for all four samples, but still, there are some quantitative differences depending on the film thickness. Therefore, fine-tuning multiplication factors of both real and imaginary parts of the thinnest MXene sample was performed. Namely, in this case, the obtained optimal factors are $\tilde{n}_{\text{optimal}} = 1.06 \cdot n - 0.9 \cdot j\kappa$.

The top cross-sectional view of the numerical unit cell model is shown in Fig. 16c. As detailed below, the simulation first computes a background field and then uses that to arrive at the total field with the MXene nanodisks present by using two EM interfaces in which the PBCs and PMLs are used separately. The incident wave is first entered as a background electric field, where the optical field propagates along the waveguide core (z-direction), with evanescent field components in the y-direction without the presence of MXene nanodisks. The full-field solution can be achieved with a first EM model interface that surrounds the geometry with periodic boundaries. The PBCs on parallel geometry boundaries were meshed identically to ensure the accuracy of the calculated results [130]. Then, the perturbation to the total optical field caused by the localized MXene nanodisks can be calculated considering the optical background field. To this end, an additional EM model interface introduced the MXene nanodisks (red circles) and covered the geometry with PMLs (yellow domains in Fig. 16c) [130]. The PMLs were used only to absorb the scattered field, utilizing a swept mesh with eight elements across each PML domain to ensure the accuracy of the calculated results.

The extinction properties of the MXene overlayer on the waveguide include both absorption and light scattering contributions. While the scattering cross-section σ_{sc} can be calculated by integrating the scattered intensity over the MXene nanodisks' closed surface, the absorption cross-section σ_{abs} can be calculated by volumetric integration of the power loss density over their volume. The extinction cross-section σ_{Ext} is the sum of the absorption and scattering cross-sections and is defined as:

$$\sigma_{\text{Ext}} = \sigma_{\text{sc}} + \sigma_{\text{abs}} = \frac{1}{I_0} \iint \left(\mathbf{n} \cdot \mathbf{S}_{\text{sc}}\right) dS + \frac{1}{I_0} \iiint P_{\text{loss}} dV \tag{3.2}$$

where I_0 is the incident intensity, $\mathbf{n}$ is the normal vector pointing outward from the nanodisks, $\mathbf{S}$ is the scattered Poynting vector, and P_{loss} is the power loss density in the MXene nanodisks. The amount of the total optical field's power loss can be defined as: $P_{\text{loss}} = \frac{1}{2}\omega \operatorname{Im}(\varepsilon)|E|^2$, where ω is the angular frequency of the light.

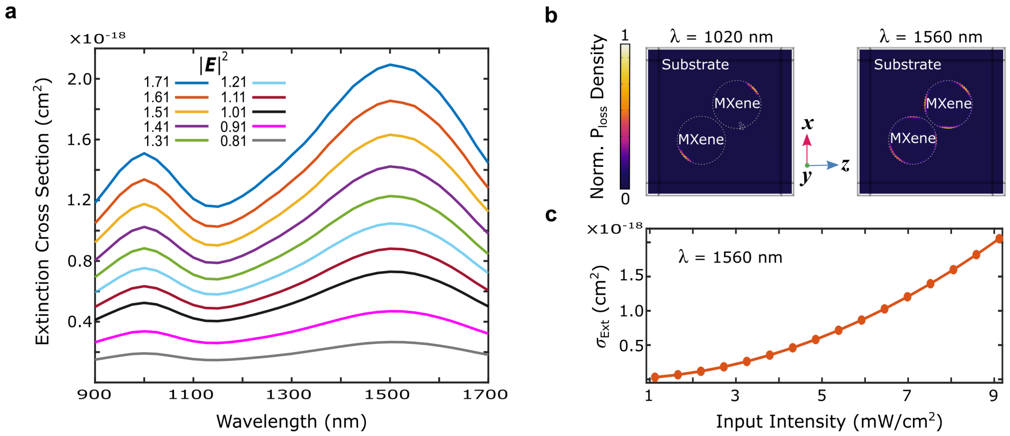

Figure 17 | Numerical results of MXene nanodisks on a substrate. a, Calculated results of extinction cross-section spectra for MXene nanodisks atop a silicon waveguide for several electric field intensities. **b,** Normalized power loss density P_{loss} in a horizontal slice through the MXene nanodisks (the silicon-water interface) of diameter 500 nm with 10 nm height at lower (1020 nm) and longer (1560 nm) wavelengths resonances. **c,** Dependence of the extinction cross-section σ_{Ext} on the incident electric field intensity at a wavelength of 1560 nm.

The numerically calculated extinction cross-section of the MXene nanodisks on the Si substrate while experiencing different optical field intensities ($I = 2\varepsilon_0 c|E|^2$) are shown in Fig. 17a. The obtained spectral profiles exhibit a well-pronounced spectral signature with two peaks around 1020 nm and a broader one around 1560 nm. These peaks can be associated with optical losses of the optical field due to plasmonic excitation of the MXene nanodisks on the Si surface. Both transversal and longitudinal surface plasmons have been evidenced in these wavelength ranges for MXene nanodisks with the same dimensions [131]. Where the free carrier oscillations in MXene thin film are more practicable at longer wavelengths (as evidenced from dielectric to metallic crossover, Fig. 12c). The power loss density associated with the MXene nanodisks at the Si-water interface for the resonance wavelengths 1020 nm and 1560 nm is depicted in Fig. 17b. Most of the optical losses occur near the outer edges of the MXene flakes' surface, and additional optical losses can be observed near the surface between the MXene particles at a wavelength of 1560 nm. The extinction cross-section at a wavelength of 1560 nm was derived from the calculated spectral results to assess the applied optical field intensity dependence in the proposed hybrid system response, as shown in Fig. 17c for varying optical field intensities from 1.1 mW/cm^2 to 9.2 mW/cm^2. Through its optical mechanism of operation, an enhancement of the extinction properties of the photonic structure is obtained as the incident optical field intensity increases. The optical power of the incoming EM radiation associated with the photon flux quadratically depends on the applied optical electric field. Therefore, a covered Si waveguide with MXene flakes overlayer may open the opportunity to implement a passive all-optical AF based on decreasing the transmission of light through the waveguide as the input intensity increases due to increasing the optical losses on its top boundary.

3.1.3 Experimental Demonstration of the Photonic Nonlinear Activation Functions

The MXene-based configurations were fabricated following the two designs previously discussed (Fig. 11), and the nonlinearity in their optical response when experiencing different optical intensities was measured by employing two independent experimental setups operating in a broad spectral range. The optical systems were constructed in a cleanroom environment at the '*Light-on-a-Chip*' group, providing a controlled environment that minimizes the amount of background light to which the samples are exposed. A supercontinuum white light laser (SuperK EXTREME EXW12, NKT Photonics) was used as the optical source in both experimental setups, allowing simultaneous wavelength and intensity interrogation. This light source provides a broad spectral bandwidth from 460 nm to 2400 nm with a total output power of 4.5 W, in which the laser output emission level can be adjusted. The collimated and coherent beam emitted from the laser was focused onto a SM fiber facet (P11550AFC, Thorlabs) using an achromat MO (RMS10X, Olympus) to achieve more flexibility when adjusting the incident light onto the samples. With the photonic devices experiencing varying laser intensities, the corresponding spectral transmittance was recorded using an OSA (AQ6370D, Yokogawa).

The differential transmittance was obtained for an accurate and full representation of the MXene-light interactions that contribute to the studied architecture's internal transmittance. For the spectral transmittance of both configurations, the power of the transmitted optical field when the MXene is present on either a BK-7 substrate or an optical rib waveguide was first measured. As reference measurements, the transmitted light without the MXene presence was collected. In particular, the differential transmittance is given by:

$$\mathcal{T}(\lambda, I) = \frac{|T_{\text{MXene}}(\lambda, I)|^2}{|T_{\text{BG}}(\lambda, I)|^2} \tag{3.3}$$

where $|T_{\text{MXene}}|^2$ is the spectral transmittance in two cases: 1) when unpolarized light is coupled to a rib waveguide with $Ti_3C_2T_x$ MXene flakes overlayer, or 2) when unpolarized light illuminates the glass supported $Ti_3C_2T_x$ MXene thin film. On the other hand, $|T_{BG}|^2$ is the transmittance spectra collected from either a blank reference waveguide or a transparent reference substrate. For each case, several measurements were performed when gradually adjusting the applied optical field intensity I.

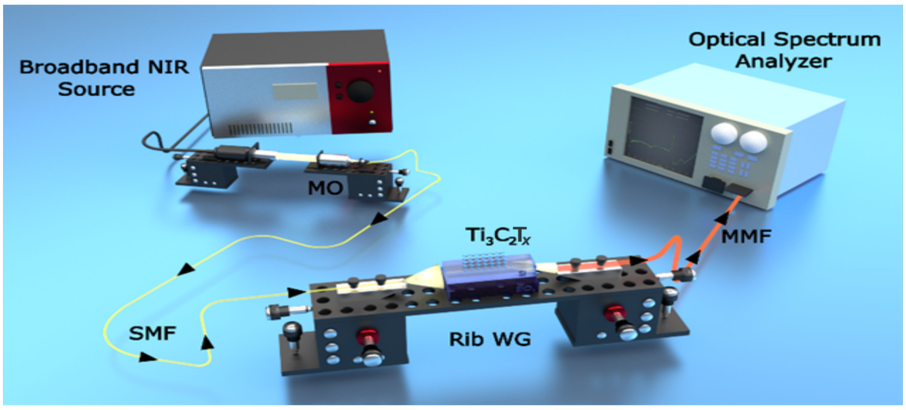

Figure 18 | Rendered illustration of the experimental setup for silicon waveguide with MXene flakes overlayer configuration. Polychromatic and unpolarized light from a single-mode fiber (SMF) is coupled to the rib waveguide (WG), whereas $Ti_3C_2T_x$ flakes solution is placed on the Si waveguide. The output facet of the waveguide is butt-coupled to multimode fiber (MMF), and the transmitted light is measured using a spectrum analyzer. The black arrows indicate the propagation direction of the light.

The MXene layered material was incorporated into an integrated photonic device. In order to test the photonic waveguide with MXene flakes overlayer configuration, an inline measurement optical system was used, providing broad spectral coverage. The rendered illustration of the inline experimental setup for the deposited MXene onto the photonic rib waveguide is shown in Fig. 18. Incident unpolarized light (400-2400 nm) from the SM fiber hits the input facet of the waveguide. The direct butt-coupling method was used to couple the polychromatic light from a SM fiber into the Si waveguide and then from the optical waveguide into a MM fiber. A 4-axis stage with a waveguide mount was placed between two 3-axis piezoelectric stages with a fiber holder to optimize the coupling efficiency in the alignment of the input and output fibers. In particular, this type of waveguide positioning allows flexibility for precisely adjusting the core axes of the photonic waveguide and both input and output fibers. The waveguide and fibers were imaged in the top view for accurate inspection and characterization via a camera (Axiocam, ZEISS) whose axis pointed perpendicularly using a stereo microscope (Stemi SV 6, ZEISS). The photonic waveguide was covered with MXene flakes solution prepared prior to the experiment, as previously stated in section 3.1.2. One drop of 2 μl $Ti_3C_2T_x$ solution was pipetted off perpendicularly to the top surface of the rib waveguide. The optical output field was collected via a MM fiber and the spectral transmittance was recorded using an OSA for different incident optical intensities.

The experimentally obtained output transmittance spectra via direct butt coupling of MM fiber and a rib waveguide covered with MXene flakes overlayer while experiencing different input optical powers are shown in Fig. 19a. While the measurement values related to the lowest input power (for 6% signal) are shown in Fig. 19b, the optical responses are plotted with a step of -15dB between each other for better spectral analysis. Well-pronounced spectral signatures are obtained in the transmittance spectra: a relative minor dip around 980 (FWHM $\sim$70 nm) with a depth of -11 dB, a dip around 1180 nm (FWHM $\sim$130 nm) with a depth of -25 dB followed by a broad shoulder (FWHM $\sim$200 nm), and a dip around 1490 nm (FWHM $\sim$220 nm) with a depth of -20 dB. These dips can be associated with the optical losses of the EM wave passes through the waveguide due to plasmonic excitation of the MXene flakes on the Si surface. In addition, the nanoscale flakes of MXene can exhibit a nano-antenna effect resulting in resonances appearing in transmittance spectra. Moreover, plasmonic excitations effect in MXene flakes can be arises from a plasmon-induced increase in the ground state absorption at photon energies above the threshold for free carrier oscillations [33].

The dip in transmittance spectra around 1490 nm can be associated with the first overtone excitation of -OH functional group out-of-plane vibrations of MXene [132]. The first principle calculation [133] verifies the fundamental vibration related to this overtone. The dip in the transmittance spectra around 980 nm can be explained by the MXene dispersion as measured with the spectroscopic ellipsometer. In particular, the peak in the imaginary component ε_2 (shown in Fig. 12d) can be related to high optical losses of MXene flakes covering the waveguide surface resulting in the dip appearing in the transmittance spectra. These two dips correspond to the observed two peaks in the simulated absorption cross-section (the dashed purple curve in Fig. 19a) of MXene nanodisks of diameter 500 nm with 10 nm height (detailed in the preceding section). The interaction of the light with MXene is not direct illumination, but it occurs when the optical EM wave propagates through the Si waveguide resulting in the absorption peaks behavior and corresponding resonances appearing in transmittance spectra. The dip in the transmittance spectra around 1180 nm can be associated with the waveguide shifted overtone vibration of MXene flakes overlayer assigned to the OH/H_2O native oxide layer on the waveguide surface or with plasmonic excitation because the real part of the permittivity of MXene becomes negative in this wavelength range, satisfying the condition $\varepsilon_1 < 0$ for the measured dispersion spectra $\varepsilon(\lambda)$ (shown in Fig. 12a). In addition, plasmonic excitations have been evidenced in MXene nanodisks in the NIR spectral region with a similar aspect ratio (as shown in Ref. [131]), exhibiting a broad plasmon resonance peak around 1200 nm.

The total transmittance is defined fundamentally by the power losses within the interaction length of the MXene-waveguide hybrid system. Following this behavior, a good estimate to characterize the transmittance of light propagating through the Si waveguide covered with MXene flakes overlayer may be expressed as a function of the wavelength based on the composite plasmonic waveguide as obtained in Ref. [134] and has the representation of the form:

$$T(\lambda) = \left| \sum_{\gamma 1 = m} C_{\gamma 1} \cdot e^{-j\alpha_{\gamma 1} L} \right|^2 \tag{3.4}$$

where $C_{\gamma 1} = \left(I_{\gamma 0,\gamma 1} + I_{\gamma_1,\gamma_0}\right)^2 / \left(4 I_{\gamma 0,\gamma 0} I_{\gamma 1,\gamma 1}\right)$, L is the interaction length, $\alpha_{\gamma 1}$ is an attenuation coefficient of mode m in a region covered with MXene flakes, $\gamma 0$ are the guided modes in blank dielectric waveguide, and $\gamma 1$ are the guided modes influenced by the MXene flakes overlayer. The experimentally obtained transmittance as a function of the wavelength for the lowest input power (6%) is shown in Fig. 19b, together with the corresponding fitting curve according to Eq. (3.4). Considering the first eight modes supported by the waveguide $m = 0, 1, \ldots, 8$, the transmittance fitting was calculated in the wavelength range from 1260 nm to 1600 nm. The experimental results show good correspondence with the theoretically computed values with a total relative error of 2.34%.

The normalized measured transmittance (for all the signals, relative to the maximal obtained measured value) as a function of both wavelength and input power is shown in Fig. 19c, highlighting the studied system's possible optical transfer functions. The Si waveguide covered with MXene flakes overlayer configuration exhibit a broad spectral optical response to the incident light power appearing in a wavelength region in telecom bands which are commonly used in optical communication devices. Each spectral window is highlighted in transparent boxes: original (O-band), extended (E-band), short wavelengths (S-band), conventional (C-band), and long wavelengths (L-band). For the MXene-waveguide configuration, quadratic fitting was used due to the nonlinear operation acting on the optical intensity, which is directly related to the electric field amplitude with squaring proportionality. In other words, the incident optical field intensity associated with the photon flux is quadratically dependent on the applied optical electric field (i.e., $I = 2\varepsilon_0 c|E|^2$). The experimentally measured nonlinear transmittance responses and the corresponding calculated fitted curves at various operating wavelengths are shown in Fig. 19d for the O-band (1310 nm, orange curve), E-band (1360 nm red curve), and C-band (1550 nm, purple).

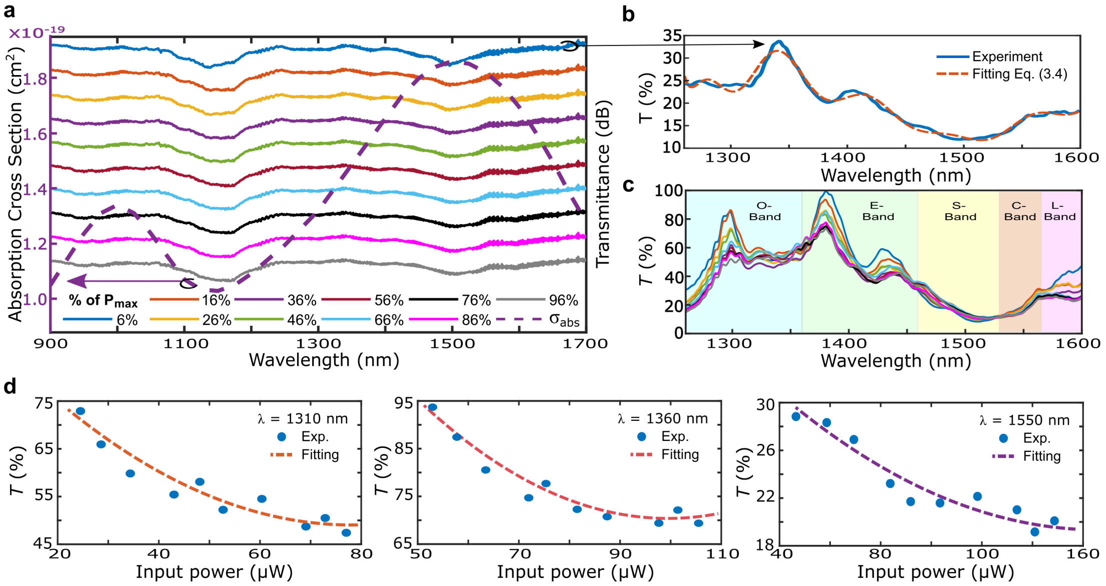

Figure 19 | Experimental results of a silicon waveguide with MXene flakes overlayer. a, The measured transmittance spectra from silicon rib waveguide covered with MXene flakes for different input power varying from 6% to 96% (from top to bottom). The measurement values related to the lowest input power are shown in subplot (**b**), and the others are plotted with a step of -15dB. The simulated absorption cross-section spectra $\sigma_{\text{abs}}(\lambda)$ of the MXene nanodisks atop a silicon waveguide is indicated by the purple dashed curve. **b,** The experimentally obtained transmittance (blue curve) as a function of the wavelength for the lowest input power (6%) and the corresponding fitting according to Eq. (3.4) (dashed orange curve). **c,** Zoom-in of the normalized measured transmittance (relative to the maximum obtained measured value) dependence on the wavelength showing a broad optical response to the incident light power that appears in wavelength regions corresponding to the telecom bands (each spectral window highlighted in a transparent box). The curves' color corresponding to the same signals appears in subplot (**a**) legend. **d,** Experimentally measured nonlinear transmittance responses and the corresponding calculated fitted curves at various operating wavelengths in the 'O' (left subplot, orange), 'E' (middle subplot, red), and 'C' (right subplot, purple) bands.

Going forward, the rendered schematic illustration of the free-space illumination experimental setup for the deposited MXene thin film onto a transparent substrate is shown in Fig. 20. A multiple-wavelength optical system was used with light frequencies covering the NIR spectrum (400-2400 nm) emitted in a single spatially coherent beam with a repetition rate of 78.56 MHz from a pulsed supercontinuum laser. The polychromatic light emitted by the SM fiber was collimated via a reflective collimator (RC04FC-P01, Thorlabs) followed by an iris. The laser output emission level was controlled in order to form an optical field of gradually varying laser intensity. The BK-7 glass supported $Ti_3C_2T_x$ film of a 50 nm thickness, as depicted in the inset of Fig. 20, was mounted on a fixed stage and an unpolarized beam was incident upon the glass with an approximately 100 µm spot. During all the measurements, the experimental setup was preserved at normal incidence (i.e., the ray path is perpendicular to the sample interface). The transmitted light was collected directly to the OSA via MMF (50:125 µm core to cladding size ratio) using an achromat MO (RMS4X, Olympus).

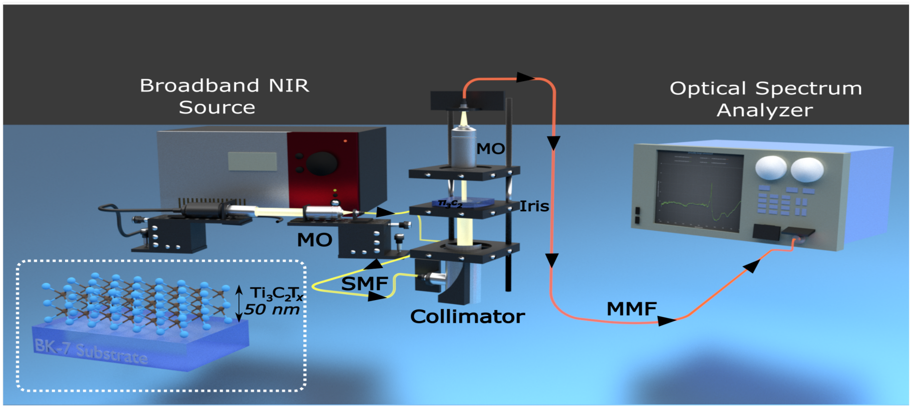

Figure 20 | Rendered illustration of free-space illumination experimental setup for MXene thin film configuration. Polychromatic and unpolarized light from a single-mode fiber (SMF) is collimated and incident normally on the glass substrate. The inset shows the $Ti_3C_2T_x$ thin film with a thickness of 50 nm supported by a BK-7 glass. The transmitted light is collected with a focusing microscope objective (MO) into multimode fiber (MMF) and measured using a spectrum analyzer. The black arrows indicate the propagation direction of the light.

The experimentally obtained output transmittance spectra through the MXene thin film while experiencing different input powers are shown in Fig. 21a. The transmittance of $Ti_3C_2T_x$ film exhibit a well-pronounced spectral signature, which increases as wavelength increases until it reaches a maximum around 1150 nm, where the transmittance then decreases. The observed dip in the transmission around 800 nm show good correspondence with the peak in the calculated imaginary component ε_2 (the dashed curve in Fig. 21a) obtained from measured complex RI with a spectroscopic ellipsometer (Fig. 12). In addition, the broad spectral peak around 1150 nm (FWHM ~400 nm) can be associated with a low attenuation corresponding to the observed minimum in the imaginary component ε_2. At longer wavelengths, the losses of the material increase as the wavelength increase, resulting in a decrease in the obtained transmission spectra, which can be associated with the dielectric to metallic crossover that occurs at wavelengths λ

greater than 1347 nm (ε_1 becomes negative, Fig. 12c). As expected, metal at optical frequencies exhibits higher losses, leading to more absorbed photons at increasing values of λ.

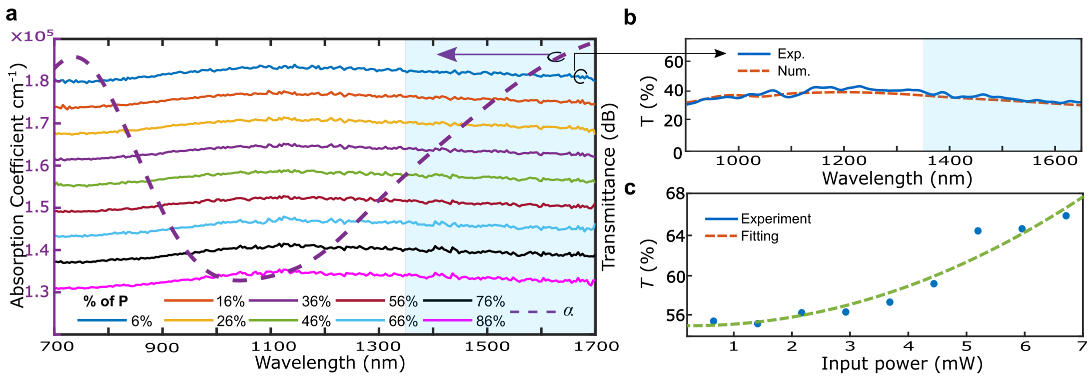

Figure 21 | Experimental results of MXene thin film optical transfer function. a, The measured transmittance spectra for 50 nm thickness MXene thin film deposited on BK-7 substrate for different input power varying from 6% to 86% (from top to bottom). The measurement values related to the lowest input power are shown in subplot (**b**), and the others are plotted with a step of -3dB. The purple dashed curve indicates the absorption coefficient for MXene thin film calculated from the spectroscopic ellipsometry measurement by its connection to the imaginary component of the RI as $\alpha(\lambda) = 4\pi\kappa(\lambda)/\lambda$. The blue area indicates the spectral region in which ε_1 becomes negative. **b,** The numerically calculated (dashed orange curve) and experimentally obtained (blue curve) transmittance response as a function of the wavelength for the lowest input power (6%). **c,** The measured nonlinear transmittance at a wavelength of 1236 nm as a function of incident power for $Ti_3C_2T_x$ 50 nm film and the corresponding calculated fitted curve.

Despite increases in the local electric field by plasmonic excitation in noble metal nanoparticles leading to saturation absorption enhancement, the simultaneous increase in free carrier oscillations typically prevents the saturable absorption behavior. By contrast, the saturable absorption behavior in MXene thin film can be associated with increased ground state absorption due to plasmon excitation [33]. On the one hand, surface plasmons have been evidenced in MXene thin film at the nanometer scale in the NIR spectral region, exhibiting a broad surface plasmon peak around 1210 nm (as stated in Ref. [135]). On the other hand, the free carrier oscillations in MXene thin film are more practicable at longer wavelengths >1347 nm (as evidenced from dielectric to metallic crossover, Fig. 12c). Consequently, these mechanisms cause the depletion of the ground state population to be more dominant at shorter wavelengths λ of the optical wave below the threshold for free carrier oscillations. These can lead to increased transmittance as the power of the applied optical field increases (i.e., nonlinear transmittance), which refers to saturable absorption behavior. Thus, passive intensity modulation of the incident light can be possible by using such mechanisms in which the nonlinear transmittance is embodied in the saturable absorption effects of MXene thin film with a 50 nm thickness.

As seen from Eq. (2.15), the absorption of saturable absorber material is attributed to a nonlinear relationship with the incident optical field intensity. In particular, the transmission through the MXene thin film at a given wavelength of excitation λ increases as increasing values of input light intensity. Utilizing the saturable absorption property of MXene, the nonlinear transfer function can be expressed by:

$$T(I) = 1 - \Delta T e^{-I/I_{\mathrm{s}}} - T_{\mathrm{ns}} \; . \tag{3.5}$$

where $T(I)$ is the transmittance, ΔT is the modulation depth, I and I_{s} are the incident and saturation intensities, and T_{ns} is attributed to non-saturable absorbance (i.e., the saturable absorber does not saturate totally to zero resulting in non-saturable losses).

The corresponding optical transmittance was recorded by gradually adjusting the incident optical power. The input power dependence of transmittance at a wavelength of 1236 nm is shown in Fig. 21c, along with the fitted curve. In particular, the power dependency of transmittance shows exponential growth: it increases slowly at low input powers, then increases sharply at higher input powers until the saturated power density, finally gradually increases until it reaches a maximum level and becomes nearly constant (i.e., indicates the non-saturable absorption).

3.1.4 All-Optical Deep Neural Networks Emulation

Having obtained several different nonlinear optical responses represent the optical transfer functions of the MXene-based configurations as a function of the power of the input optical signal, these optical responses were introduced as nonlinear AFs of nonlinear activators. To study the effectiveness and functionality of the obtained nonlinear activators in deep structured learning configurations, their performance was characterized by two independent NN architectures on a conventional classification machine-learning task. These proposed configurations can serve as nonlinear units in which the nonlinear transfer function can be flexibly designed depending on the operating wavelength without modifying the physical structure. They operate at commonly used optical communication wavelength bands and can be adjusted by controlling a variable broadband light source via standard software.

The nonlinear transmittance curves form the nonlinear AFs of nonlinear activators for MXene thin film deposited on a BK-7 substrate at a wavelength of 1230 nm, and for MXene deposited onto a photonic rib waveguide at a wavelength of 1310 nm, 1360 nm, and 1550 nm are shown in Fig. 22a-d. Each set for each nonlinear AF mechanism consists of several measurements of normalized transmittance for various input optical powers. Both input and output values were normalized relative to the maximal measured value for each data set. In general, the nonlinear activators squash a real input number to a fixed interval specified with unitless, as shown in Fig. 7 for several typically used software-based nonlinear AFs employed to compare to the proposed all-optical configurations. In practice, realistic optical AFs input and output units are in the context of spectral quantities specified with units of mW/nm (or dBm/nm) and need to be normalized. As seen in Eq. (2.17), a generic nonlinear activator f_{NL} is defined via a mathematical function that theoretically models the system's output for each possible input for each neuron. In practice, this is equivalent to operating devices' optical transform function. Namely, this can be expressed by the physical mapping $n_{out} = f_{NL}\left(X_{OIU}\right) \longrightarrow P_{out} = f_{NL}(P_{in}) = T(P_{in}) \times P_{in}$. Therefore, to achieve a mathematical model of the nonlinear activators for possible use in photonic NN emulation, a f_{NL} that models the optical transfer functions associated with each studied mechanism due to MXene-light interaction (as detailed in the preceding section) need to be considered as shown in Fig. 22.

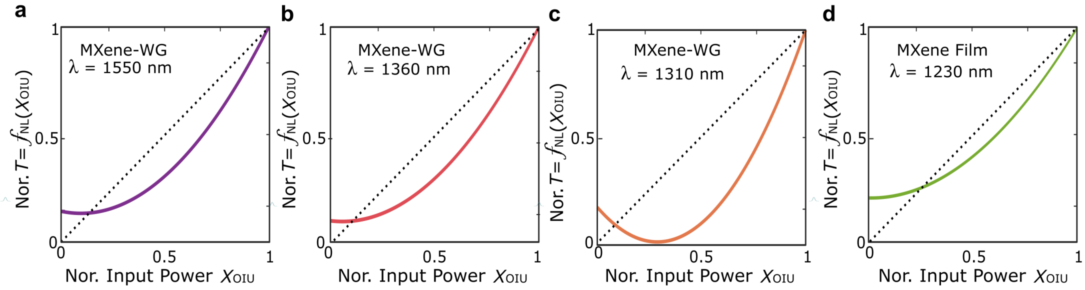

Figure 22 | Experimentally results of MXene-based all-optical nonlinear activators. a-d, Different nonlinear AFs embodied in the optical transfer functions of the silicon waveguide covered with MXene flakes overlayer (**a-c**) and MXene thin film (**d**) architectures operate at various wavelengths in the typical telecom bands. The normalized nonlinear transmittance (relative to the maximum obtained measured value for each data set) shows the obtained AFs of nonlinear activators in the NNs.

Although no negative inputs (or weights) were involved in the deep-learning task (corresponding to a standard intensity encoding scheme), the proposed MXene-based AFs can efficiently work in such deep structured learning configurations. This because the difference between input signals with $P_{in} < 0$ and $P_{in} > 0$ is only reflected by their phases, that is $-P_{in} = e^{-j\pi}P_{in}$. Therefore, $P_{out}(P_{in})$ is an odd function $P_{out}(-P_{in}) = -P_{out}(P_{in})$. In addition, the devices have intensity dependency, and changes in the optical signal phase do not affect the applied optical modulation. However, since the photodetectors and the proposed all-optical configuration are not sensitive to the optical signal phase, $P_{out}(P_{in})$ need to be considered as an even function, that is $P_{out}(-P_{in}) = P_{out}(P_{in})$. Accordingly, only the regime where $P_{in} > 0$ was plotted, as shown in Fig. 22. It is worth mentioning that the wavelength dependence of the optical responses allows tuning the nonlinear AF shape of the nonlinear activator. Note that the studied experimental nonlinear AFs represent a subset of transfer functions achievable by the proposed all-optical devices without modifying their structure or involving complex geometry.

A deep learning simulator was used to characterize the performance of the photonic AFs in a machine learning task of classifying images. Two deep structured learning architectures were implemented, FFNN and CNN, using a deep learning framework [136] in the Matlab environment. For consistency, both NN architectures performed the same task: identifying the represented number for each input handwritten digit image from the MNIST (Modified National Institute of Standards and Technology) dataset consisting of 60,000 images of handwritten digits ranging from 0 to 9. In order to form independent sets for training and validation phases, a random sampling was employed to split the MNIST dataset into training and validation subsets in an 80%-20% ratio (i.e., 48,000 and 12,000 images), respectively. This ensures that the models can classify the images based on learning about the data features without acknowledging the data beforehand. On the one hand, during the training phase, the weights are optimized using the backpropagation algorithm [137], which aims to learn the dataset features for future prediction. On the other hand, the validation dataset is used to verify the trained network's performance without updating the weights. In particular, the deep structured learning models were trained by feeding the dataset into the input layer followed by computing the outputs (so-called forward propagation). Then the models optimize the weights (so-called backpropagation) based on the loss function calculated from outputs prediction. The deep learning networks were trained using a stochastic gradient descent optimizer with a learning rate of 0.001 for 50 epochs. Both network architectures were trained with two sets of AFs: 1) software-based AFs commonly used in deep structured learning applications, and 2) the studied MXene-based all-optical nonlinear AFs based on their transfer functions.

The decomposition of the studied three-layer photonic FFNN is shown in Fig. 23a, along with an example of outputs predicted labels corresponding to four handwritten digit images fed to the input layer. The photonic NN consists of a sequence of linear and nonlinear operations corresponding to OIU and ONLU, respectively, which implements optical matrix multiplication by integrated MZIs meshes and applies nonlinear activation through MXene-based configurations (as the building block represented in Fig. 10). The nonlinear AF is placed on each output connection between two consecutive layers, where the detectable optical signals pass through a softmax function at the end. While each hidden layer of the FFNN comprises 100 neurons, the output layer in the network consists of ten neurons corresponding to 10 classes of output, each representing a digit ranging from 0 to 9. The input layer consists of 784 neurons (does not perform any weighting or apply an AF to the input signals) due to the input data's total size. The input layer consists of 784 neurons (does not perform any weighting or apply an AF to the input signals) due to the input data's total size. Namely, the input layer dimension must accommodate all the $28^2 = 784$ real-space pixels as inputs. In other words, feeding each image to the photonic NN requires preprocessing from a 2D matrix to a high-dimensional vector. In practice, these can be achieved using a traditional computer due to a computationally inexpensive algorithm or completely passive via Fourier optics [138]. Moreover, using Fourier optics can reduce the total size of the input data to only 16 complex Fourier coefficients [102] resulting in a decrease in the required photonic NN dimension.

The classification accuracy and loss of the photonic FFNN during the training phase for 50 epochs are shown in Fig. 23b. The results show the performance of trained photonic FFNN, employing either all-optical MXene-based AFs or software-based nonlinear AFs on the MNIST dataset. All the studied photonic AFs based on Si waveguide covered with MXene flakes overlayer and MXene thin-film achieve accuracy between 97.9 % to 99.1 %. The network prediction accuracy and loss of the validation dataset as a function of epoch count are shown in Fig. 23c to validate the models' performance. All models exhibit convergence behavior in which the classification accuracy increases rapidly at first as the epoch count increases (cross the 95% accuracy within 15 epochs), then more slowly until it reaches a maximum. Concurrently, the classification loss leveled out towards a minimum within 50 epochs.

To better understand the functionality of the MXene-based nonlinear AFs, an independent CNN architecture was constructed to numerically characterize their performance on the handwritten machine-learning digits classification task. This deep structured learning architecture functions under a different method than the first studied FFNN, as mentioned in section 2.3.2. The decomposition of the studied CNN architecture into individual layers is shown in Fig. 24a, along with an example of an output predicted label corresponding to an input handwritten digit image. The MNIST handwritten digital dataset was used in the CNN model's input layer with $28 \times 28 \times 1$ dimensions corresponding to the width, height and depth (the last dimension is the color channel which is 1 represents a grayscale image). The input experiences three successive convolution layers with nonlinear AFs, pooling, and a final fully connected layer followed by a softmax function. The output consists of 10 neurons corresponding to 10 classes of output, each representing a digit ranging from 0 to 9.

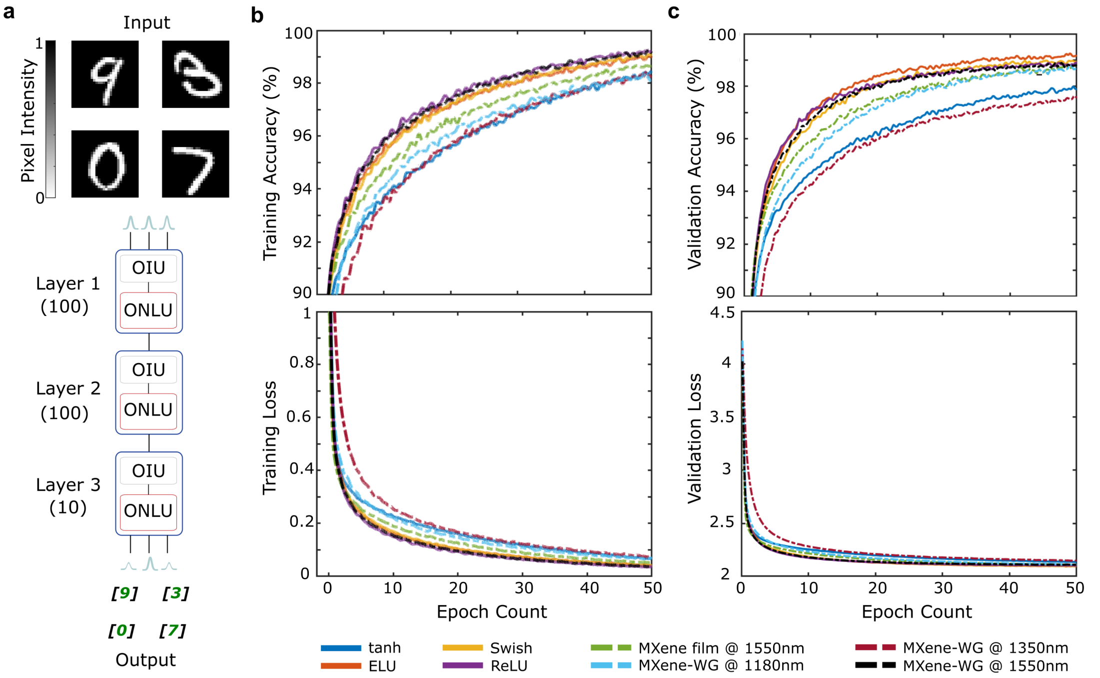

Figure 23 | Photonic FFNN performance on MNIST classification with MXene-based nonlinear AF. a, Schematic diagram of the studied photonic fully connected deep structured learning architecture, in which each layer is formed of OIU and ONLU. The output shows a sample of network-predicted labels corresponding to four handwritten digit inputs. **b-c,** MNIST handwritten digit classifiers' accuracy and loss as a function of epoch count during the training (**b**) and validation (**c**) processes utilizing all-optical nonlinear AFs based on rib waveguide covered with MXene flakes overlayer and MXene thin-film versus traditional AFs.

The network prediction accuracy and loss comparison between utilizing the studied all-optical MXene-based and commonly used software-based nonlinear AFs during the training phase are shown in Fig. 24b. The network prediction accuracy and loss of the validation dataset as a function of epoch count are shown in Fig. 24c to validate the models' performance. The studied photonic MXene-based AFs achieve prediction accuracy between 98.3 % and 99.7 %. All models are found to converge within 50 epochs to negligible loss, whereas the accuracy increases (cross the 96% accuracy within 13 epochs) until it levels out towards a maximum.

Through these comparisons of two independently deep learning architectures, FFNN and CNN (Fig. 23 and Fig. 24), the studied AFs MXene-based mechanisms in NIR provide competitive performance in terms of accuracy and loss as a function of epoch regarding the well-established and commonly used nonlinear AFs on classifying handwritten digits images task from the MNIST dataset. It is worth mentioning that excluding the examined classification examples, there are numerous machine learning applications and tasks where the studied nonlinear AFs play an essential role in the NN system. Moreover, there are various deep structured learning architectures where such nonlinear AFs are frequently employed in addition to the two configurations demonstrated in this work.

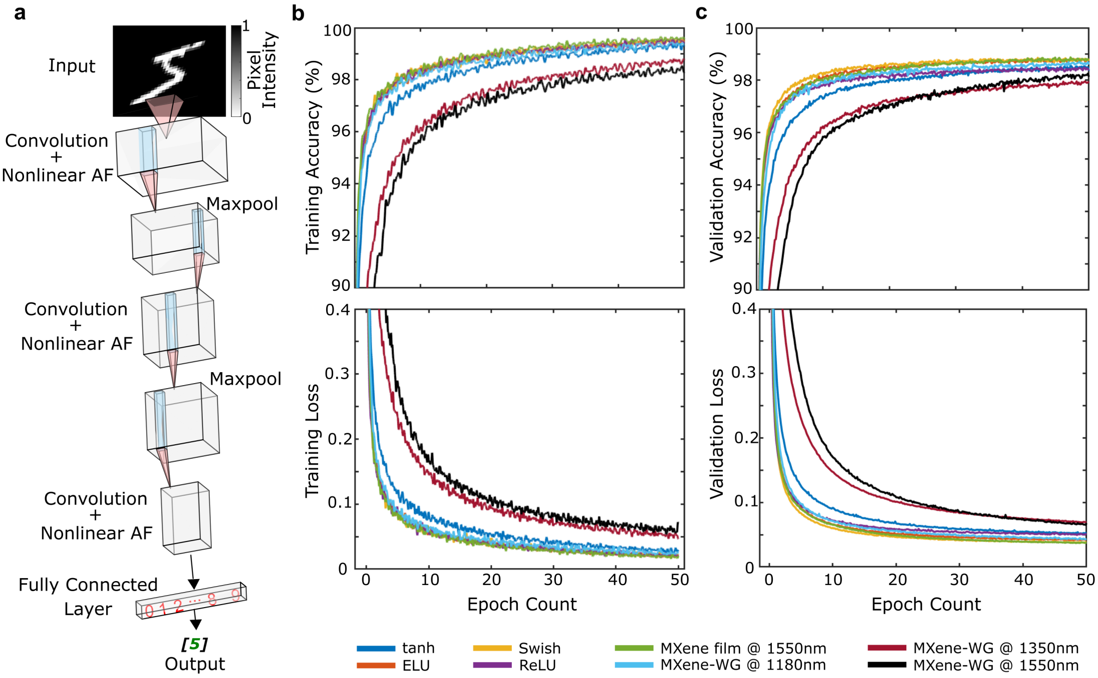

Figure 24 | Performance of CNN configuration on MNIST classification with MXene-based nonlinear AF. a, Schematic diagram of the studied optical CNN architecture contains convolutional layers with nonlinear AFs, pooling, and a fully connected layer, resulting in outputs ranging from 0 to 9. The output shows an example of a predicted label corresponding to a handwritten digit input image. **b-c,** Epoch count dependency of accuracy and loss on MNIST handwritten digit classification through the training (**b**) and validation (**c**) phases employing all-optical nonlinear AFs based on MXene flakes overlayer on silicon waveguide and MXene thin-film compared to software-based AFs.

To summarize, I have demonstrated an all-optical nonlinear AF operating in a wide spectral range. Two independent configurations were designed for both free-space and integrated photonics approaches. Moreover, the proposed free-space MXene configuration could be expanded to serve as ONLU for a photonic integrated circuit, in which in-plane optical saturable absorption covers the output facet of the waveguides. Focusing on the nonlinear neuron unit, I study its all-optical nonlinear AFs utilizing unique light-MXene interactions. $Ti_3C_2T_x$ MXene thin films and MXene overlayers on waveguides were manufactured, and the nonlinear optical responses in the cases of: 1) evanescent excitation; 2) free-space illumination were measured experimentally. Through a combined approach of experimental measurements and NN emulation, the photonic NN's performance in terms of accuracy and loss a function of the epoch were examined with respect to the software-based nonlinear AFs in deep structured learning tasks.

3.2 On-Chip Quantum Money

Developing practical methods and architectures for quantum technologies is becoming an increasingly important field. In particular, quantum information study presents many approaches that make their application extremely attractive, including guaranteeing the security of quantum money (QM) and tokenized signature schemes [52, 53]. These utilize unique quantum principles such as the no-cloning theorem and Heisenberg's uncertainty principle, providing advantages beyond what is possible with conventional classical cryptography. A QM scheme enables the creation of verifiable quantum banknotes by a trusted bank for untrusted users used in authenticated transactions that cannot be forged - achieved by unclonable quantum states by embedding a sequence of qubits prepared from a set of different bases.

Wiesner's QM protocol [38] is widely considered to be the first proposed quantum cryptographic application (detailed in sections 1.2.2 and 2.4). There are individual proof-of-principle demonstrations of both time-bin and polarization encoding for implementing a QM scheme. However, they are all free-space [43–45] and optical communication components [46, 47] usage-based. Here, a photonics candidate construction based on guided-wave optics for on-chip quantum tokens is presented - which may allow QM to rely on classical verification and is also compatible with tokenized signature schemes.

3.2.1 Classically Verifiable Quantum Money Scheme

Generally, a QM scheme aims to construct unforgeable banknotes with quantum states for an authenticated transaction with maximal security guarantees. That ensures that an untrusted holder cannot reproduce the quantum states to copy it or increase the amount of money. The introduction of a classical channel within the token [40, 43–45] verification phase in Wiesner's original QM (as detailed in section 2.4) can provide a practical realization satisfying unforgeability with unconditional security [45] (i.e., the money state uses quantum state $|\psi\rangle$ of N qubits that cannot be used for verification more than once, based only on the laws of nature without bounding the available technology of dishonest users) [40, 48–50, 117, 139]. It is worth mentioning that the main difference between the traditional QM scheme and the classically verifiable QM scheme is the verifying method - which is done by interactive protocol with classical communication between the bank and the honest holder (e.g., client), in particular, the verification phase does not require quantum communication. Since the answers corresponding to the quantum measurement results are in the form of a classical bit string, the verifier who applies quantum measurements communicates the measurement outcome with the bank via a typical classical channel to validate or reject the QM. Namely, the verifier's terminal sends the classical outcomes of those measurements to the bank in one classically communication round for verification [46, 48].

In a refinement of this scheme, the usage of quantum money states is extended to another notion: quantum tokens for digital signatures, and quantum tokens for message authentication codes [52], which require a secret key in their verification. This tokenized construction is based on the QM scheme establishing the quantum states via hidden subspaces of the vector space $\mathbb{F}_2^N$ [51]. Following the qubits scheme introduced in Ref. [51, 52], each money state $|A\rangle$ uses N qubits (or this would be the signing token) which are in a uniform superposition of the vectors in a random $N/2$ dimensional subspace $A \leq \mathbb{F}_2^N$, defined by $|A\rangle = \frac{1}{\sqrt{|A|}} \sum_{x \in A} |x\rangle$ with N-qubit basis states $|x\rangle$. In addition, applying the Hadamard operation on each qubit of the state $|A\rangle$ gives the state $H^{\otimes N} |A\rangle = |A^{\perp}\rangle$, or equivalently performing a quantum Fourier transform (a.k.a QFT) over $\mathbb{F}_2^N$.

According to the tokenized scheme, the signing authority secretly and securely generates a random $N/2$ dimensional subspace A as a secret key s and quantum state $|A\rangle$ of N qubits as the signing token to allow the signature of a document. To this end, a non-zero element in A and a non-zero element in the dual space $A^{\perp}$ may correspond to a signature for the bit values 0 and 1, respectively. If a dishonest user holds the signing token, the measurement on $|A\rangle$ can be performed either on the standard basis or the Hadamard basis. As a result, an element of A or $A^{\perp}$ can be obtained, respectively. Without the sequence associated with a set of bits indicating the correct measurement bases, an untrusted holder cannot measure $|A\rangle$ in both bases. Therefore, the quantum information cannot be read or reproduced at will. Since once the qubit is measured, its original quantum state collapses (section 2.4) to the measured state value. By contrast, the honest verifier who knows the secret key s (i.e., the relevant subspace A and $A^{\perp}$) can deterministically distinguish between $|A\rangle$ and $|A^{\perp}\rangle$, associated with the bit values 0 and 1, to validate or reject the signing token.

In general, any scheme for producing quantum tokens for QM or message authentication codes consists of two main processes: 1) a procedure for the bank (or the signing authority) to prepare the QM (or signing token), and 2) a method to verify the quantum token's authenticity and reject when discovering fraud attempts. It is worth mentioning that the N qubits money state utilized for the QM scheme can also be used as quantum signing tokens for a private tokenized signature scheme [52].

The practical quantum token protocol depicted in Fig. 25 is based on the theoretical works of preparing the quantum state upon the proposal in Refs. [51, 52], in conjunction with the techniques developed in Refs. [46, 48] uses only Bennett-Brassard 1984 (BB84) states (that form a larger state $|\psi\rangle$) and a single round of classical communication for the verification. Fig. 25 demonstrates the entire life cycle of the qubits' sequence embodied in token states, together with the sequence of interactions between the three entities in this setting: the trusted authority (e.g., bank), an honest holder (e.g., client), and an honest verifier (e.g., vendor). Through generating algorithm, the bank obtains a unique serial number i and a classical description $\mathcal{A}$ of a randomly-chosen subspace A. While this classical description has been kept secret, the bank distributes the state $|\psi\rangle$ prepared via $\mathcal{A}$. Considering the bank prepares a QM state $|\psi\rangle$ uses two qubits (i.e., $N = 2$), the space $\mathbb{F}_2^2$ consists of 4 vectors 00, 01, 10, 11, and for instance, one option for the subspace A could be the vectors 00, 10. Hence, the QM state $|\psi\rangle$ in this case, is the two-qubit state: $\frac{1}{\sqrt{2}}(|00\rangle + |10\rangle)$. The corresponding dual space $A^{\perp}$ consists of the vectors 00, 01, and the state $|\psi^{\perp}\rangle$ is the two-qubit state: $\frac{1}{\sqrt{2}}(|00\rangle + |01\rangle)$. In general, the transform $|\psi\rangle$ to $|\psi^{\perp}\rangle$ and vice versa can be achieved by applying a Hadamard operation on each qubit (e.g., $H_2^{\otimes 2}|{+}0\rangle = |0{+}\rangle = (|00\rangle + |01\rangle)/\sqrt{2}$). Utilizing the description $\mathcal{A}$ of A, the bank can produce the quantum state $|\psi\rangle = |{+}0\rangle$ (i.e., $|{+}0\rangle = (|00\rangle + |10\rangle)/\sqrt{2}$). Considering the case of the two-qubit state, the bank, in principle, can choose to encode the quantum token using a different sequence of the two-qubit state in $\{|{+}0\rangle, |{-}0\rangle, |{+}1\rangle, |{-}1\rangle, |0{+}\rangle, |0{-}\rangle, |1{+}\rangle, |1{-}\rangle\}$.

A trusted holder (or signer) who gets the quantum token from the bank (or trusted authority) can pick which transaction to perform (alternatively, pick a document to sign). Considering the token is sent directly to the verifier's terminal without temporary storage, its goal is to perform a quantum measurement on $|\psi\rangle$ either in the standard basis or in a different (Hadamard) basis to get a uniformly random element of A or $A^{\perp}$, respectively. The answers corresponding to the measurement results are a sequence of classical bits that eventually serve as inputs to the verification procedure along with the secret key s. That allows verifying whether the quantum token is valid by deterministically distinguishing between $|\psi\rangle$ and $|\psi^{\perp}\rangle$ associated with the bit values 0 and 1 via comparing to the relevant classical description of the chosen subspace. Namely, the verifier's terminal measures each of the N qubits of $|\psi\rangle$ in a randomly chosen basis to reproduce the encoded information based on the classical description $\mathcal{A}$ of A. In the example above, the state $|+0\rangle$ has an equal chance (i.e., 50% probability) of being measured in the standard basis in the states $|00\rangle$ or $|10\rangle$. At the same time, it has a 0% chance of being measured in the states $|01\rangle$ or $|11\rangle$. In general, if the single qubit is in the state $|0\rangle$, the measurement in the standard basis is certain to be $|0\rangle$. However, the measurement of this qubit in the Hadamard basis is entirely random. Hence, if the token is in the state $|+0\rangle$, the measurement in the standard (Hadamard) basis has a deterministic outcome in the rightmost (leftmost) qubit, i.e., is certain to be $|0\rangle$ ($|+\rangle$).

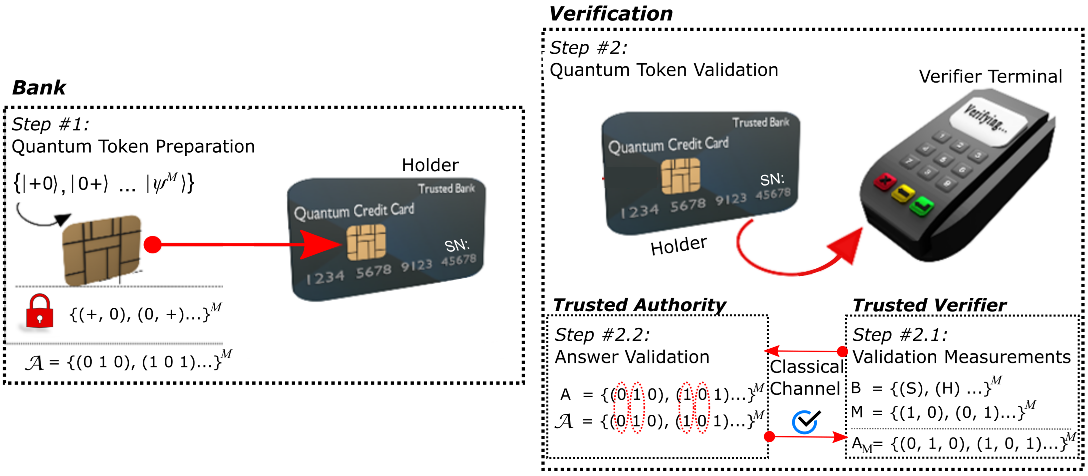

Figure 25 | Schematic illustration of classically verifiable QM scheme as a quantum token. The bank prepares M quantum states according to a random secret string $\mathcal{A}$ containing a classical description of the chosen subspaces. It allocates a unique serial number (SN) to the quantum card, which is then given to a trusted holder. In order to verify the quantum token, the verifier's honest terminal randomly selects one of the two bases for each state and performs the corresponding measurement. Upon an input bit, the honest verifier applies a Hadamard operation (H) or measures on a standard basis (S). The measurement outcomes (M) and the representing bits of the measurement bases (B) are then sent for comparison with the bank's secret key. The token is finally accepted as valid if the answers ($\mathrm{A_M}$) correspond to the measurement results and are consistent with secret string $\mathcal{A}$ - otherwise, it is rejected.

Given that the verifier can access the secret key in the private setting, it allows the verifier to test the relevant subspace membership for reading the encoded quantum information. Since the answers corresponding to the measurement results are in the form of a classical bit string, the verifier can communicate the measurement outcomes with the bank (or trusted authority) using a typical classical channel. In the example above, the measurement outcome can first consist of the chosen basis (e.g., 0 for the standard basis and 1 for the Hadamard basis) followed by the corresponding measurement results (i.e., the answer might be 010 in this case). Finally, the trusted authority can accept or reject the quantum token in one classically verification round, in which the verifier transmits the data of all the measurements answers to test the outcomes with the corresponding secret key and return its decision: token valid or invalid. The described protocol constructs a quantum token consisting of a single bit and can easily be extended to such a scheme in which the quantum token supports M bits. That can be accomplished via duplicating the depicted protocol M times. The bank independently and randomly chooses M strings of N bits constituting the quantum token identified with elements of the vector space $\mathbb{F}_2^N$ associated with different randomly chosen subspaces.

3.2.2 Design Integrated Photonics Architecture for Quantum Money

Two guided-wave optics devices are designed for fast and efficient classically verifiable quantum photonic tokens. Following the honest scheme previously discussed, qubit states are mapped onto weak coherent states utilizing a set of discrete waveguide normal modes. These demonstrate the entire life-cycle of the qubits' sequence embodied in a quantum token: from preparation using a monochromatic optic wave and waveguide-based building blocks for manipulating and modulating the propagating light to verification, allowing the honest verifier to reproduce the detected quantum state and sharing the classical outcomes of the quantum measurements.

The schematic illustration of the designed chip-to-chip photonic system is depicted in Fig. 26. In analogy to optical communication, the scheme's two main processes are composed of a photonic transmitter and receiver. Namely, the former is a device that can prepare the encoded qubits $|\psi\rangle$ according to the choice of A and $A^{\perp}$, and can send this state (e.g., holder's quantum credit card). The letter is a device that can apply quantum measurements to the sent states (e.g., vendor's payment terminal) and communicate the classical outcomes. More precisely, upon an input bit, the receiver either measures the received qubits in the standard basis to get an element of $|\psi\rangle$ or applies the Hadamard operation to get an element of $|\psi^{\perp}\rangle$. The answers corresponding to the measurement outcomes are in the form of a sequence of classical bits used for the verification procedure, along with the choice of the measurement basis - which compares it with the classical description $\mathcal{A}$ of A and $A^{\perp}$, this can be done on a classical computer.

In the quantum token preparation phase, weak coherent states of light are produced for probabilistically creating single-photon pulses. This corresponds to the characterization of a highly attenuated laser pulse that delivers a clocked manner of wavepackets of light. The optical field's polarization states that characterize the discrete guided modes supported by the waveguide are applied to weak coherent states $|\alpha_m\rangle = e^{-\frac{1}{2}|\alpha_m|^2} \sum_{\mathcal{N}=0}^{\infty} \frac{\alpha_m^{\mathcal{N}}}{\sqrt{\mathcal{N}!}} |\mathcal{N}_m\rangle$, where $\mu_\alpha = |\alpha_m|^2$ is the average number of photons in a clock cycle, $|\mathcal{N}_i\rangle$ are the photon number states, with a probability of finding $\mathcal{N}$ photons in a given mode m follows the Poisson distribution (i.e., $P(\mu_\alpha, \mathcal{N}) = \mu_\alpha^{\mathcal{N}} e^{-\mu_\alpha}/\mathcal{N}!$). According to the tokens scheme, the transmitter does not necessarily need to contain its own light source, in fact, an off-chip device allows more flexibility and reduces the dimensions of the holder's credit card device. In addition, the components constructing the chip-to-chip system, from the light source over the various guided-wave optics building blocks to single-photon detectors, operate at the C-band to take advantage of the lower loss at a wavelength of 1550 nm commonly used for optical communication.

The schematic of the transmitter implementation is shown in Fig. 26a, consisting of a photonic circuit with two successive EO intensity modulators followed by a beam splitter whose outputs are directed to an EO polarization modulator and an off-chip power meter. Calibrating the light source and setting the average photon number per pulse μ_α relies on modulating the steady emission provided by the laser to produce a block of consecutive pulses, then highly attenuating the outputs to determine the incident optical power P_{in}. In general, the photon flux (i.e., the number of incident photons per second) is determined by $P_{\text{in}}\lambda/hc$, where h is Planck's constant, c is the speed of light in vacuum, and λ is the wavelength of the associated optical wave. The light emitted from a monochromatic CW source feeds the input spatial mode of the MZI. The power of the incident optical wave is split equally into two waveguides that form the two MZI's arms. When an external electric field is applied to one arm, the RI of the material is modified, resulting in modulation of the phase of the optical field propagating through this waveguide. Combining two waves with different phase changes via a standard Y-branch at the end of the MZI obtains interferometrically intensity modulation. Changing the applied voltage allows the light's output power to continuously be controlled for setting the pulse duration and its repetition rate. Then, additional MZI is placed and used as a variable optical attenuator to reduce the optical power carried by the output pulses. Next, the light pulses go through another Y-branch to split the light pulses from one waveguide into two waveguides with a high splitting ratio such as 99:1, enhancing the required attenuation. The off-chip photodiode is used to monitor the power of the incident wavepackets for adjusting the average photon number μ_α.

The polarization information, which depends on the trusted authority's secret key (the classical description $\mathcal{A}$), is encoded on each pulse via a multi-stage EO phase modulator for modulating the polarization state to create the quantum token described in section 3.2.1. By applying appropriate voltages to electrodes on top of the modulator's waveguide, a distinct lightwave polarization state can be achieved to satisfy the qubit state in one of the two bases: the standard or the Hadamard bases, as detailed in the remainder of this section. In particular, the secret key containing the randomly chosen subspace corresponds to the control voltage sequences, which simultaneously indicate the correct measurement bases. In particular, these optical blocks encode quantum information in guided modes of weak coherent states of the optical field carried through the holder chip via waveguides to be sent directly to the verifier's terminal chip without temporary storage in a quantum memory. In the end, the verifier will have the $|\psi\rangle$ state and the holder won't anymore.

Because of the probabilistic behavior of the photon number distribution in a given mode for a weak coherent state of light, there is no specific way that generates optical wavepackets containing just one photon in a clocked manner with high fidelity and efficiency. In other words, there are different options for how the photons will be distributed within these clock cycles, which incorporate emission probabilities of vacuum pulses, single-photon pulses, and multi-photon pulses. In general, it is essential to prevent multi-photon wavepackets in the various quantum schemes since counterfeiters attacking via photon-number splitting may be attractive in such a scenario. Accordingly, this can be achieved by setting a small value of the average number of photons in clock cycle μ_α, through high attenuation experienced by the incident optical wave, which manages the emission probabilities of both vacuum and multi-photon wavepackets. In this weak regime (i.e., small values of μ_α), the value of μ_α falls well below 1, where the multi-photon to single-photon emission probabilities ratio bounded to $\frac{\mu_\alpha}{2}$ on the one hand, it enhances the emission probability of vacuum wavepackets to $1 - \mu_\alpha$ on the other hand [111]. Generally, the photon arrival rate can be expressed as $R_{\text{inc}} = f_{\text{rep}}\mu_\alpha$. The mean number of photons μ_α per detection time interval, taking into account experimental parameters, at the transmitter's output is given by:

$$\mu_\alpha = \frac{\lambda}{hc}\frac{\tau_{\text{SPAD}}}{\tau_{\text{d}}}\frac{t_\eta P_{99} t_{1/99}}{f_{\text{rep}}} \tag{3.6}$$

where hc/λ is the energy per photon of the optical wavepacket with average power P_{in}, $P_{99} = 0.99P_{\text{in}}$ is the output measured average power from the 99-port of the Y-branch with a transformation splitting ratio efficiency of $t_{1/99} = 1/99$, t_η is the transmission efficiency of the multi-stage EO phase modulator, τ_{SPAD} is the detection time window of the single-photon avalanche detectors (SPAD), and τ_{d} and f_{rep} are the pulse duration and its repetition rate, respectively. As seen from Eq. (3.6), the value of μ_α can be adjusted for different experiments by modifying the characterizations of the incident light without modifying the transmitter's physical structure. Both the transmitter and receiver are controlled using a combination of bias voltage $\overline{V}$ and electrical signals $\tilde{V}$ sent from a pulse generator to manage the EO phase modulators.

The schematic of the receiver implementation for the quantum token validation is shown in Fig. 26b. The verification phase requires each block of qubits to be measured via the verifier's terminal in one of two measurements, each corresponding to a randomly chosen measurement basis: either the standard basis or a different (i.e., Hadamard) basis. This is accomplished by utilizing MZI, whose output ports are connected to other waveguides to select between two paths. The wavepackets can be spatially switched between the two output waveguides by adjusting the applied voltage across one of MZI's arms. Next, two NIR SPADs are employed for each photonic path, each at an output spatial mode of a polarization beam splitter based on typical polarizing directional couplers that route the fundamental TE- and TM- guided modes into two other different waveguides. While one photonic path allows measuring the state in the standard basis to distinguish between $|\leftrightarrow\rangle$ and $|\updownarrow\rangle$ states, the second photonic path additionally employs a voltage-controlled $\lambda/2$ waveplate with a fixed orientation angle of 22.5° for implementing Hadamard operation optically (detailed in the remainder of this section) that allow measuring the input state in the other basis $\{|\nearrow\rangle, |\nwarrow\rangle\}$.

Due to the two different coupling lengths for the TE- and TM- polarized guided modes, the verifier can perform a measurement at the directional couplers' output ports of the chosen path (i.e., corresponding to the randomly selected basis) for each of the N transmitted token states. The off-chip SPADs modules can then be utilized to detect the spatial output modes associated with the weak coherent states and record the detection events of the receiving optical wavepackets block. Next, the data from the SPADs can be transmitted and stored in a classical computer for postprocessing once all measurement rounds are ended (i.e., for each received qubit's state), allowing to complete the token verification classically. In particular, the answers corresponding to the measurement results are in the form of a sequence of classical bits (e.g., 0 can be associated with the detected states $|\leftrightarrow\rangle$, $|\nearrow\rangle$ and 1 to the detected states $|\updownarrow\rangle$, $|\nwarrow\rangle$).

Eventually, the verifier has access to the secret key (i.e., the chosen A or $A^\perp$) in the token scheme's private setting, as described in section 3.2.1. Therefore the quantum information encoded in the set of normal guided modes can be read by deterministically distinguishing between $|\psi\rangle$ and $|\psi^\perp\rangle$ based on the chosen measurement basis. Alternatively, the verifier can communicate with the trusted authority the sequence of the classical measurement outcomes together with the sequence of classical bits corresponding to its randomly chosen measurements basis. By one classically verification round, the trusted authority can validate or reject the quantum token via transmitting the data utilizing a typical classical channel.

Since the verification requires randomly choosing between two measurements (i.e., one of the switch's spatial modes), the system can use only two SPADs by incorporating two output ports from different polarizing directional couplers. Hence, a mesh of MZIs or integrated combiners at the end of the receiver circuit can be utilized (as shown in the configuration in Fig. 10) or two 2×1 fiber-couplers directly connected to the SPADs (as shown in the setup in Fig. 29) to recombine the two output ports (i.e., the pair of output ports labeled $\{\leftrightarrow, \nearrow\}$, and the ports labeled $\{\updownarrow, \nwarrow\}$). Considering the weak coherent wavepackets arrival with mean photon number μ_α and losses represented by $e^{-\mu_\alpha \eta}$, the verifier measures each of the N quantum token states in its chosen random basis and outputs $(1 - e^{-\mu_\alpha \eta})N$ measurement outcomes. The count rate is $R_{\text{det}} = f_{\text{rep}}(1 - e^{-\mu_\alpha \eta})$, wherein the limit of $\mu_\alpha \eta << 1$ approximates $\approx \mu_\alpha \eta f_{\text{rep}}$. The overall detection efficiency, η, is the product of the channel transmission efficiency and quantum efficiency of a threshold single-photon detector, $\eta = \eta_T \eta_{det}$.

Following the designed chip-to-chip photonics system, the qubits can be realized by a set containing two orthogonal polarization waveguide modes. Given a typical wire waveguide, the 0 logical state $|0\rangle$ can be encoded into the first normal mode TE_{00} and the 1 logical state $|1\rangle$ encoded by the second orthogonal normal mode TM_{00}. Since the light propagation nature in discrete waveguide modes, these qubits can be applied to both quantum states (e.g., single-photon states) and classical states (e.g., coherent states) of optical fields. The qubit states may be mapped onto two-mode weak coherent states of the optical field in which $|0\rangle \rightarrow |\text{TE}_{00}\rangle \otimes |\text{vac}\rangle$, $|1\rangle \rightarrow \text{TM}_{00} \otimes |\text{vac}\rangle$, $|+\rangle \rightarrow |\text{TE}_{00}\rangle \otimes |\text{TM}_{00}\rangle$, and $|-\rangle \rightarrow |\text{TE}_{00}\rangle \otimes |e^{j\pi}\text{TM}_{00}\rangle$, where $|\text{vac}\rangle$ represents the vacuum state. The optical waves travel in the waveguide along the z direction in distinct optical modes that mathematically represent a solution to Maxwell's equations under the appropriate boundary conditions imposed by the waveguide geometry and materials. The dispersion equations (a.k.a. eigenvalue equations) are provided by the scalar wave equation (Eq. 2.4) solutions, along with the boundary conditions matching at the interfaces between planes of different RIs (i.e., at core interfaces), which require the continuity of the electric field function and its first derivatives. Therefore, only certain discrete values of propagation constant β are allowed. Accordingly, just a limited number of guided modes can be supported depending on the waveguiding region's physical dimensions, the structure's RI distribution, and the light's wavelength. These discrete values of β correspond to the different optical modes associated with two families: TE and TM optical modes. The two orthogonal polarized optical modes can constitute a complete set of functions, so an arbitrary optical field distribution that satisfies the boundary matching condition can be described in terms of them. The qubit's state can be described as a superposition of the two basic normal modes $|0\rangle$ and $|1\rangle$ as: $|\psi\rangle = a_0 |0\rangle + a_1 |1\rangle$.

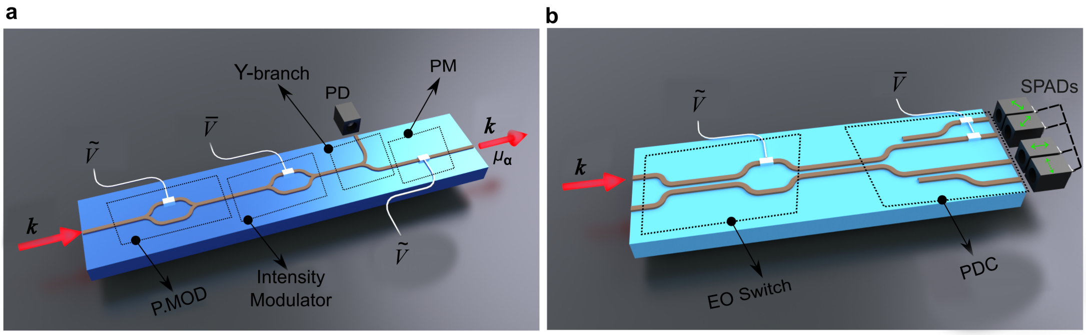

Figure 26 | Integrated photonics devices for the proposed on-chip quantum tokens architecture. a, A reconfigurable integrated transmitter holder chip, consists of MZI formed by an EO phase shifter and Y-branch splitter/combiner, to perform pulse modulation (P. MOD) of the monochromatic input light emitted from a CW laser. An intensity modulator, an off-chip photodiode (PD), and a Y-branch splitter allow the light source to be calibrated by controlling the average photon number per pulse μ_α at the output. According to the scheme, an EO polarization modulator (PM) is then used to encode the quantum information in the polarized normal guided modes of weak coherent states of light via applying appropriate voltages. The wavevector $\boldsymbol{k}$ (red arrows) indicates the propagation direction of the light. **b,** A photonic receiver circuit realizes the verifier's terminal chip for deterministically distinguishing the quantum states with off-chip NIR single-photon avalanche detectors (SPAD). MZI is formed by directional couplers and configured with an EO phase shifter. That allows for an EO-controlled spatial switch between the two output waveguides, which include polarizing directional couplers (PDC) and a phase modulator. The EO phase modulators are controlled by combining bias voltage ($\bar{V}$) and electrical signals ($\tilde{V}$) sent from a pulse generator.

The same material was considered for all the involved building blocks to simplify the implementation of the proposed chip-to-chip system. The LiNbO$_3$ waveguide platform provides high-performance devices with large bandwidths and is ideal for forming high-speed modulation systems [140], which is required for the various components in the integrated photonics circuit. The waveguide structure is usually fabricated by local Ti-indiffusion into the core region in which the core RI n_{core} is greater than both RI of the substrate and cladding to satisfy the guiding condition, as seen from Eq. (2.1). The numerically calculated mode effective index n_{eff} of the different orders of supported guided mode as a function of the core width at a fixed wavelength of 1550 nm are depicted in Fig. 27a, together with the electric field distributions of the first three orders. The optical modes in the waveguide modeling were carried out using COMSOL Multiphysics in the wave optics module based on the finite element analysis method. A waveguide with core dimensions of 3 µm high and 4 µm width can be assumed to support only the 1st order of the two polarized normal modes, namely the fundamental quasi-TE_{00} and quasi-TM_{00} optical modes (the vertical red-dashed line in Fig. 27a). The upper bound of the SM region where only these two polarized modes are supported is depicted by the 2nd order mode cutoff indicated by the vertical black line in Fig. 27a.

The corresponding normalized electric field configurations of the fundamental TE_{00} and TM_{00} optical modes at a wavelength of 1550 nm are depicted in Fig. 27b-c, along with the RI distribution $n(x, y)$ of the waveguide structure. While the RI along the x direction exhibit a symmetrical profile, a step function is supported along the y direction. These obey the wire waveguide as illustrated in the inset of Fig. 27a which constructed by a core with $n(\lambda = 1550\ \mathrm{nm})_{\mathrm{core}} = 2.22$ in which the light is confined, immersed in a $\mathrm{LiNbO_3}$ substrate $n(\lambda = 1550\ \mathrm{nm})_{\mathrm{sub}} = 2.2$, and both are in contact with air $n(\lambda = 1550\ \mathrm{nm})_{\mathrm{clad}} = 1$. The calculated electric field profiles $|E(x, y = -1.5\ \mu\mathrm{m})|$ and $|E(x = 0, y)|$ as a function of x and y are qualitatively similar for these optical modes of the same order. They have quite similar mode effective indices, but the electric fields point in different directions. While the main transverse field component of the TE mode is E_x, the E_y is the dominant transverse field component of the TM mode. Given that the two TE_{00} and TM_{00} modes are characterized by propagation constants β_1 and β_2 with electric fields $E_1 = A_1\mathcal{E}_1(x, y)e^{-j\beta_1 z}$ and $E_2 = A_2\mathcal{E}_2(x, y)e^{-j\beta_2 z}$, respectively, the $|\leftrightarrow\rangle$ state (or $|0\rangle$) and $|\updownarrow\rangle$ state (or $|1\rangle$) can be utilized to represent the bit values 0 and 1.

An expression for the electric field $E(x, y, z)$ propagating in the waveguide along the z direction can be written as a linear combination of the supported optical guided modes, i.e., $E(x, y, z) = \sum_m A_m\mathcal{E}_m(x, y)e^{-j\beta_m z}$, where A_m and $\mathcal{E}_m(x, y)$ are the amplitude and the transverse function of the corresponding mode m. An arbitrary local field $E(x, y, z)$ which propagates in the waveguide that supports the fundamental modes, can be expanded in terms of this set of normal modes $\{|\leftrightarrow\rangle, |\updownarrow\rangle\}$ when injected linearly polarized optical wave, at normal incidence, into the waveguide with a certain angle φ_{in} to the vertical. In addition, the electric field of optical guided mode $E_m(x, y, z)$ varies sinusoidally as a function of the z direction (i.e., proportional to $e^{-j\beta_m z}$). Thus, the optical field $E(x, y, z)$ has a unique representation based on the set of normal modes $\{|\mathrm{TE}_{00}\rangle, |\mathrm{TM}_{00}\rangle\}$ of the form:

$$E(x, y, z) = K_1\mathcal{E}_1(x, y)e^{-j\beta_1 z} + K_2\mathcal{E}_2(x, y)e^{-j\beta_2 z}\ . \tag{3.7}$$

where the constants are determined by $K_1 = A_1 \sin(\varphi_{\text{in}})$ and $K_2 = A_2 \cos(\varphi_{\text{in}})$. Accordingly, the state of a qubit can be described as a superposition of these two orthogonal states as $|\psi\rangle = K_1 |\leftrightarrow\rangle + K_2 |\updownarrow\rangle$.

The quantum information encoding at the end of the integrated transmitter circuit is performed using a guided optics wave multi-stage EO phase modulator. It contains a cascade of waveguide-based polarization transformers, which can be electro-optically adjusted to act as an individual on-chip variable waveplate with modifiable thickness and orientation by applying appropriate control voltages. This allows transforming an arbitrary input optical field's polarization state into a particular output polarization state in one of the two bases: the standard or the Hadamard bases, for each N-qubit state of the token $|\psi\rangle$. In principle, an arbitrary quantum state $|\psi\rangle = a_0 |\leftrightarrow\rangle + a_1 |\updownarrow\rangle$ can be prepared based on the set of these normal modes $\{|\text{TE}_{00}\rangle, |\text{TM}_{00}\rangle\}$, with $a_0 = \cos(\varphi)$ and $a_1 = e^{j\phi} \sin(\varphi)$ as derived from Eq. (2.21).

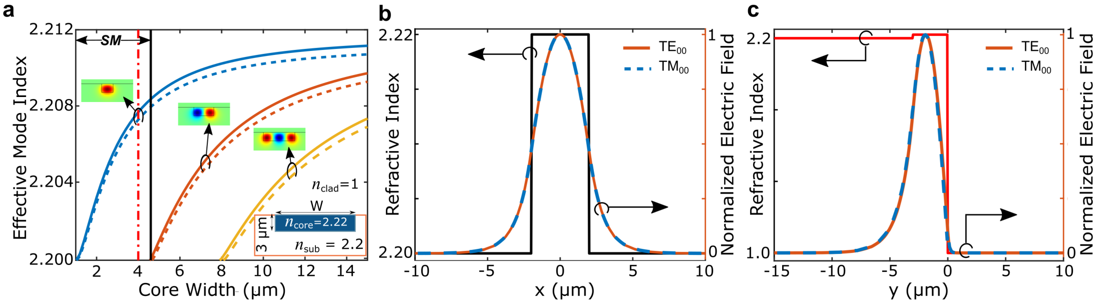

Figure 27 | Calculated electric field profiles of the supported modes for on-chip qubit realization. a, The dependence of mode effective index on the waveguide core width at a wavelength of 1550 nm for the first three orders of guided modes with their characterized electric field distributions. The solid curves indicate the TE modes, and the dashed curves indicate the TM modes. The black vertical line indicates the upper bound of the single-mode (SM) region. The designated SM waveguide with a 3 μm × 4 μm core cross-section is marked by the vertical red dashed line. The inset shows a wire waveguide with a guiding layer immersed in a substrate, and both are surrounded by air. **b-c,** The electric field profiles of corresponding fundamental TE$_{00}$ (orange curves) and TM$_{00}$ (blue dashed curves) normal modes as a function of the x (**b**) and y (**c**) directions, and the corresponding waveguide RI distributions.

A typical LiNbO$_3$ EO phase modulator consists of a single optical waveguide with three metallic electrodes: two symmetrically along the waveguiding (A and C placed on top of the substrate), and one on top of the core region (B). Its mechanism is established on the Pockels effect (a.k.a, the EO effect), where an external electric signal is used for controlling the waveguide's optical properties resulting in phase delay of the guided optical mode passing through the waveguide [3, 4]. Relying on the direction of the applied electric field, and the waveguide orientation, this phase delay can depend on the polarization direction. Therefore, such integrated photonics Pockels cell can act as a voltage-controlled waveplate for modulating the output optical field's polarization state by implementing a z-propagating waveguide in the x-cut substrate of LiNbO_3. While the optical mode travels without disturbance through the waveguide when no voltage is involved, the medium's RI experiences modifications depending on the applied electric field $n(E)$ in the region between the electrodes where the material birefringence behavior is proportional to the combination of applied voltages.

A phase delay of the TE and TM modes can be determined by the applied voltage differences of the outer electrodes where the center electrode is grounded [141]. In particular, the required operating voltages to achieve Λ-waveplate with an orientation angle $\varphi/2$ are:

$$\begin{aligned} V_A &= 2V_o \cdot \Lambda \cdot \sin(\varphi) - V_\pi \cdot \Lambda \cdot \cos(\varphi) + V_A^{\text{Bias}} \ , \\ V_B &= 0 \quad (\text{ Ground }) \ , \\ V_C &= 2V_o \cdot \Lambda \cdot \sin(\varphi) + V_\pi \cdot \Lambda \cdot \cos(\varphi) + V_C^{\text{Bias}} \ . \end{aligned} \tag{3.8}$$

where V_o and V_π are the voltage required to rotate all power from TE mode to TM mode, and the elemental voltage to induce a π phase shift between these modes, respectively. $\varphi/2$ denotes the angle between an input linearly polarized optical wave and the waveplate's fast axis adjusted with the polarization vector of fundamental guided mode TE_{00}. The bias voltages needed to be applied to electrodes A and C to achieve zero birefringences between the two orthogonal modes are $V_A^{\text{Bias}} \cong -V_C^{\text{Bias}}$.

There are various options to configure the integrated multi-stage EO transformer for modulating the polarization of the input optical wavepacket to achieve one of the four polarization states as required in the token state preparation. Considering unpolarized light launched into a cascade of waveguide phase modulators, the first polarization transformer stage can configure as a polarizer in the horizontal or vertical orientation. The input polarization state of the optical field can be transformed into horizontal or vertical states associated with the TE_{00} and TM_{00} modes, respectively. The successive stage can be configured in four extreme positions as a $\lambda/2$ waveplate with rotation angles of $\varphi/2 = 0°, 45°, \pm 22.5°$ achieved with the corresponding combination of the applied voltages according to Eq. (3.8). This allows the preparation of either $|\psi\rangle$ or $\left|\psi^\perp\right\rangle$. The action of the half-waveplate on these two modes can be defined by the corresponding projection operator given by:

$$\hat{A}_{\varphi/2}^{HWP} = \begin{pmatrix} \cos(\varphi) & \sin(\varphi) \\ \sin(\varphi) & -\cos(\varphi) \end{pmatrix} . \tag{3.9}$$

For the input states $|\psi_{\text{in}}\rangle = |\leftrightarrow\rangle$ and $|\psi_{\text{in}}\rangle = |\updownarrow\rangle$, the obtained output polarization states have the form of $|\psi_{\text{out}}\rangle = \hat{A}^{HW}_{\varphi/2}|\leftrightarrow\rangle = \begin{pmatrix} \cos(\varphi) \\ \sin(\varphi) \end{pmatrix}$ and $|\psi_{\text{out}}\rangle = \hat{A}^{HW}_{\varphi/2}|\updownarrow\rangle = \begin{pmatrix} \sin(\varphi) \\ -\cos(\varphi) \end{pmatrix}$, respectively. Assuming the excitation of the fundamental TE_{00} mode in the output of the first stage of EO waveguide modulator $|\psi_{\text{in}}\rangle = |\leftrightarrow\rangle$, the optical electric fields at the waveguide output for the four cases of $\varphi/2$ are pointed in four different directions $|\psi_{out}\rangle = \hat{A}^{HW}_{\varphi/2}|\psi_{in}\rangle$: 1) horizontal in which $|\psi_{\text{out}}\rangle = \hat{A}^{HW}_{0^\circ}|\leftrightarrow\rangle = |\leftrightarrow\rangle$. 2) vertical in which $|\psi_{\text{out}}\rangle = \hat{A}^{HW}_{45^\circ}|\leftrightarrow\rangle = |\updownarrow\rangle$. 3-4) diagonal or anti-diagonal in which $|\psi_{\text{out}}\rangle = \hat{A}^{HW}_{22.5^\circ}|\leftrightarrow\rangle = |\nearrow\rangle$ and $|\psi_{\text{out}}\rangle = \hat{A}^{HW}_{-22.5^\circ}|\leftrightarrow\rangle = |\nwarrow\rangle$.

The calculated optical electric field distribution associated with four different possible linear polarization orientations of the qubit state in the waveguide are shown in Fig. 28, along with the optical field pointing directions (depicted with the black arrows). These optical waves travel in the waveguide in distinct optical guided modes corresponding to the qubit states: $|\leftrightarrow\rangle$ (the TE_{00} mode), $|\updownarrow\rangle$, (the TM_{00} mode), $|\nearrow\rangle = \frac{1}{2}(|\leftrightarrow\rangle + |\updownarrow\rangle)$ and $|\nwarrow\rangle = \frac{1}{2}(|\leftrightarrow\rangle - |\updownarrow\rangle)$ (or $\frac{1}{2}(\text{TE}_{00} \pm \text{TM}_{00})$). While the $\{|\leftrightarrow\rangle, |\updownarrow\rangle\}$ basis eigenstates are represented with the two orthogonal polarized TE and TM modes, the $\{|\nearrow\rangle, |\nwarrow\rangle\}$ basis is depicted through their superpositions. The first and second qubit states in each basis can be employed to encode the bit values 0 and 1, respectively. In addition, the electric field of optical guided mode $E_m(x, y, z)$ varies sinusoidally as a function of the z direction (i.e., proportional to $e^{-j\beta_m z}$), and consists of a combination of two perpendicular in-phase components resulting in an electric field wave linearly change in the xy plane (e.g., horizontal polarization vector or right and left changes as the optical wave travels).

As seen from Eq. 2.20, the operation of a Hadamard gate on the logical states can be described by leaving the basis state $|\leftrightarrow\rangle$ unchanged and manipulating $|\updownarrow\rangle$ to $-|\updownarrow\rangle$, then mapping these basis states into their superposition: $|\leftrightarrow\rangle \rightarrow |\leftrightarrow\rangle + |\updownarrow\rangle$ and $-|\updownarrow\rangle \rightarrow |\leftrightarrow\rangle - |\updownarrow\rangle$. The realization of the Hadamard operation relies on the dependence of the phase delay on the polarization direction. Its mechanism corresponds to the optical functionality of a $\lambda/2$ waveplate oriented at $\varphi/2 = \pi/8$ (or 22.5°). This also can be accomplished by a guided optic wave device utilizing the integrated Pockels cell as described above for polarization state modulation of the incident optical wavepacket. By applying an appropriate external electric signal, the voltage-controlled waveplate adjusts its setting to $\Lambda = 1/2$ with an orientation angle $\varphi/2 = \pi/8$ for the required waveplate's behavior.

These parameters are chosen to utilize two properties: 1) a path phase shift of $\lambda/2$ is introduced between the TE- and TM-polarized waves propagating through the waveguide, which induces π phase shift between the polarization components of the optical field. and 2) an incident linearly polarized light rotates by twice the angle $\varphi/2$ between its polarization vector and the photonic waveplate's fast axis. Considering that the waveplate's fast axis is adjusted with the polarization vector of fundamental guided mode TE_{00} with the appreciated voltage differences following Eq. (3.8), the basis state $|{\leftrightarrow}\rangle$ remains unchanged. In contrast, the basis state $|{\updownarrow}\rangle$ associated with the orthogonal normal mode TM_{00} mapped into $-|{\updownarrow}\rangle$ due to the phase shift term (i.e., $e^{j\pi} = -1$). It is easy to see from Eq. (3.9), a uniform superposition of the standard basis states can be created with $\varphi/2 = \pi/8 \rightarrow \varphi = \pi/4$. In particular, $|{\nearrow}\rangle \equiv \frac{1}{\sqrt{2}}(|{\leftrightarrow}\rangle + |{\updownarrow}\rangle)$ and $|{\nwarrow}\rangle \equiv \frac{1}{\sqrt{2}}(|{\leftrightarrow}\rangle - |{\updownarrow}\rangle)$ can be achieved, which are associated with the required states of the Hadamard basis.

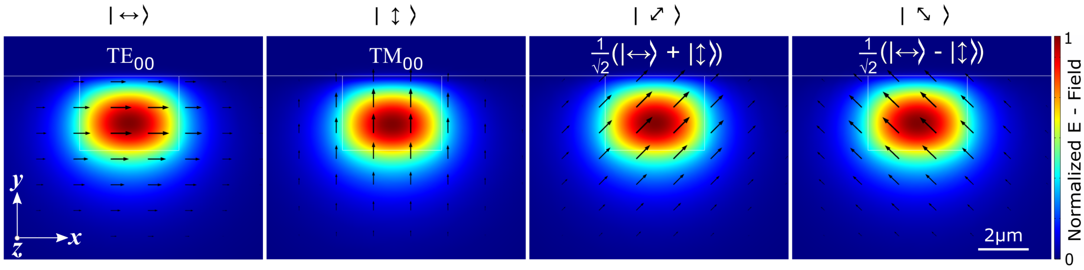

Figure 28 | Quantum state preparation and encoding of single qubit via optical waveguide modes. The calculated electric field distribution for four different possible orientations of the qubit state using a set of discrete waveguide modes. The black arrows indicate the polarization direction of the optical field. The fundamental TE_{00} and TM_{00} optical guided modes formed the mode basis $\{|{\leftrightarrow}\rangle, |{\updownarrow}\rangle\}$ encoding the bit values 0 and 1. The states $|{\nearrow}\rangle = (|\mathrm{TE}\rangle + |\mathrm{TM}\rangle)/\sqrt{2}$ and $|{\nwarrow}\rangle = (|\mathrm{TE}\rangle - |\mathrm{TM}\rangle)/\sqrt{2}$ are the basis eigenstates prepared via the superposition of these two fundamental normal modes.

3.2.3 Experimental Principles for Photonic Quantum Tokens Scheme

In order to provide a suitable environment for photonics-based quantum tokens and to visualize the end-designed chip-to-chip system, an experimental setup was planned. The experimental system operates at the C-band in NIR to take advantage of the lower loss at a wavelength of 1550 nm commonly used for optical communication. The photonic setup allows for fast and efficient verification of quantum tokens based on the on-chip realization depicted in Fig. 26. Each of the integrated photonics building blocks is implemented by a telecommunication fiber-coupled guided-wave optics device with the exact optical mechanism of operation. This allows physical tests to take place and characterize in terms of the dependence of the correctness on the wavepackets' average photon number prior to the chip system manufacturing for large-scale deployment together with near-future quantum storage devices.

The schematic diagram of the proposed experimental setup for the prototype quantum tokens is depicted in Fig. 29. It is divided into two optical interfaces following the analyzed scheme in the previous sections: 1) the quantum transmitter (e.g., the holder's quantum credit card), for preparing the token state via encoding the N qubits state in the polarization of weak coherent states of the optical field, and 2) the quantum receiver (e.g., the verifier's payment terminal), to perform a measurement on each of the N token states, in the standard basis or in another (Hadamard) basis for classically token verification.

In the quantum token preparation phase, a monochromatic light emitted from a CW laser can be used as the optical energy source in the setup. The light emitted at 1550 nm is launched into the EO intensity modulator, which allows pulse modulation of the incident optical wave. The optical source (KLS1550, Thorlabs) is connected to an EO $LiNbO_3$ modulator (LN81S-FC, Thorlabs) formed by a fiber-coupled MZI structure by an optical fiber (P1-1550A-FC, Thorlabs). The pulse duration and the repetition rate can be managed via a suitable electrical signal sent from a pulse generator. It is worth mentioning that all the involved integrated modulators can operate up to 10 GHz. However, the pulse repetition frequency is configured regarding the SPAD detection dead time τ. Namely, this satisfies that the frequency f_{rep} is lower than the maximum repetition frequency $1/\tau$ of the detectors (< 100 MHz). Then, the light experienced attenuation via passing through a fiber-coupled variable optical attenuator (V1550F, Thorlabs) followed by a fiber optic coupler (TW1550R1F1, Thorlabs) with a coupling ratio of 99 to 1 for routing the optical signal into two paths. While one is directed to the OSA to monitor the power of the incident optical signal, the other path is directed to a polarization controller (PC-B600SFASFA, EOSPACE) formed by a cascade of integrated polarization transformer stages. The wavepacket polarization can be selected via properly applied voltages, in which the optical output field is pointed in four different directions: $|\leftrightarrow\rangle$ (horizontal), $|\updownarrow\rangle$ (vertical), $|\nearrow\rangle$ (diagonal), and $|\nwarrow\rangle$ (anti-diagonal). The variable EO attenuator, OSA, and a fiber-coupled splitter allow the light source to be calibrated by controlling the wavepacket's average photon number μ_α.

In the verification phase, the holder's token state is encoded in the polarization of weak coherent states of the optical field. Then, it is sent directly to the verifier's terminal without temporary storage - to be measured in the basis randomly chosen by the verifier (either standard or Hadamard bases). The wavepackets are routed to one of two different optical paths using a 1×2 optical switch (OSW12-1310E, Thorlabs). While one optical path consists of a fiber-based polarizing beam splitter (PFC1550H, Thorlabs), the other employs an additional 3-paddle fiber polarization controller (FPC031, Thorlabs) acting as $\lambda/2$ half-waveplate oriented at 22.5° (for

Hadamard operation). Next, two 2×1 integrated combiners are utilized for connecting the four output ports of the polarizing beam splitters to two SPADs: the pair of output ports and labeled as $\{\leftrightarrow, \nearrow\}$, and the ports labeled $\{\updownarrow, \nwarrow\}$. Finally, two InGaAs/InP (indium gallium arsenide and indium phosphide) SPADs (IDQube-NIR-FR-STD, IDQ) are used for detection labeled SPAD$_{\leftrightarrow,\nearrow}$ and SPAD$_{\updownarrow,\nwarrow}$. These allow the verifier to distinguish between $|\leftrightarrow\rangle$ or $|\updownarrow\rangle$ states and between $|\nwarrow\rangle$ or $|\nearrow\rangle$ states, as detailed in the preceding section. Once all measurement rounds are ended for each of the N token states, the SPADs record measurement outcomes are eventually transmitted and stored in a classical computer to complete the token verification classically. The answers corresponding to the measurement results are in the form of a sequence of classical bits as well as the sequence of the randomly chosen measurement bases and, therefore, can be transmitted over a classical channel. The trusted authority compares these sequences with the secret key (i.e., the chosen A or $A^{\perp}$ also used for the qubits encoding).

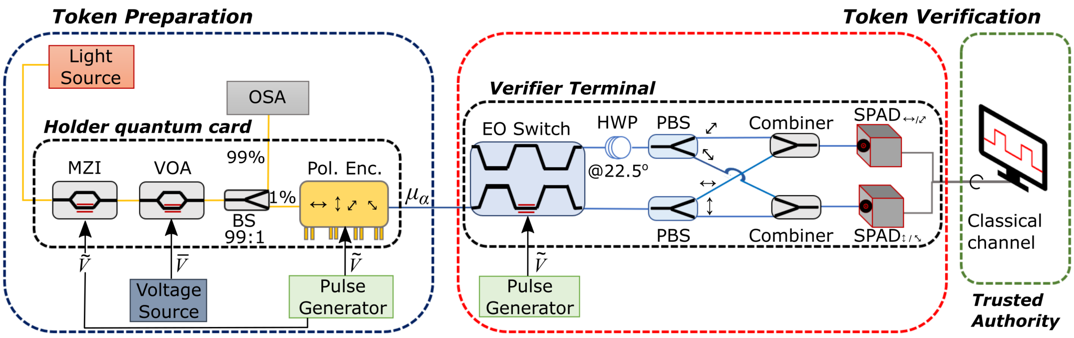

Figure 29 | Schematic diagram of the experimental setup for generating and verifying quantum tokens. In the token state preparation (blue frame), monochromatic light emitted from the CW laser passes through MZI for pulse intensity modulation. The electrically-controlled variable optical attenuator (VOA), OSA, and a fiber-coupled beam splitter (BS) are used to calibrate the light source and set the wavepackets' average photon number μ_α. A multi-stage integrated polarization transformer is then used to encode (Pol. Enc.) quantum information on weak coherent states of the optical field by applying appropriate voltages to be sent to the verifier terminal. The holder card (black frame) is controlled through a combination of bias voltage ($\bar{V}$) and electrical signals ($\tilde{V}$) sent from a voltage source and pulse generator. The verifier receiver terminal (red frame) combines an optical spatial switch and fiber polarization controller to create a half-waveplate (HWP) oriented at 22.5°, a polarizing beam splitter (PBS), and fiber-coupled combiners. This allows for deterministically distinguishing between the arrival qubit states ($|\psi\rangle$ and $|\psi^{\perp}\rangle$). Two single-photon avalanche detectors (SPAD) are placed at the end of the circuit to record the detection events. Electrical signals also manage the quantum receiver ($\tilde{V}$) sent from a pulse generator to control the EO switch allowing the verifier to choose between the two measurement bases (the standard or Hadamard).

To summarize, having presented the analyzed quantum tokens protocol includes the bank's procedures for preparing the quantum tokens and their verification, the design and implementation of a chip-to-chip system are demonstrated for practical photonic QM (as a quantum token) relying on classical verification, which is also compatible with the tokenized scheme for message authentication code. Two guided-wave optics devices were designed for quantum state preparation and classically verification. The transmitter and receiver serve as a trusted holder's quantum card and a verifier's honest terminal, respectively. The qubits were realized with a set of polarized optical discrete waveguide modes. While the transmitter was utilized for preparing the encoded qubits of the quantum token state to be sent to the verifier's terminal, the receiver was used to apply quantum measurements to the arrival states either in the standard basis or in a different basis (i.e., Hadamard). Finally, an experimental setup is planned to provide a suitable quantum optical tokens environment using available fiber-coupled guided-wave optics components operating in telecommunication wavelengths to realize the proposed integrated photonic circuit.

3.3 Polarization Manipulation via Twisted Dielectric Waveguide

Polarization manipulations have always played an essential role in various photonic systems ranging from optical technologies such as telecommunication over spectroscopy and biosensing to quantum information encoding. Typically, manipulating the polarization state of light is realized in free-space utilizing conventional bulk optical waveplates. However, on-chip polarization controlling and manipulating using integrated waveguides are nontrivial and remain to be addressed. These applications were never demonstrated with a 3D optical waveguide structure immersed inside a glass having a weak RI contrast step between the core and the cladding.

Twisting optical geometries can provide more degrees of freedom in manipulating propagating light characteristics. In this work, I take advantage of the nature of EM wave propagation in optical waveguides [1, 2] and the novel method for femtosecond laser writing of optical glass waveguides [13] to allow the design of an on-chip waveguide type waveplate device. One can manipulate the polarization state of an optical guided-wave by utilizing a unique 3D integrated waveguide geometry - with a varying cross-section shape along the propagation direction of the light. The twisted waveguides were tested with monochromatic laser sources in both the NIR and visible regions to demonstrate the feasibility of polarization manipulation via a 3D laser-written waveguide in the weakly guiding regime that has a small index step. Parts of this section have been published in Ref. [13], where further details can be found.

3.3.1 Design of 3D Twisted Rectangular Guided-Wave Structure

The proposed device is a 3D dielectric waveguide with varying cross-sections and sizes along the optical axis, aiming to manipulate the polarization state of propagating light. The concept of the studied 3D optical waveguide structure geometry is depicted in the schematics of Fig. 30. A buried channel waveguide (a.k.a. wire waveguide) consists of a core and cladding; the waveguide core possesses a higher RI n_{core} and is buried in a lower RI n_{clad} medium so-called cladding. The unique 3D buried waveguide comprises three successive regions: a straight y-aligned rectangular waveguide region at the input, a twisted waveguide region at the middle with a rotated rectangular cross-section shape, and a straight x-aligned rectangular waveguide region at the output. While the twisting length of the middle region is l_{t}, each straight waveguide at the input/output has a length of l_{s}; thus, the total waveguide length is $l_{\mathrm{wg}} = l_{\mathrm{t}} + 2l_{\mathrm{s}}$. The z-axis (longitudinal direction) points along the optical axis of the propagating mode supported by the waveguide. The schematic of the inset in Fig. 30 shows the twisted waveguide core with smooth counterclockwise rotation by $\theta_{\mathrm{t}} = 90°$ along the propagation direction of the light directed to the optical axis. In particular, the rectangular cross-section shape at the input rotates around the z-axis by a twisting angle θ_{t} with respect to the xy plane at the input facet of the waveguide - where the y-aligned rectangular facet rotates 90° to become an x-aligned rectangular facet. The length of the twisted waveguide region required to achieve a certain twisting angle θ_{t} is denoted by the twisting length l_{t}.

Numerical simulators are essential in designing and developing SM and multimode optical waveguides with various complex cross-section geometries. A full-wave simulation of the studied single 3D rectangular waveguide can be handled well by the COMSOL Multiphysics platform based on the finite element analysis method; in the wave optics module utilizing the beam envelopes interface. The numerical model's computational domains consist of the waveguide structure geometry with $\theta_{\mathrm{t}} = 90°$, as shown in Fig. 30; the light propagates in the z-direction. Since the electric field in the cladding is decaying exponentially as a function of the distance from the core-cladding interface (detailed in section 2.1.1), considering large enough cladding - the field of confined modes has an extremely small value at the exterior boundaries (lower than -100 dB). Therefore, perfect electric conductor boundary conditions could be applied at the exterior boundaries of the y- and x- aligned rectangular straight waveguides (i.e., cladding boundaries).

In contrast, scattering boundary conditions can be used at the exterior boundaries of the twisted waveguide; to avoid back reflection of the outgoing wave from the exterior boundaries of the computational domains. Namely, these boundary conditions make the exterior boundaries transparent to the outgoing waves.

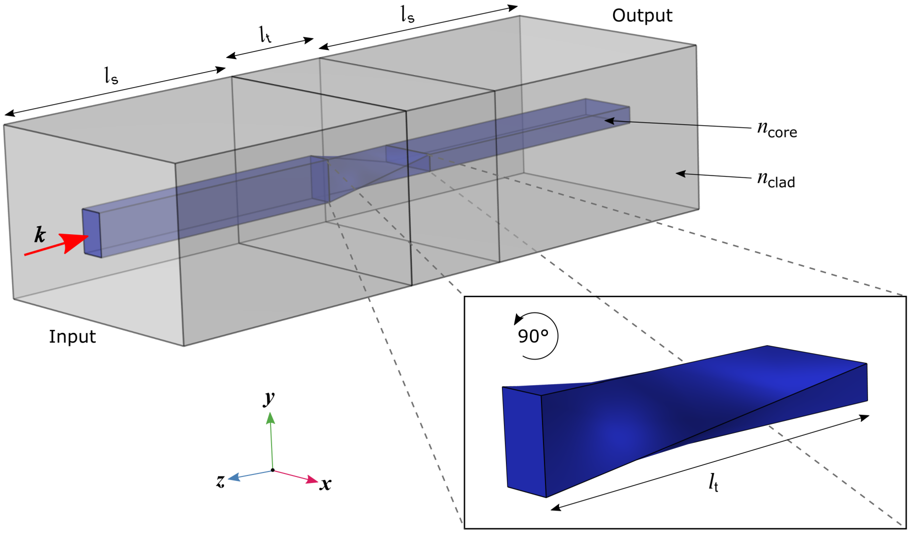

Figure 30 | The structure geometry of the studied twisted dielectric rectangular waveguide. 3D schematic representation of a single buried waveguide composed of a twisted waveguide region with a twisted length of l_t, sandwiched between two straight rectangular waveguide regions: y-aligned at the input and x-aligned at the output, each with the length of l_s. The single buried channel waveguide consists of a core (blue) with RI n_core and cladding (gray) with a lower RI n_clad. The wavevector $\boldsymbol{k}$ (red arrow) indicates the propagation direction of the light. The zoom-in shows the twisting waveguide core, at the middle waveguide region, with a smooth counterclockwise rotation by of 90° along its length in the z-direction.

Fabrication of complex 3D waveguide geometry, such as the studied unique twisted waveguide, can be achieved via the femtosecond-laser writing technique [142–144]. Due to the novel ability to finely control cross-section size along all transversal axes [13], waveguides with varied cross-section shapes and sizes along their length can be easily and efficiently created. The technique makes it possible to draw 3D optical waveguide paths inside transparent materials, generally using femtosecond laser pulses and multiphoton nonlinear effects to form the waveguide RI profile. Most femtosecond laser writing of optical-fiber-compatible glass waveguides are weakly guiding waveguides with a small index step, Δn, between the waveguide core and the cladding. The weak RI contrast (i.e.,the RI difference between the waveguide core and cladding $\Delta n = n_\mathrm{core} - n_\mathrm{clad}$) in the weak-guidance approximation follows $\Delta n / n_\mathrm{core} << 1$. In order to study and examine the 3D structure of the proposed waveguide configuration in optical glass, as shown in Fig. 30, laser-written waveguides were fabricated in borosilicate glass (Corning EAGLE 2000) samples by our collaborators. Comprehensive details about the fabrication of femtosecond direct laser-written waveguides in glass done by our collaborators are present in Ref. [13].

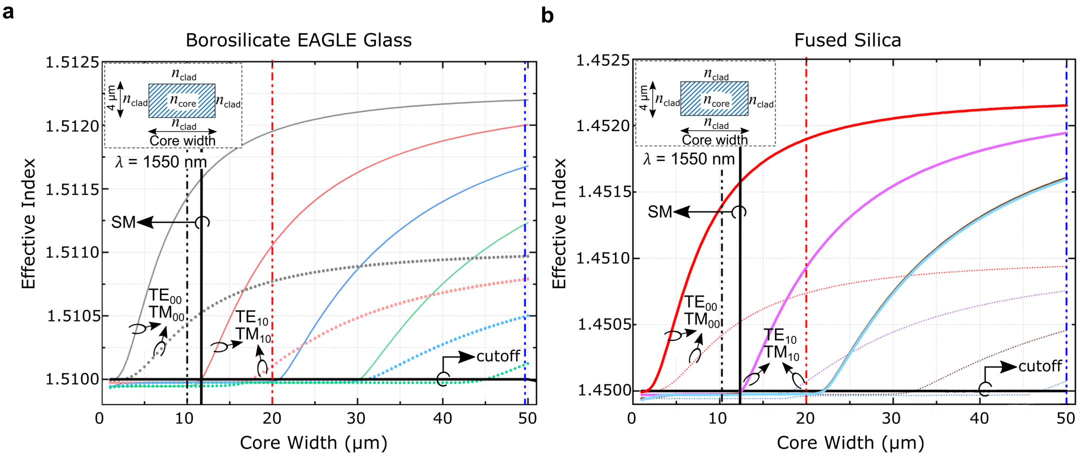

Figure 31 | Modal analysis of guided modes through SM and multimode waveguides. a-b, The calculated mode effective index as a function of the waveguide core width at a wavelength of 1550 nm for BK-7 glass (**a**) and fused silica glass (**b**) waveguides. The inset shows a schematic cross-section of the waveguide structure with a fixed waveguide core height of 4 µm. The solid black vertical lines indicate the upper bound of the SM region. The solid black horizontal lines indicate the cutoff of the modes, $n_{\text{eff}} > n_{\text{clad}}$. For BK-7 glass (**a**), the cladding RI is $n_{\text{clad}} = 1.51$, and consider waveguide core RI n_{core} between 1.513 (dashed curves) and 1.515 (solid curves). For fused silica glass (**b**), the cladding RI is $n_{\text{clad}} = 1.45$, and consider waveguide core RI n_{core} between 1.453 (dashed curves) and 1.455 (solid curves).

Two of the leading material platforms widely applied for the fabrication of photonic structures in transparent optical materials are fused silica glass (SiO_2) and borosilicate glass (BK-7). Empirical relationships between RI $n(\lambda)$ and wavelength can usually determine the dispersion of light in typical transparent media [129, 145]. Consider the telecommunication C-band to take advantage of the lower loss at a wavelength of 1550 nm commonly used in optical communication systems. If using a SiO_2 glass substrate, the RI of the cladding is $n_{\text{clad}} = 1.45$, whereas using a BK-7 glass substrate, the RI of the cladding is $n_{\text{clad}} = 1.51$. Since it is not always possible to accurately implement a particular RI change when creating such waveguides, the RI of the waveguide core needs to be evaluated for numerical modeling taking into account changes in the transparent medium due to the fabrication process [146–149]; particularly in cases where the waveguide design parameters are required before fabrication. These parameters can be estimated more accurately in future work by characterizing the RI profile of fabricated waveguides, as pointed out in Ref. [13]. Thus, a solid waveguide core RI was considered in the range $n_{\rm core} \sim [1.513, 1.515]$ for BK-7 glass and $n_{\rm core} \sim [1.453, 1.455]$ for SiO_2 glass to simplify modeling these waveguides before fabrication. It is worth mentioning that the actual RI profile of the fabricated waveguides is nontrivial, as observed in Fig. 2c in Ref. [13]. Therefore to further simplify the modeling of these waveguides, we used step-index approximation of the waveguide geometry. Namely, in the simulation, the waveguide core RI was considered uniform (i.e., solid core) and equal to the average of the actual RI in the core.

Before embarking into designing a rectangular waveguide where the light is confined in both transverse dimensions (i.e., the horizontal and vertical transversal directions), one can focus on a slab waveguide that confines the guided mode in a single transverse dimension to acquire a fundamental understanding of desired design parameters for optical waveguide. The mode properties of a waveguide are typically characterized in terms of a dimensionless normalized waveguide parameter. The normalized frequency (a.k.a. V number) of a step-index slab waveguide is given by:

$$V_{\rm c}^{m} = \frac{2\pi}{\lambda} d_{\rm h} \sqrt{n_{\rm core}^2 - n_{\rm clad}^2} \tag{3.10}$$

where $d_{\rm h}$ is the height of the waveguide core (a.k.a. the core thickness), λ is the vacuum wavelength, and $n_{\rm core}$ and $n_{\rm clad}$ denote the RI of the core and cladding, respectively. Symmetric slab waveguide's TE and TM modes have the same critical cutoff condition: $V_{\rm c}^{m} = m\pi$ for the $m^{\rm th}$ TE and TM modes. Because the fundamental mode (TE_0/TM_0) cutoff occurs at zero thickness ($V_{\rm c}^{0} = 0$), neither fundamental TE nor fundamental TM modes in a symmetric waveguide exhibit a cutoff. Thus, if the waveguide parameter is below $V_{\rm c}^{1} < \pi$, only the fundamental TE and TM modes can be supported by the waveguide. The waveguide core height was chosen as the optimal tradeoff between the compactness for easy fabrication and achieving only the first-order mode in the vertical direction of the designed waveguide; therefore, the waveguide thickness was fixed to 4 µm.

Proceeding further, a numerical mode analysis was employed to study the variations of the mode effective index with the width of the rectangular waveguide. That allows the designing of both SM and multimode waveguides. The waveguide core width dependency on the mode effective index $n_{\rm eff}$ at a wavelength of 1550 nm is shown in Fig. 31 for both material platforms. As seen from Eq. (2.1), confined modes are possible only when the waveguide core possesses the highest RI (i.e., $n_{\rm core} > n_{\rm clad}$) so that the guiding condition can be satisfied. Hence, the case of interest is when the mode effective index ranges between the RI of the core and cladding $n_{\mathrm{clad}} < n_{\mathrm{eff}} < n_{\mathrm{core}}$. In this case, the energy carried by these modes is confined to the vicinity of the waveguide core. Generally, higher effective index modes, where the fundamental mode has the highest effective index, are more tightly confined to the waveguide core and have more rapidly decaying evanescent tails (as detailed in section 2.1.1). The horizontal black solid lines in Fig. 31a-b represent the cutoff condition, $n_{\mathrm{eff}} > n_{\mathrm{clad}}$, where the modes having effective index below the cladding RI are not guided modes and refer to the radiation modes of the waveguide. In addition, designing SM or multimode waveguides is achievable by analyzing the mode effective index variations at a given wavelength and defining a desired waveguide core width. The black vertical lines in Fig. 31a-b indicate the SM operation regime (the left region from the line), which denotes the maximum value of the waveguide core width with a fixed core height of 4 µm - allowing the waveguide to support only the fundamental mode. In particular, the cutoff of the 2^{nd} order mode defines the upper bound of the SM region.

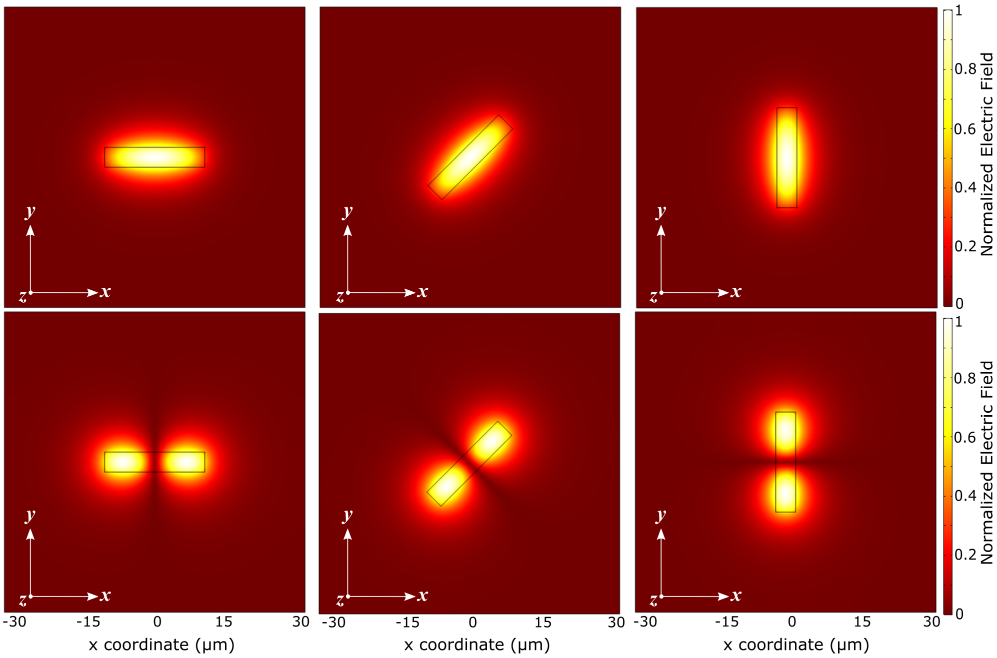

Figure 32 | Optical guided modes via the twisted rectangular waveguide structure. The simulated normalized mode intensity spatial profiles of the first two order modes supported by the waveguide at a wavelength of 1550 nm for different positions along the propagation direction of the light: at the input (right column), middle (middle column), and output (left column) of the twisted waveguide, with a twisting angle of ($\theta_{\mathrm{t}} = 90°$) and a twisted length of $l_{\mathrm{twist}} = 1.4$ mm. Each row corresponds to a different order mode: the fundamental (upper row) and the 2^{nd} order (bottom row) guided modes.

The specific design parameters of the SM and multimode twisted waveguides employed for the femtosecond laser-written fabrication are summarized in Table 3.2. These rectangular waveguides support a discrete number of guided modes which can be grouped into two families: quasi-TE (a.k.a. TE-like or E^x_{mn}) and quasi-TM (a.k.a. TM-like or E^y_{mn}). The sub-indices m and n (integers) indicate the number of crossings of each field component with the x-axis and y-axis inside the core, respectively. For a small RI step Δn between the waveguide core and cladding (i.e., under the weak guidance approximation $\Delta n/n_{\text{core}} << 1$), along with the symmetry of the transversal cross-section shape of the waveguide, the solution for the quasi-TE modes coincides with those of quasi-TM, as shown in Fig. 31. This behavior indicates that the TE/TM guided modes having the same order are almost degenerate. While degenerate modes have the same propagation constant value β, they are characterized by different polarization and other main field components. Thus, both the fundamental quasi-TE and the fundamental quasi-TM modes are involved in the SM region in which the cutoff of the 2$^{\text{nd}}$ order modes defines the upper bound. Based on the results shown in Fig.31, it is possible to design either a SM or a multitude waveguide supporting a particular number of modes by adjusting the waveguide core width. For instance, a SM waveguide can be achieved by configuring the cross-section sizes to 10 µm × 4 µm (represented by the black vertical dashed lines in Fig. 31). Conversely, by configuring the cross-section sizes to 20 µm × 4 µm (represented by the red vertical dashed lines in Fig. 31), the waveguide can support the 2$^{\text{nd}}$ order of TE and TM modes. In comparison, the waveguide can support the 4$^{\text{th}}$ order TE and TM modes by configuring the cross-section sizes to 50 µm × 4 µm (represented by the blue vertical dashed lines in Fig. 31). The twisted length of the waveguide was chosen to be the optimal tradeoff between the compactness to losses of the designed device. A parametric sweep was performed in the numerical model to allow modifying the twisted length value for choosing an appropriate length. The transmittance at shorter twisted lengths ($l_{\text{t}} < 0.65$ mm) decreases due to the rapid rotation of the waveguide shape and causes the scattering of light from all waveguide core boundaries. Conversely, as the twisted length increases from $l_{\text{t}} = 0.65$ mm to $l_{\text{t}} = 1$ mm, light scattering from the core boundaries decreases; consequently, the transmittance gradually increases. For twisted length in the range of $l_t > 1$ mm, the observed transmittance was maintained above 90%. Moreover, by adjusting the dimensions of the twisted waveguide, such as the twisted length and the total waveguide length, one can achieve optimal performance at desired wavelength(s), as pointed out in Ref. [13].

Table 3.2 | Design parameters of the twisted rectangular waveguides in borosilicate glass.

Waveguide Class	*Core cross section (μm)^2*	*Twisted Length (mm)*	*Fundamental mode n_{eff}*
Single-mode	4×10	1.4	1.51143
Multimode	4×20	1.4	1.51195

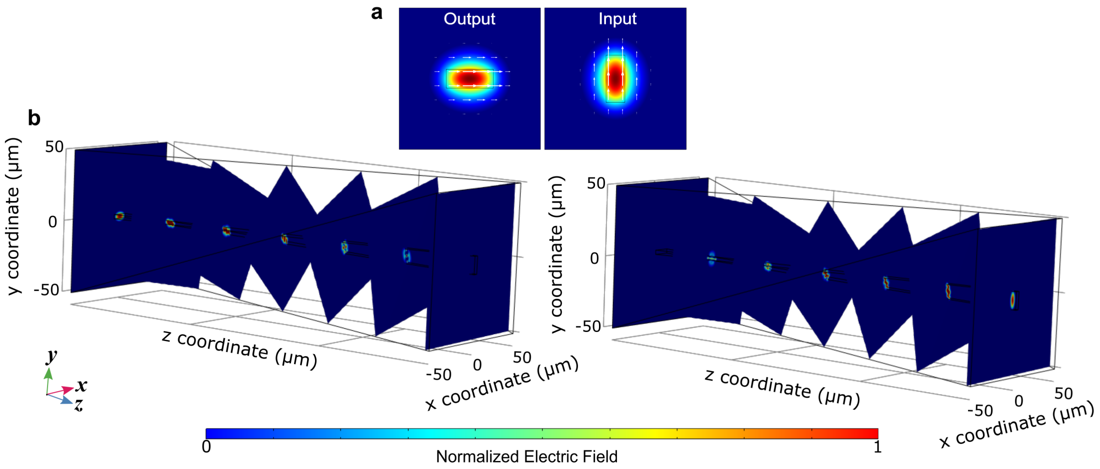

Figure 33 | Propagation dynamics of confined light via a twisted waveguide. a, Calculated normalized fundamental mode intensity profiles at the input and output of a 90° twisted waveguide at a wavelength of 1550 nm. The transversal cross-section sizes are 20 μm × 4 μm. **b,** Modal mode intensity profiles of the fundamental quasi-TE mode (right) for a twisted waveguide with a twisted length of 1.4 mm. The fundamental quasi-TM mode (left) evolution as it propagates via the twisted waveguide.

In order to search for the possibility of on-chip passive polarization manipulation of guided linear polarized light via a twisted waveguide, a waveguide having a 90° rotated rectangular shape was numerically simulated, as shown in Fig. 32 and Fig. 33. The light propagates along the waveguide, twisting uniformly along its optical axis with a twisted length of 1.4 mm and transversal cross-section sizes of 20 μm × 4 μm. A monochromatic TE polarized light was injected into the y-aligned rectangular facet of the twisted waveguide. As shown in Fig. 32, when monochromatic TE polarized light was injected from a y-aligned rectangular facet, the mode profiles obtained at the output of the waveguide were rotated 90° to become x-aligned. Moreover, when a fundamental quasi-TE polarized light was excited at the input of the twisted waveguide, a significant component of quasi-TM mode was observed at the output, as depicted at the bottom of Fig. 33. The modal analysis of the fundamental guided modes in the twisted waveguide exhibits that a twisted waveguide inside a glass configuration can achieve rectangular beam rotation. When light propagates along the waveguide, twisting uniformly along its optical axis, the optical guided modes shape experiences an adiabatic evolution, as pointed out in Ref. [13]. On the other hand, the polarization of the photons also changes as they travel through the twisted region, as evidenced by the fundamental quasi-TM mode evolution as it propagates via the twisted waveguide when the quasi-TE mode is excited at the input.

3.3.2 Experimental Evidence of On-Chip Polarization Manipulation

The twisted waveguides were fabricated using the new method for femtosecond laser writing of optical waveguides in transparent glass, as reported in Ref. [13]. The optical system was constructed in a cleanroom environment at the '*Light-on-a-Chip*' group, providing a controlled environment that minimizes the amount of background light to which the samples are exposed. In order to demonstrate the feasibility of waveguiding polarization manipulation, the twisted waveguide was tested using a polarization-controlled experimental setup - schematically shown in Fig. 34. The experimental measurements involved two different illuminations, allowing wavelength interrogation in two spectral regions, visible and NIR. Namely, the twisted waveguide was tested with linear polarized 637 nm and 1550 nm monochromatic laser sources. The two independent experimental measurements employed the sources of visible (iFLEX-iRIS CLM, Qioptiq Photonics) and NIR (KLS1550, Thorlabs). An optical SMF (P11550AFC, Thorlabs) connects the CW laser source to a protected silver reflective collimator (RC04FC-P01, Thorlabs). This type of achromatic collimator provides stable focus over a wide range of wavelengths. The collimated light passes through a polarizer (WP25M-UB, Thorlabs) followed by an iris to achieve 0°/90° linear polarization states of the light. Then, the beam was focused on the input waveguide facet using a $\times 40$ infinity-corrected imaging MO (RMS40X, Olympus). Namely, the coupling-in was performed via the focusing MO. The waveguide sample was mounted on a 4-axis piezoelectric stage (MBT402D, Thorlabs), allowing flexibility to adjust the incident light accurately to the waveguide input facet. A top view of the twisted waveguide was imaged for accurate inspection and characterization - using a stereo microscope (Stemi SV 6, ZEISS) and a camera (Axiocam, ZEISS) whose axis pointed perpendicularly to the twisted sample.

The transmitted light was collected from the output facet of the waveguide via a $\times 100$ MO (LD EC Epiplan-Neofluar, Zeiss), passed through a further polarizer and an iris, and directed to a 50:50 beam splitter (CCM1-BS015, Thorlabs) that splits the beam of light into two optical paths. Considering the polarization dependence of the BS (see Ref. [150]), an appropriate normalization was performed in the corresponding observed mode profile images. It is worth mentioning that the back focal point iris was placed to block the diffracted light from both the transparent sample and the optical system. Due to locating the waveguide one focal length away from the MO (4 mm), the transmitted optical signal from the waveguide can be imaged at infinity. Thus, the transmitted beam through the beam splitter was focused on a VIS-SWIR high-sensitivity imaging camera (NINOX 640 II, Photonics) using a lens (NBK-7 Plano-Convex, Thorlabs) with a focal length of 125 mm. The effective magnification of the MO is 75.76 due to the combining optical elements from different manufacturers. The dimensions of the camera sensor and the system magnification determine the dimensions of the sample area; then, the image area is 126.72 µm×101.24 µm. For the field intensity imaging of the optical mode of twisted waveguide, the camera was configured with fixed gain (0.001 dB) and exposure time (1.511 msec) to achieve optimal image brightness. In the case where the reference straight waveguide was tested, the camera configuration was preserved. Reconfiguring the camera would affect the image brightness, so the comparison between twisted and reference straight waveguides would be arbitrary or require appropriate normalization.

Concurrently with the imaging mode profiles of twisted and reference straight waveguides utilizing the camera, the reflected beam from the beam splitter was collected by an optical power meter. The two polarizers were placed before and after the waveguide sample and used for the polarization conversion measurement. Specifically, these polarizers were placed with relative angles of 0° and 90° to each other - to characterize the polarization-maintaining and the polarization conversion, respectively. When the polarizer transmission axis and input polarization are parallel (i.e., 0° relative angle), the transmission of a linearly polarized input is at its maximum. In contrast, the transmission is at its minimum by rotating the polarizer 90°, i.e., the transmission axis and input polarization are perpendicular. In addition, before the laser-written twisted- and reference straight-waveguides were characterized, an SMF was tested for the optical system calibration. The light emitted from SMF passed via the first polarizer, and the coupling-in was performed via the focusing MO. The SMF's transmission was measured by fine-tuning and aligning the optical elements in the system. When the optical power meter indicates zero counts, the relative angle between the transmission axis and injected linearly polarized light is 90°. However, when it indicates the maximum value, the relative angle between the transmission axis and injected linearly polarized light is 0°. Besides, the field intensity imaging of the guided mode supported by the typical SMF at a wavelength of 1550 nm was utilized to improve and reduce the imaging system's aberrations.

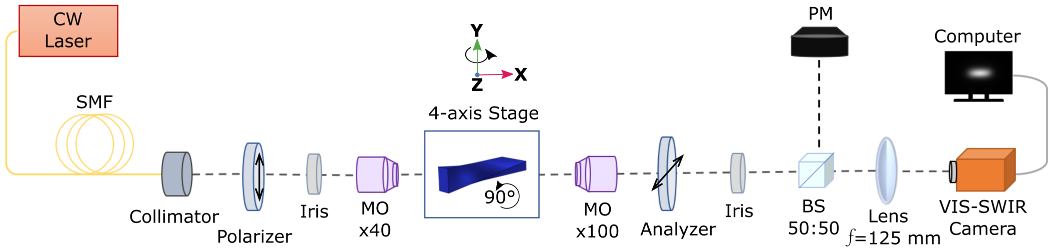

Figure 34 | Schematic diagram of the experimental setup for waveguide polarization measurements. Monochromatic light emitted from single-mode fiber (SMF) is collimated, linearly polarized, and then focused on the input waveguide facet. The transmitted light is collected from the output waveguide facet using a microscope objective (MO), passed through a polarizer, and split into two optical paths by a 50:50 beam splitter (BS). The reflected beam is directed to a digital optical power meter (PM). At the same time, the transmitted beam is focused on a VIS-SWIR camera.

In many cases, controlling the polarization state of the incident light is necessary, the same as required in the examined polarization-controlled experiments. A notable optical technique to couple light into an optical waveguide is starting with a beam in free-space and then using a lens to refocus the light onto the input facet of the tested waveguide. The full-wave simulation of the free-space SMF-to-waveguide coupling system was handled well by the COMSOL Multiphysics platform based on the finite element analysis method; in the wave optics module utilizing the beam envelopes interface. Fig. 35a shows the computational domains constructing the numerical model that properly represents the optical elements included in the coupling method used in the experimental setup (as depicted in Fig. 34). These include (from left to right) an SMF tip corresponding to the SMF connected to the laser source used in the experimental setup; two concave lenses placed in free-space between the fiber and waveguide analogous to the collimator and MO; and a waveguide tip corresponding to the fabricated laser-written waveguide. While the first lens was introduced to collimate the light emitted by the fiber, the second lens was placed to refocus the collimated light on the input facet of the waveguide. The spatial distribution of the normalized electric field at a wavelength of 1550 nm is shown in Fig. 35a when the lenses are placed at a position for minimum coupling loss. The SMF is placed at the back focal point of a lens resulting in a collimated beam at its output. When the light is output from the collimating lens, it converges slightly to that beam waist; then, the beam diverges at the same rate in the Rayleigh range (until the beam diameter continually increases). A converging beam (beam comes to a focus) is obtained when the light is output from the focusing lens - the beam diameter gradually decreases to that beam waist. The calculated transmittance and reflectance as a function of the focusing lens position at a wavelength of 1550 nm are shown in Fig. 35b. In addition, the transmittance and reflectance wavelength dependence is shown in 35c when the lenses are placed for minimum losses. One can see that the coupling loss is minimized (and as a result, the transmittance is maximized) - when the lenses shifted 5 µm closer to the waveguide tip and SMF end than the ideal focal length of the lenses. Namely, the collimating lens position is modified by 5 µm closer to the SMF tip, whereas the focusing lens is shifted closer to the waveguide tip with the same distance. The appropriate positions of the lenses allow more energy to couple into the waveguide.

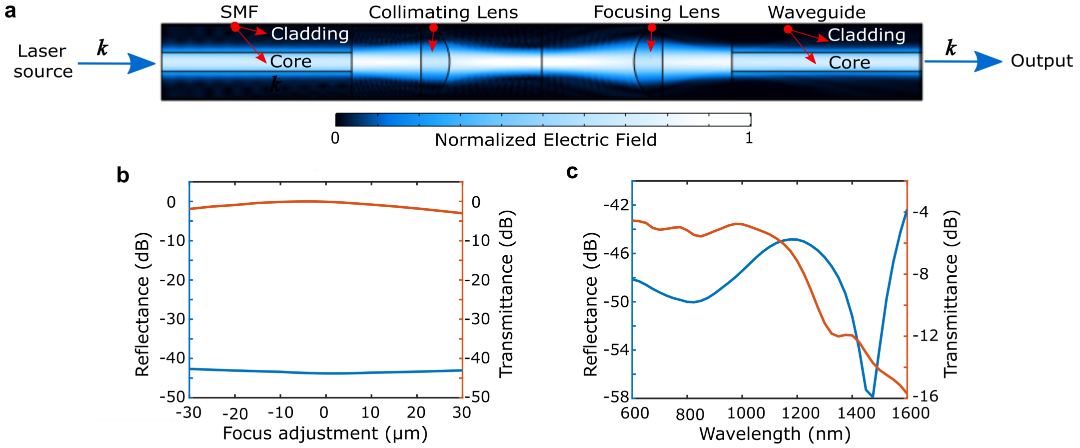

Figure 35 | Numerical simulation for the free-space SMF to waveguide coupling system. a, Visualization of the end-to-end expanded beam coupling system shows the normalized electric field distribution at a wavelength of 1550 nm. In order to achieve minimum optical losses, the lenses are placed in the optimal position between a single-mode fiber (SMF) -end and the waveguide tip. The wavevector $\boldsymbol{k}$ (blue arrows) indicates the propagation direction of the light. **b-c,** The dependent of the focusing lens position (**b**) and wavelength (**c**) on the transmittance (orange) and reflectance (blue) for optimizing the coupling efficiency.

In order to assess the possibility of on-chip passive polarization manipulation of guided linear polarized light via a twisted waveguide, polarization-controlled experiments were carried out for both twisted and reference straight waveguides. The laser-written waveguides were tested with linearly polarized light; emitted from either 637 nm or 1550 nm monochromatic laser sources. Fig. 36 shows the experimental results indicating the capability and feasibility of polarization state manipulation of the guided light via a twisted waveguide with a $\theta_\mathrm{t} = 90°$ twisting angle and twisted length of $l_\mathrm{t} = 1.4$ mm. Both twisted and straight waveguides have cross-section dimensions of 20 µm × 4 µm and a total length of 10 mm. The results show that the designed twisted dielectric waveguide enables the polarization state rotation of linearly polarized laser light during its transmission via the twisted region. Concurrently with these results, a twisted dielectric waveguide with a rotated rectangular transversal cross-section shape enables on-chip rectangular beam rotation of transmitted laser light at both tested wavelengths. As shown in Fig. 36a-b, a higher-order mode was observed for guided laser light at 637 nm, whereas the fundamental mode was observed for guided laser light at 1550 nm.

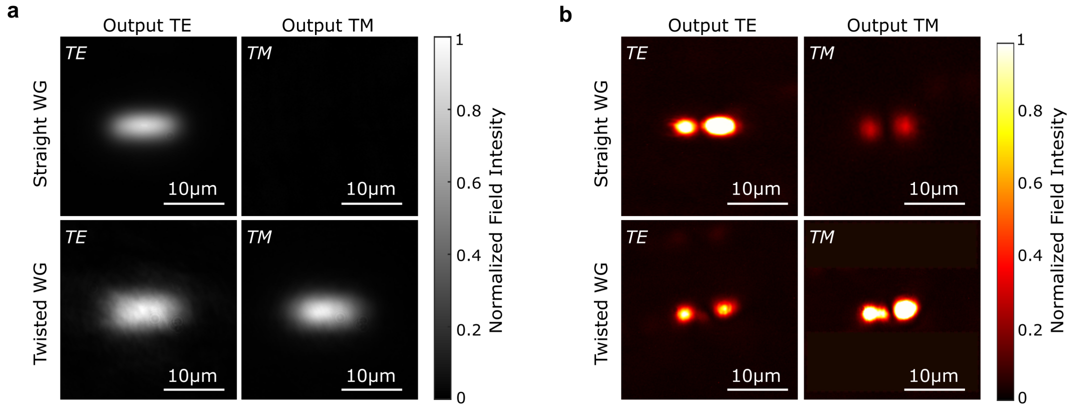

Figure 36 | Experimental results of on-chip polarization manipulation via a twisted rectangular waveguide buried inside a transparent glass. a-b, Polarization-controlled measurements for straight waveguide (top) and 90° twisted waveguide (bottom) with 1.4 mm twisted length. Both waveguides have cross-sections of 20 μm × 4 μm and a total length of 10 mm. Imaging guided mode profiles obtained from the buried waveguides facet for a particular output polarization state (TE/TM); when monochromatic TE polarized laser light incident upon the waveguides input facet at wavelengths of 1550 nm (**a**) and 637 nm (**b**).

When light propagates along the waveguide, twisting uniformly along its optical axis, the optical guided modes shape experiences an adiabatic evolution. On the other hand, the polarization of the photons also changes as they travel through the twisted region. The comparison between the twisted and reference straight waveguides for both the 637 nm laser and 1550 nm laser is shown in Fig. 36a-b. As seen in the obtained mode image profiles, the straight waveguide maintained the same polarization state of guided laser light at 1550 nm. On the other hand, the twisted waveguide could convert the polarization state with an efficiency of nearly 43%. When monochromatic TE polarized light was injected into the twisted waveguide, significant power in TM mode was observed at the output, as depicted in the bottom images of Fig. 36a. However, the power in the TM output mode was slightly lower than in the TE mode supported by the twisted waveguide. The results for the twisted waveguide with 1550 nm laser show good correspondence with results with 637 nm laser - significant power in TM mode was observed at the output, as depicted in the bottom images of Fig. 36b. The power in the TM output mode was slightly higher than in the TE mode supported by the twisted waveguide. The proposed 90° twisted waveguide can be generalized to implement an arbitrary rotation of the guided modes supported by the waveguide - by adjusting its twisting angle and RI contrast between the waveguide core and the surrounding medium [13]. In addition, by adjusting the design dimensions of the twisted waveguide (e.g., twisted length, total waveguide length, twisting angle, etc.), one can achieve optimal performance at desired wavelength(s), as pointed out in Ref. [13].

CHAPTER 4

Conclusion

The main aim of the research activity in the present thesis was to investigate novel on-chip configurations for unique functionalities. The major contributions of this research include:

- **MXene-based all-optical nonlinear AF for photonics-based deep structured learning.** Two independent all-optical nonlinear AF configurations were numerically explored and experimentally demonstrated via fabricated $Ti_3C_2T_x$ MXene thin films and MXene overlayers on an optical waveguide. This allowed to achieve all-optical nonlinear transform functions via the devices' optical responses in the cases of: 1) evanescent excitation, and 2) free-space illumination. Photonics deep structured learning emulation showed compatible performance of the studied all-optical activation mechanisms, in terms of accuracy and loss as a function of epoch with respect to the well-established and commonly used nonlinear AFs in deep-learning applications. A similar concept utilizing the studied nonlinear AFs can be applied to implement numerous machine learning applications and other complex tasks. The MXene-based all-optical nonlinear AF demonstrated in this work may open the door to the MXene-platform development of efficient and high-speed optical computation for photonic NNs.

- **On-chip classically verifiable photonic quantum money.** A chip-to-chip system based on a set of optical discrete waveguide modes and fundamental guided-wave optics building blocks has been proposed and demonstrated for the feasibility of preparing and verifying quantum photonic tokens. Whether QM with optical guided-wave modes can be realized in practice remains to be verified by experiments with the possibility of near-future implementations of quantum memories. However, the presented scheme can also pave the way for other practical notions, such as quantum message authentication code. It may also open new perspectives for implementing other desired quantum cryptography and quantum information applications.

- **Twisted dielectric waveguide for on-chip polarization manipulation.** A 3D laser-written waveguide structure immersed inside a transparent glass, with a weak RI contrast, was explored to manipulate the polarization state of the propagating light. The polarization of the photons traveling along the twisted waveguide region gradually transforms during their transmission via the 90° twisted rectangular waveguided core. By adjusting the design parameters of the twisted waveguide, a similar concept can be applied to realize a waveguide-type rotated waveplate - that achieves optimal polarization conversion efficiency at desired wavelengths across wide bands, from visible to NIR regions.

CHAPTER 5

Future Scope and Perspectives on Studied Topics

Having presented my studies' results, demonstrated and analyzed my findings, and summarized the thesis through the preceding chapters, I would like to propose the following ideas for possible future studies in the field of integrated photonics architectures for efficient light manipulation on a chip. The major future directions in the fields of this research may include:

∫ **Photonic-based deep structured learning.**

- Many deep structured learning models have used the *Softmax* function at the final hidden layer before the output layer. Even so, a photonic *Softmax* realization has not been placed. In particular, the *Softmax* function is used to transform the incoming input values z_j (j=1,2...n), generated at the i^{th} neuron with k neurons in the layer, to probabilities distribution follows: $f_i(X_{\text{OIU}}) = e^{X^{\text{OIU}}{}_i}/(\sum_{j=1}^{k} e^{X^{\text{OIU}}{}_j})$. Namely, the remainders receive a much lower value when one input receives a high value (i.e., proportional to the exponentials). Therefore, my idea for *Softmax* optical implementation is based on integrated photonic circuit combined mesh of photonic combiners, and all-optical nonlinear AF similar to the one proposed in this study. By passing the output of an individual neuron through elu-like AF, one can implement the function's numerator. In the same way for all the other neurons output and mesh of optical combiners to sum these signals, one can implement the function's denominator. Thus, the results of subtracting these two measured optical signals can be achieved by applying the logarithmic functionality.
- Advancements in deep learning applications include huge datasets and complex calculation models, which require considerable computational resources and a long processing

time for the training phases to reach their stage of being applicable. Hence, slow backpropagation and large energy consumption limit the advances of photonic deep structured learning applications. Since photonic-based NNs exhibit novel computational approaches, they also enable unique methods for training their parameters (i.e., weights optimizing). Therefore, developing and experimentally demonstrating novel methods for training these models is demanded. While there have been individual demonstrations of directly obtaining the parameters' gradient by employing forward propagation phases and the finite difference method [87], gradients computation via in situ intensity measurements and adjoint variable method [151], and the neuroevolution technique [152] in self-learn the weights of photonic-based NNs, practically and efficiently realization for training the all-optical deep structured learning architectures still remains an open challenge in realistic use cases.

- In order to be scaled the photonic deep structured learning approaches for large-scale deployment, both high and low levels of system design are required. To this end, a new processing platform of photonic chip-level that incorporates approaches of both EM simulations and photonic NN model emulations must be suggested. Namely, a comprehensive hybrid system of tools and resources that can simulate an optical NN considering the light-matter interactions in different elemental devices of the model to create accurate computations. These include verification techniques to modify the NN model's parameters and the actual physical devices' characteristics. Achieving this goal may open the door for pushing the state-of-the-art photonic-based deep structured learning applications to develop various future complex models efficiently.

∫ **On-chip quantum money as quantum token.**

- The vital missing ingredient for realistic use cases of numerous quantum communications and quantum computing applications and to advance many quantum systems is quantum memory that can store the photons' quantum state and reproduce it on demand. Currently, media-based (e.g., atoms, molecules, and others) is the most promising physical approach to the realization of state-of-the-art of quantum memories. These approaches' mechanisms are characterized by either optically controlled or external electric or magnetic field adjustments. These approaches' mechanisms are characterized by either optically controlled or external electric or magnetic field adjustments. Considering the availability of numerous MXenes with a wide range of chemical characteristics which provide a broad range of EM properties and optical properties covering the wavelength from UV to IR, MXenes are the first choice for several applications from EO devices through plasmonics applications to energy storage. But, can the MXenes family also provide a suitable platform for the future generation of quantum memory devices?

- Besides the fact that qubits can be realized by utilizing the first order of TE- and TM-polarized guided modes, as proposed in this work, polarization diversity systems can also be used for both holder chip and verifier terminal chip. A similar concept can be applied to encoded different orders of waveguide modes as qubits for one polarization only (instead of both TE and TM modes). This requires multimode waveguide construction with mode multiplexer/demultiplexer, which might be carried out via a parallel mode coupler with two different waveguide widths. Developing various quantum functionalities with guided-wave optics may open new perspectives for practical quantum cryptography and quantum information applications.

References

1. Okamoto, K. *Fundamentals of optical waveguides* (Elsevier, 2021).
2. Born, M. & Wolf, E. *Principles of optics: electromagnetic theory of propagation, interference and diffraction of light* (Elsevier, 2013).
3. Ostrowsky, D. B. & Reinisch, R. *Guided wave nonlinear Optics* (Springer Science & Business Media, 2012).
4. Boyd, R. W. *Nonlinear optics* (Academic Press, 2020).
5. Meng, Y. *et al.* Optical meta-waveguides for integrated photonics and beyond. *Light: Science & Applications* **10,** 1–44 (2021).
6. Khodadadi, M., Nozhat, N. & Moshiri, S. M. M. Theoretical analysis of a circular hybrid plasmonic waveguide to design a hybrid plasmonic nano-antenna. *Scientific reports* **10,** 1–17 (2020).
7. Gangaraj, S. A. H., Jin, B., Argyropoulos, C. & Monticone, F. Broadband field enhancement and giant nonlinear effects in terminated unidirectional plasmonic waveguides. *Physical Review Applied* **14,** 054061 (2020).
8. Hunsperger, R. G. *Integrated optics* (Springer, 1995).
9. Prasad, S., Schumacher, H. & Gopinath, A. *High-speed electronics and optoelectronics: devices and circuits* (Cambridge University Press, 2009).
10. Weber, M. J. *Handbook of optical materials* (CRC press, 2018).
11. Pal, B. P. *Guided wave optical components and devices: basics, technology, and applications* (Academic press, 2010).
12. Bhadra, S. & Ghatak, A. *Guided Wave Optics and Photonic Devices* (CRC Press, 2017).
13. Sun, B. *et al.* On-chip beam rotators, adiabatic mode converters, and waveplates through low-loss waveguides with variable cross-sections. *Light: Science & Applications* **11,** 1–15 (2022).

14. Hazan, A. *et al.* MXene Nanoflakes Enabled All-Optical Nonlinear Activation Function for On-Chip Photonic Deep Neural Networks. *Advanced Materials,* 2210216 (2023).
15. Karabchevsky, A., Katiyi, A., Ang, A. S. & Hazan, A. On-chip nanophotonics and future challenges. *Nanophotonics* **9,** 3733–3753 (2020).
16. Karabchevsky, A., Hazan, A. & Dubavik, A. All-Optical Polarization-Controlled Nanosensor Switch Based on Guided-Wave Surface Plasmon Resonance via Molecular Overtone Excitations in the Near-Infrared. *Advanced Optical Materials,* 2000769 (2020).
17. Hegde, R. S. Deep learning: a new tool for photonic nanostructure design. *Nanoscale Advances* **2,** 1007–1023 (2020).
18. Tahersima, M. H. *et al.* Deep neural network inverse design of integrated photonic power splitters. *Scientific Reports* **9,** 1–9 (2019).
19. Liu, D., Tan, Y., Khoram, E. & Yu, Z. Training deep neural networks for the inverse design of nanophotonic structures. *ACS Photonics* **5,** 1365–1369 (2018).
20. Sajedian, I., Kim, J. & Rho, J. Finding the optical properties of plasmonic structures by image processing using a combination of convolutional neural networks and recurrent neural networks. *Microsystems & Nanoengineering* **5,** 1–8 (2019).
21. Qian, C. *et al.* Deep-learning-enabled self-adaptive microwave cloak without human intervention. *Nature Photonics* **14,** 383–390 (2020).
22. Shastri, B. J. *et al.* Photonics for artificial intelligence and neuromorphic computing. *Nature Photonics* **15,** 102–114 (2021).
23. Grant-Jacob, J. A. *et al.* Fibre-optic based particle sensing via deep learning. *Journal of Physics: Photonics* **1,** 044004 (2019).
24. Kornienko, V. V. *et al.* Machine learning for optical gas sensing: a leaky-mode humidity sensor as example. *IEEE Sensors Journal* **20,** 6954–6963 (2020).
25. Amin, M. J. & Riza, N. Machine learning enhanced optical distance sensor. *Optics Communications* **407,** 262–270 (2018).
26. Strack, R. Deep learning advances super-resolution imaging. *Nature methods* **15,** 403–403 (2018).
27. Fang, L. *et al.* Deep learning-based point-scanning super-resolution imaging. *Nature Methods* **18,** 406–416 (2021).

28. Zhang, Q., Yu, H., Barbiero, M., Wang, B. & Gu, M. Artificial neural networks enabled by nanophotonics. *Light: Science & Applications* **8,** 1–14 (2019).

29. Pei, L. *et al.* Key Technologies of Photonic Artificial Intelligence Chip Structure and Algorithm. *Applied Sciences* **11,** 5719 (2021).

30. Xiang, C. *et al.* High-performance lasers for fully integrated silicon nitride photonics. *Nature communications* **12,** 1–8 (2021).

31. Liu, J. *et al.* Research progress in optical neural networks: theory, applications and developments. *PhotoniX* **2,** 1–39 (2021).

32. Demertzis, K., Papadopoulos, G. D., Iliadis, L. & Magafas, L. A Comprehensive Survey on Nanophotonic Neural Networks: Architectures, Training Methods, Optimization, and Activations Functions. *Sensors* **22,** 720 (2022).

33. Dong, Y. *et al.* Saturable absorption in 2D Ti_3C_2 MXene thin films for passive photonic diodes. *Advanced Materials* **30,** 1705714 (2018).

34. Jhon, Y. I. *et al.* Metallic MXene saturable absorber for femtosecond mode-locked lasers. *Advanced Materials* **29,** 1702496 (2017).

35. Wang, G. *et al.* Two-photon absorption in monolayer MXenes. *Advanced Optical Materials* **8,** 1902021 (2020).

36. Maleski, K., Shuck, C. E., Fafarman, A. T. & Gogotsi, Y. The Broad Chromatic Range of Two-Dimensional Transition Metal Carbides. *Advanced Optical Materials* **9,** 2001563 (2021).

37. Chaudhuri, K. *et al.* Highly broadband absorber using plasmonic titanium carbide (MXene). *ACS Photonics* **5,** 1115–1122 (2018).

38. Wiesner, S. Conjugate coding. *ACM Sigact News* **15,** 78–88 (1983).

39. Wootters, W. K. & Zurek, W. H. A single quantum cannot be cloned. *Nature* **299,** 802–803 (1982).

40. Pastawski, F., Yao, N. Y., Jiang, L., Lukin, M. D. & Cirac, J. I. Unforgeable noise-tolerant quantum tokens. *Proceedings of the National Academy of Sciences* **109,** 16079–16082 (2012).

41. Ma, L., Slattery, O. & Tang, X. Optical quantum memory and its applications in quantum communication systems. *Journal of Research of the National Institute of Standards and Technology* **125** (2020).

42. Lvovsky, A. I., Sanders, B. C. & Tittel, W. Optical quantum memory. *Nature photonics* **3,** 706–714 (2009).

43. Bartkiewicz, K. *et al.* Experimental quantum forgery of quantum optical money. *npj Quantum Information* **3,** 1–8 (2017).

44. Jiráková, K., Bartkiewicz, K., Černoch, A. & Lemr, K. Experimentally attacking quantum money schemes based on quantum retrieval games. *Scientific Reports* **9,** 1–9 (2019).

45. Kent, A., Lowndes, D., Pitalúa-García, D. & Rarity, J. Practical quantum tokens without quantum memories and experimental tests. *npj Quantum Information* **8,** 1–14 (2022).

46. Bozzio, M. *et al.* Experimental investigation of practical unforgeable quantum money. *npj Quantum Information* **4,** 1–8 (2018).

47. Guan, J.-Y. *et al.* Experimental preparation and verification of quantum money. *Physical Review A* **97,** 032338 (2018).

48. Bozzio, M., Diamanti, E. & Grosshans, F. Semi-device-independent quantum money with coherent states. *Physical Review A* **99,** 022336 (2019).

49. Dušek, M., Jahma, M. & Lütkenhaus, N. Unambiguous state discrimination in quantum cryptography with weak coherent states. *Physical Review A* **62,** 022306 (2000).

50. Amiri, R. & Arrazola, J. M. Quantum money with nearly optimal error tolerance. *Physical Review A* **95,** 062334 (2017).

51. Aaronson, S. & Christiano, P. *Quantum money from hidden subspaces* in *Proceedings of the forty-fourth annual ACM symposium on Theory of computing* (2012), 41–60.

52. Ben-David, S. & Sattath, O. Quantum tokens for digital signatures. *arXiv preprint arXiv: 1609.09047* (2016).

53. Behera, A., Sattath, O. & Shinar, U. Noise-tolerant quantum tokens for mac. *arXiv preprint arXiv:2105.05016* (2021).

54. Yaman, F. *et al.* 10 x 112Gb/s PDM-QPSK transmission over 5032 km in few-mode fibers. *Optics Express* **18,** 21342–21349 (2010).

55. Berova, N., Nakanishi, K. & Woody, R. W. *Circular dichroism: principles and applications* (John Wiley & Sons, 2000).

56. Tang, Y. & Cohen, A. E. Enhanced enantioselectivity in excitation of chiral molecules by superchiral light. *Science* **332,** 333–336 (2011).

57. Tyo, J. S., Goldstein, D. L., Chenault, D. B. & Shaw, J. A. Review of passive imaging polarimetry for remote sensing applications. *Applied optics* **45,** 5453–5469 (2006).

58. Gündoğan, M., Ledingham, P. M., Almasi, A., Cristiani, M. & De Riedmatten, H. Quantum storage of a photonic polarization qubit in a solid. *Physical review letters* **108,** 190504 (2012).

59. Ma, X.-S. *et al.* Quantum teleportation over 143 kilometres using active feed-forward. *Nature* **489,** 269–273 (2012).

60. Chen, R.-P., Chen, Z., Gao, Y., Ding, J. & He, S. Flexible manipulation of the polarization conversions in a structured vector field in free space. *Laser & Photonics Reviews* **11,** 1700165 (2017).

61. Lyu, Z. & Wang, C. All-optically phase-induced polarization modulation by means of holographic method. *Scientific Reports* **10,** 1–11 (2020).

62. Nicholls, L. H. *et al.* Ultrafast synthesis and switching of light polarization in nonlinear anisotropic metamaterials. *Nature Photonics* **11,** 628–633 (2017).

63. Kim, Y. *et al.* Demonstration of integrated polarization rotator based on an asymmetric silicon waveguide with a trench. *Journal of Optics* **18,** 095801 (2016).

64. An, S. & Kwon, O.-K. Integrated InP polarization rotator using the plasmonic effect. *Optics Express* **26,** 1305–1314 (2018).

65. Hou, Z.-S. *et al.* On-Chip Polarization Rotators. *Advanced Optical Materials* **7,** 1900129 (2019).

66. Schumann, M., Bückmann, T., Gruhler, N., Wegener, M. & Pernice, W. Hybrid 2D–3D optical devices for integrated optics by direct laser writing. *Light: Science & Applications* **3,** e175–e175 (2014).

67. Corrielli, G. *et al.* Rotated waveplates in integrated waveguide optics. *Nature Communications* **5,** 1–6 (2014).

68. Matsuda, N. *et al.* A monolithically integrated polarization entangled photon pair source on a silicon chip. *Scientific Reports* **2,** 1–7 (2012).

69. Chrostowski, L. & Hochberg, M. *Silicon photonics design: from devices to systems* (Cambridge University Press, 2015).

70. Snyder, A. W. & Love, J. *Optical waveguide theory* (Springer Science & Business Media, 2012).

71. Taylor, H. F. & Yariv, A. Guided wave optics. *Proceedings of the IEEE* **62,** 1044–1060 (1974).

72. Katiyi, A. & Karabchevsky, A. Figure of merit of all-dielectric waveguide structures for absorption overtone spectroscopy. *Journal of Lightwave Technology* **35,** 2902–2908 (2017).

73. Selvaraja, S. K. & Sethi, P. Review on optical waveguides. *Emerging Waveguide Technology* **95** (2018).

74. COMSOL, I. *COMSOL Multiphysics.* https://www.comsol.com/.

75. Nicolet, A., Zolla, F. & Guenneau, S. Modelling of twisted optical waveguides with edge elements. *The European Physical Journal Applied Physics* **28,** 153–157 (2004).

76. Napiorkowski, M. & Urbanczyk, W. Rigorous modeling of twisted anisotropic optical fibers with transformation optics formalism. *Optics Express* **29,** 15199–15216 (2021).

77. Shyroki, D. M. Exact equivalent straight waveguide model for bent and twisted waveguides. *IEEE Transactions on microwave theory and techniques* **56,** 414–419 (2008).

78. Azzam, S. I. & Kildishev, A. V. Time-domain dynamics of saturation of absorption using multilevel atomic systems. *Optical Materials Express* **8,** 3829–3834 (2018).

79. Yamashita, S. Nonlinear optics in carbon nanotube, graphene, and related 2D materials. *APL Photonics* **4,** 034301 (2019).

80. Autere, A. *et al.* Nonlinear optics with 2D layered materials. *Advanced Materials* **30,** 1705963 (2018).

81. Wu, Q. *et al.* MXene-based saturable absorber for femtosecond mode-locked fiber lasers. *Optics Express* **27,** 10159–10170 (2019).

82. Jhon, Y. I., Jhon, Y. M. & Lee, J. H. Nonlinear optics of MXene in laser technologies. *Journal of Physics: Materials* **3,** 032004 (2020).

83. Waldrop, M. M. The chips are down for Moore's law. *Nature News* **530,** 144 (2016).

84. Chiles, J., Buckley, S. M., Nam, S. W., Mirin, R. P. & Shainline, J. M. Design, fabrication, and metrology of 10× 100 multi-planar integrated photonic routing manifolds for neural networks. *APL Photonics* **3,** 106101 (2018).

85. Carolan, J. *et al.* Universal linear optics. *Science* **349,** 711–716 (2015).

86. Tait, A. N. *et al.* Microring weight banks. *IEEE Journal of Selected Topics in Quantum Electronics* **22,** 312–325 (2016).

87. Shen, Y. *et al.* Deep learning with coherent nanophotonic circuits. *Nature Photonics* **11,** 441–446 (2017).

88. Zhang, H. *et al.* An optical neural chip for implementing complex-valued neural network. *Nature Communications* **12,** 1–11 (2021).

89. Reck, M., Zeilinger, A., Bernstein, H. J. & Bertani, P. Experimental realization of any discrete unitary operator. *Physical Review Letters* **73,** 58 (1994).

90. Feldmann, J., Youngblood, N., Wright, C. D., Bhaskaran, H. & Pernice, W. H. All-optical spiking neurosynaptic networks with self-learning capabilities. *Nature* **569,** 208–214 (2019).

91. Tait, A. N., Nahmias, M. A., Shastri, B. J. & Prucnal, P. R. Broadcast and weight: an integrated network for scalable photonic spike processing. *Journal of Lightwave Technology* **32,** 4029–4041 (2014).

92. Lin, X. *et al.* All-optical machine learning using diffractive deep neural networks. *Science* **361,** 1004–1008 (2018).

93. Luo, Y. *et al.* Design of task-specific optical systems using broadband diffractive neural networks. *Light: Science & Applications* **8,** 1–14 (2019).

94. Giambagli, L., Buffoni, L., Carletti, T., Nocentini, W. & Fanelli, D. Machine learning in spectral domain. *Nature Communications* **12,** 1–9 (2021).

95. Li, J. *et al.* Spectrally encoded single-pixel machine vision using diffractive networks. *Science Advances* **7,** eabd7690 (2021).

96. Xu, X. *et al.* 11 TOPS photonic convolutional accelerator for optical neural networks. *Nature* **589,** 44–51 (2021).

97. Chang, J., Sitzmann, V., Dun, X., Heidrich, W. & Wetzstein, G. Hybrid optical-electronic convolutional neural networks with optimized diffractive optics for image classification. *Scientific reports* **8,** 1–10 (2018).

98. Xu, X., Zhu, L., Zhuang, W., Lu, L. & Yuan, P. *A Convolution Neural Network Implemented by Three 3× 3 Photonic Integrated Reconfigurable Linear Processors* in *Photonics* **9** (2022), 80.

99. Mehrabian, A., Al-Kabani, Y., Sorger, V. J. & El-Ghazawi, T. *PCNNA: A photonic convolutional neural network accelerator* in *2018 31st IEEE International System-on-Chip Conference (SOCC)* (2018), 169–173.

100. Nakajima, M., Tanaka, K. & Hashimoto, T. Scalable reservoir computing on coherent linear photonic processor. *Communications Physics* **4,** 1–12 (2021).

101. Zhou, T. *et al.* Large-scale neuromorphic optoelectronic computing with a reconfigurable diffractive processing unit. *Nature Photonics* **15,** 367–373 (2021).

102. Williamson, I. A. *et al.* Reprogrammable electro-optic nonlinear activation functions for optical neural networks. *IEEE Journal of Selected Topics in Quantum Electronics* **26,** 1–12 (2019).

103. Jha, A., Huang, C. & Prucnal, P. R. Reconfigurable all-optical nonlinear activation functions for neuromorphic photonics. *Optics Letters* **45,** 4819–4822 (2020).

104. De Lima, T. F. *et al.* Noise analysis of photonic modulator neurons. *IEEE Journal of Selected Topics in Quantum Electronics* **26,** 1–9 (2019).

105. Amin, R. *et al.* ITO-based electro-absorption modulator for photonic neural activation function. *APL Materials* **7,** 081112 (2019).

106. Mourgias-Alexandris, G. *et al.* An all-optical neuron with sigmoid activation function. *Optics express* **27,** 9620–9630 (2019).

107. Hill, M. T., Frietman, E. E., de Waardt, H., Khoe, G.-d. & Dorren, H. J. All fiber-optic neural network using coupled SOA based ring lasers. *IEEE Transactions on Neural Networks* **13,** 1504–1513 (2002).

108. Miscuglio, M. *et al.* All-optical nonlinear activation function for photonic neural networks. *Optical Materials Express* **8,** 3851–3863 (2018).

109. Zuo, Y. *et al.* All-optical neural network with nonlinear activation functions. *Optica* **6,** 1132–1137 (2019).

110. Rasmussen, T. S., Yu, Y. & Mork, J. All-optical non-linear activation function for neuromorphic photonic computing using semiconductor Fano lasers. *Optics Letters* **45,** 3844–3847 (2020).

111. Gisin, N., Ribordy, G., Tittel, W. & Zbinden, H. Quantum cryptography. *Reviews of modern physics* **74,** 145 (2002).

112. Krovi, H. Models of optical quantum computing. *Nanophotonics* **6,** 531–541 (2017).

113. O'brien, J. L. Optical quantum computing. *Science* **318,** 1567–1570 (2007).

114. O'brien, J. L., Furusawa, A. & Vučković, J. Photonic quantum technologies. *Nature Photonics* **3,** 687–695 (2009).

115. Mohanty, A. *et al.* Quantum interference between transverse spatial waveguide modes. *Nature communications* **8,** 1–7 (2017).

116. Sibson, P. *et al.* Chip-based quantum key distribution. *Nature communications* **8,** 1–6 (2017).

117. Gavinsky, D. *Quantum money with classical verification* in *2012 IEEE 27th Conference on Computational Complexity* (2012), 42–52.

118. Zhandry, M. Quantum lightning never strikes the same state twice. or: quantum money from cryptographic assumptions. *Journal of Cryptology* **34,** 1–56 (2021).

119. Farhi, E., Gosset, D., Hassidim, A., Lutomirski, A. & Shor, P. *Quantum money from knots* in *Proceedings of the 3rd Innovations in Theoretical Computer Science Conference* (2012), 276–289.

120. Anasori, B. & Gogotsi, Y. G. *2D metal carbides and nitrides (MXenes)* (Springer, 2019).

121. Anayee, M. *et al.* Role of acid mixtures etching on the surface chemistry and sodium ion storage in $Ti_3C_2T_x$ MXene. *Chemical Communications* **56,** 6090–6093 (2020).

122. Gogotsi, Y. & Anasori, B. *The rise of MXenes* 2019.

123. Naguib, M. & Gogotsi, Y. Synthesis of two-dimensional materials by selective extraction. *Accounts of Chemical Research* **48,** 128–135 (2015).

124. Ghidiu, M., Lukatskaya, M. R., Zhao, M.-Q., Gogotsi, Y. & Barsoum, M. W. Conductive two-dimensional titanium carbide 'clay' with high volumetric capacitance. *Nature* **516,** 78–81 (2014).

125. Katiyi, A. & Karabchevsky, A. Si Nanostrip Optical Waveguide for On-Chip Broadband Molecular Overtone Spectroscopy in Near-Infrared. *ACS Sensors* **3,** 618–623 (2018).

126. Anasori, B., Lukatskaya, M. R. & Gogotsi, Y. 2D metal carbides and nitrides (MXenes) for energy storage. *Nature Reviews Materials* **2,** 1–17 (2017).

127. Dillon, A. D. *et al.* Highly conductive optical quality solution-processed films of 2D titanium carbide. *Advanced Functional Materials* **26,** 4162–4168 (2016).

128. Polyanskiy, M. *Refractive index database. Silicon (Si).* https://refractiveindex.info/?shelf=main&book=Si&page=Pierce.

129. Polyanskiy, M. *Refractive index database. Fused Silica (SiO2).* https://refractiveindex.info/?shelf=main&book=SiO2&page=Malitson.

130. COMSOL, A. *Wave Optics Module User's Guide, COMSOL Multiphysics V. 5.6.* https://doc.comsol.com/5.6/doc/com.comsol.help.woptics/WaveOpticsModuleUsersGuide.pdf.

131. Gonçalves, M. *et al. Interband, Surface Plasmon and Fano Resonances in Titanium Carbide (MXene) Nanoparticles in the Visible to Infrared Range* in *Photonics* **8** (2021), 36.

132. Satheeshkumar, E. *et al.* One-step solution processing of Ag, Au and Pd@MXene hybrids for SERS. *Scientific Reports* **6,** 1–9 (2016).

133. Hu, T. *et al.* Vibrational properties of Ti_3C_2 and $Ti_3C_2T_2$ (T=O, F, OH) monosheets by first-principles calculations: a comparative study. *Physical Chemistry Chemical Physics* **17,** 9997–10003 (2015).

134. Karabchevsky, A., Wilkinson, J. S. & Zervas, M. N. Transmittance and surface intensity in 3D composite plasmonic waveguides. *Optics Express* **23,** 14407–14423 (2015).

135. Mauchamp, V. *et al.* Enhanced and tunable surface plasmons in two-dimensional Ti 3 C 2 stacks: Electronic structure versus boundary effects. *Physical Review B* **89,** 235428 (2014).

136. The MathWorks, I. *MATLAB Deep Learning Toolbox.* https://www.mathworks.com/products/deep-learning.html.

137. Goodfellow, I., Bengio, Y. & Courville, A. *Deep learning* (MIT press, 2016).

138. Goodman, J. W. Introduction to fourier optics, roberts & co. *Publishers, Englewood, Colorado* (2005).

139. Kumar, N. Practically feasible robust quantum money with classical verification. *Cryptography* **3,** 26 (2019).

140. Zhang, M., Wang, C., Kharel, P., Zhu, D. & Lončar, M. Integrated lithium niobate electro-optic modulators: when performance meets scalability. *Optica* **8,** 652–667 (2021).

141. Van Haasteren, A. J., van der Tol, J. J., Van Deventer, M. O. & Frankena, H. J. Modeling and characterization of an electrooptic polarization controller on LiNbO/sub 3. *Journal of lightwave technology* **11,** 1151–1157 (1993).

142. Guan, J., Liu, X. & Booth, M. J. Ultrafast laser writing quill effect in low loss waveguide fabrication regime. *Optics Express* **26,** 30716–30723 (2018).

143. Huang, L., Salter, P., Payne, F. & Booth, M. Aberration correction for direct laser written waveguides in a transverse geometry. *Optics Express* **24,** 10565–10574 (2016).

144. Guan, J., Liu, X., Salter, P. S. & Booth, M. J. Hybrid laser written waveguides in fused silica for low loss and polarization independence. *Optics Express* **25,** 4845–4859 (2017).

145. Polyanskiy, M. *Refractive index database. Borosilicate Glass (BK7).* https://refractiveindex.info/?shelf=glass&book=BK7&page=SCHOTT.

146. Jesacher, A., Salter, P. & Booth, M. Refractive index profiling of direct laser written waveguides: tomographic phase imaging. *Optical Materials Express* **3,** 1223–1232 (2013).

147. Guan, J., Liu, X. & Booth, M. J. Investigation of structural mechanisms of laser-written waveguide formation through third-harmonic microscopy. *Optics Letters* **44,** 1039–1042 (2019).

148. Marshall, G. D., Jesacher, A., Thayil, A., Withford, M. J. & Booth, M. Three-dimensional imaging of direct-written photonic structures. *Optics Letters* **36,** 695–697 (2011).

149. Guan, J., Menssen, A. J., Liu, X., Wang, J. & Booth, M. J. Component-wise testing of laser-written integrated coupled-mode beam splitters. *Optics Letters* **44,** 3174–3177 (2019).

150. Inc., T. *Non-Polarizing Beamsplitter Cubes.* https://www.thorlabs.com/newgrouppage9.cfm?objectgroup_id=4129&pn=CCM1-BS015.

151. Hughes, T. W., Minkov, M., Shi, Y. & Fan, S. Training of photonic neural networks through in situ backpropagation and gradient measurement. *Optica* **5,** 864–871 (2018).

152. Zhang, T. *et al.* Efficient training and design of photonic neural network through neuroevolution. *Optics Express* **27,** 37150–37163 (2019).

APPENDIX A

Publications

A.1 Journal Publications

1. **Hazan, A.**, Ratzker, B., Zhang, D., Katiyi, A., Sokol, M., Gogotsi, Y. and Karabchevsky, A., ”MXene Nanoflakes Enabled All-Optical Nonlinear Activation Function for On-Chip Photonic Deep Neural Networks.” *Advanced Materials*, (2023). *Accepted for publication,* https://doi.org/10.1002/adma.202210216.

2. Sun, B., Morozko, F., Salter, P.S., Moser, S., Pong, Z., Patel, R.B., Walmsley, I.A., Wang, M., **Hazan, A.** et al., ”On-Chip Beam Rotators, Adiabatic Mode Converters, and Waveplates through Low-Loss Waveguides with Variable Cross-Sections.” *Light: Science & Applications*, 11(1), 1-15 (2022).

3. Karabchevsky, A, **Hazan, A.** and Dubavik, A., ”All-Optical Polarization-Controlled Nanosensor Switch Based on Guided-Wave Surface Plasmon Resonance via Molecular Overtone Excitations in the Near-Infrared.” *Advanced Optical Materials*, 8(19):2000769 (2020). *Selected to be on the front cover of Advanced Optical Materials Journal, 8(19)*.

4. Karabchevsky, A., Katiyi, A., Ang, A.S. and **Hazan, A.**, ”On-Chip Nanophotonics and Future Challenges.” *Nanophotonics*, 9(12):3733-3753 (2020). *Invited.*

A.2 Conference Contributions

Conferences

1. **Hazan, A.**, Ratzker, B., Zhang, D., Katiyi, A., Frage, N., Sokol, M., Gogotsi, Y. and Karabchevsky, A., *Realization of neuron’s nonlinear activation function optically on a chip by MXene in Near-Infrared.* International Day of Light conference, BGU, Israel, 2021. *Best Poster Award.*

2. **Hazan, A.**, Ratzker, B., Zhang, D., Katiyi, A., Frage, N., Sokol, M., Gogotsi, Y. and Karabchevsky, A., *On-Chip All-Optical Nonlinear Activation Function for Photonic Neural Network via Two-Dimensional Ti_3C_2 (MXene) in Near-Infrared*. The 66th Israel Physical Society Conference (IPS), Israel, 2021. *Poster*.

3. **Hazan, A.**, Sattah, O. and Karabchevsky, A., *On-chip Quantum Money with Classical Verification*. The 66th Israel Physical Society Conference (IPS), Israel, 2021. *Poster*.

4. Karabchevsky, A. and **Hazan, A.**, *All-optical switch with hybrid plasmonic molecular systems: sensing or switching?*. Nonlinear Metamaterials and Photonic Crystals, Kfar Blum, Israel, 2019. *Talk*.

5. Karabchevsky, A. and **Hazan, A.**, *Metamaterials-based probing weak quantum absorber in coupled three-resonator system with guided wave surface plasmons: sensing or all-optical switching?*. The 10th International Conference on Metamaterials, Photonic Crystals and Plasmonics (Meta 2019), Lisbon, Portugal, 2019. *Talk*.

Patents

I Karabchevsky, A. and **Hazan, A.**, (2021). *All-Optical Nonlinear Activation Function for Photonic Neural Network*. No. 63/228,110, ApplDate: 01/08/2021, USA.

II Karabchevsky, A. and **Hazan, A.**, (2020). *Twisted Waveguide as Polarization Entangled Photon Pair Source*. No. 63/066,272, ApplDate:16/08/2020, USA.

תקציר

פוטוניקה משולבת היא אחת מאבני הדרך המשמעותיות של מדעי האלקטרו-אופטיקה והפוטוניקה. פלטפורמה זו מכילה התקנים אופטו-אלקטרוניים על-שבב העוסקים בשליטה ובמניפולציה של האור במעגלים משולבים עבור יישומים שמטרתם להשיג יתרונות העולים על הביצועים המסורתיים של האלקטרוניקה. ארכיטקטורות מהירות במיוחד ובעלות הספק נמוך אלה, משכו עניין רחב והובילו לניצול אפשרי במגוון רחב של תחומים מסחריים ושדות מחקר, כולל תקשורת אופטית, מחשוב אופטי, עיבוד מידע קוונטי-אופטי, קריפטוגרפיה ועוד תחומים רבים אחרים.

בעבודה זו, חקרתי כיוונים חדשים שונים ולמדתי כיצד ניתן להשתמש בתצורות המבוססות על מוליכי-גלים אופטיים עבור יישום פונקציות אופטיות ייחודיות. על ידי שימוש באינטראקציות אור-וחומר ב-$\mathrm{Ti_3C_2T}_x$ דו מימדי (ממשפחת MXenes) בתחום האינפרא אדום הקרוב, הדגמתי באופן ניסיוני שתי גישות חדשות ליישום אופטי של פונקציית השיפעול הלא ליניארית של הנוירון בשתי תצורות: 1) מוליך גל העשוי מסיליקון עם שכבה של פתיתי MXene, שהונחה על גבי המשטח העליון של מוליך הגל ו-2) שכבה דקה של MXene שהונחה על מצע שקוף. התצורות כפי שהוצעו יכולות לשמש כיחידות לא ליניאריות ביישומים אופטיים של ארכיטקטורות לימוד-מכונה, שבהן ניתן לתכנן את פונקציית ההעברה הלא ליניארית בצורה גמישה בהתאם לאורך גל ההפעלה, מבלי לשנות את המבנה הפיזי שלהן. יכולתן והיתכנותן של התצורות, שהוזכרו לעיל, נבחנו בהשוואה לפונקציות שיפעול לא ליניאריות המבוססות תוכנה המצויות בשימוש נרחב. זאת על ידי ביצוע משימות סיווג, תוך שימוש בשתי ארכיטקטורות עצמאיות של לימוד-מכונה, בכדי לאפיין את הביצועים שלהן במונחים של דיוק. ניתן לעשות שימוש בטכניקה זו ממש גם כדי ליישם משימות שרירותיות של לימוד-מכונה.

במסגרת עבודתי זו, תכננתי קונסטרוקציה פוטונית מעשית המבוססת על אבני בניין של פוטוניקה-משולבת עבור יישום סכימת הכסף הקוונטי על-שבב (כ'אסימונים' קוונטיים). מימוש הקיוביטים נעשה באמצעות קבוצת אופנים אופטיים מקוטבים הנתמכים במוליך הגל. המבנים האופטימליים של ההתקנים הפוטונים המוצעים - המשדר והמקלט, הושגו על ידי ניתוח תיאורטי נרחב של מנגנון הפעולה האופטי שלהם. בנוסף, הוצע תכנון למערך ניסוי לאב-טיפוס עבור מימוש האסימון הפוטוני תוך שימוש בהתקני תקשורת אופטית, הזמינים כיום, ומבוססים על מוליכי גל אופטים.

הדגמתי באופן ניסיוני את ההתכנות לביצוע מניפולציה על מצב הקיטוב של אור מקוטב לינארי המתפשט במוליך גל בעל מבנה תלת מימדי ייחודי, המקיים יחס ניגודיות נמוך בין מקדמי השבירה של הליבה לבין התווך הסובב אותה. עבור מוליך גל מפותל המוטבע במצע זכוכית, בעל זווית פיתול של 90 מעלות וחתך מלבני מסובב לאורכו, מצב הקיטוב משתנה בהדרגה יחד עם התפשטות האור לאורך האזור המפותל.

עבור כל נושא במחקר, הצגתי את המושגים הבסיסיים והגישות הנדרשות להבנת האינטראקציות של האור-והחומר המשולבים עם מוליכי-גלים אופטיים. השיטות בהן נעשה שימוש להשגת כל יעדי המחקר מסוכמים בעבודה זו, וכמו כן הבחנות נומריות וניסיוניות הודגמו ונותחו בתזה זו.

אוניברסיטת בן-גוריון בנגב
הפקולטה למדעי ההנדסה
בית הספר להנדסת חשמל ומחשבים
המחלקה להנדסת אלקטרו-אופטיקה ופוטוניקה

ארכיטקטורות פוטוניות משולבות חדישות למניפולציה יעילה של אור על שבב

מאת

אדיר חזן

חיבור זה מהווה חלק מהדרישות לקבלת תואר מגיסטר בהנדסה

בהנחיית

פרופ׳ אלינה קרבצ׳בסקי

אדיר חזן	17.2.2023
חתימת המחבר	*תאריך*
Alina Karabchevsky	19/02/2023
חתימת המנחה	*תאריך*
חתימת יו״ר וועדת הוראה מחלקתית	*תאריך*

ספטמבר, 2022
אלול תשפ״ב

אוניברסיטת בן-גוריון בנגב
הפקולטה למדעי ההנדסה
בית הספר להנדסת חשמל ומחשבים
המחלקה להנדסת אלקטרו-אופטיקה ופוטוניקה

ארכיטקטורות פוטוניות משולבות חדישות למניפולציה יעילה של אור על שבב

מאת

אדיר חזן

חיבור זה מהווה חלק מהדרישות לקבלת תואר מגיסטר בהנדסה

בהנחיית

פרופ׳ אלינה קרבצ׳בסקי

ספטמבר, 2022
אלול תשפ״ב